NASA CR-54978

Rocketdyne R-6636 -1

FINAL REPORT

FLUORINE-HYDROGEN PERFORMANCE EVALUATION

PHASE I, PART I: ANALYSIS, DESIGN, AND DEMONSTRATION

HIGH-PERFORMANCE INJECTORS FOR THE LIQUID

FLUORINE-GASEOUS HYDROGEN PROPELLANT COMBINATION

By

H. A. Arbit
S. D. Clapp

prepared for

NATIONAL AERONAUTICS AND SPACE ADMINISTRATION

Contract NASw-1229

ROCKETDYNE RESEARCH DEPARTMENT
North American Aviation, Inc.
6633 Canoga Avenue, Canoga Park, California

NOTICE

This report was prepared as an account of Government sponsored Work. Neither the United States, nor the National Aeronautics and Space Administration (NASA), nor any person acting on behalf of NASA:

A.) Makes any warranty or representation, expressed or implied, with respect to the accuracy, completeness, or usefulness of the information contained in this report, or that the use of any information, apparatus, method, or process disclosed in this report may not infringe privately owned rights; or

B.) Assumes any liabilities with respect to the use of, or for damages resulting from the use of any information, apparatus, method or process disclosed in this report.

As used above, "person acting on behalf of NASA" includes any employee or contractor of NASA, or employee of such contractor, to the extent that such employee or contractor of NASA or employee of such contractor prepares, disseminates, or provides access to, any information pursuant to his employment or contractor with NASA, or his employment with such contractor.

Requests for copies of this report should be referred to

National Aeronautics and Space Administration
Office of Scientific and Technical Information
Attention: AFSS-A
Washington, D.C. 20546

FINAL REPORT

FLUORINE-HYDROGEN PERFORMANCE EVALUATION,

PHASE I, PART I: ANALYSIS, DESIGN, AND DEMONSTRATION OF

HIGH PERFORMANCE INJECTORS FOR THE LIQUID FLUORINE-

GASEOUS HYDROGEN COMBINATION

By

H. A. Arbit
S. D. Clapp

prepared for

NATIONAL AERONAUTICS AND SPACE ADMINISTRATION
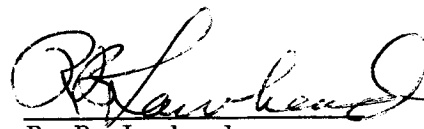
July 1966

Contract NASw-1229

Technical Management
NASA Lewis Research Center
Cleveland, Ohio
Advanced Rocket Technology Branch
Paul Herr

Rocketdyne Research Department
North American Aviation, Inc.
6633 Canoga Avenue, Canoga Park, California

FLUORINE-HYDROGEN PERFORMANCE EVALUATION,
PHASE I, PART I: ANALYSIS, DESIGN, AND DEMONSTRATION OF
HIGH PERFORMANCE INJECTORS FOR THE LIQUID FLUORINE-
GASEOUS HYDROGEN COMBINATION

Technically Reviewed and Approved By:

E. V. Zettle
Group Scientist
Propulsion Applications
Research Division

R. B. Lawhead
Chief
Propulsion Processes
and Applications
Research Division

J. Friedman
Program Manager
Small Engines Division

August 1966

ii

FOREWORD

This report was prepared in compliance with Article
IX of NASA Contract NASw-1229, under Rocketdyne
G.O. 8708. NASA Program direction was provided by
Mr. F. Stephenson, NASA Headquarters, Washington,
D.C., and Mr. P. Herr, NASA Lewis Research Center.
Mr. J. Friedman, Small Engines Division, was Pro-
gram Manager for the subject contract.

For that portion of the overall project carried
out by the Research Division and reported herein,
S. D. Clapp served as Responsible Engineer, and
H. A. Arbit as Project Engineer.

ACKNOWLEDGMENT

Important contributions to the conduct of the pro-
gram and to the preparation of report material
were made by the following personnel:

> B. J. Heckert
> J. P. Bott
> R. L. Fallack
> D. E. Zwald

CONTENTS

ILLUSTRATIONS

TABLES

SUMMARY

Delivered performance of the fluorine–hydrogen propellant combination is greatly dependent upon the nature of the nozzle expansion process, because this combination exhibits a substantial difference between frozen and shifting specific impulse. To establish design criteria for maximum-recombination nozzle contours, experimental determinations of performance in various types of nozzles are necessary. The primary purpose of the program was to make such determinations with liquid fluorine-gaseous hydrogen, under simulated altitude conditions, over a nine-point parametric matrix of chamber pressure (50, 100, 200 psia) and mixture ratio (9, 12, and 15).

Because a high–performing injector/chamber combination is essential to such investigations of nozzle efficiency, they were preceded by an analytical, design, and experimental firing effort to establish a combination(s) which exhibited minimum c* efficiency of 97 percent over the parametric matrix. This effort is the subject of the present report. A secondary objective of these studies was the acquisition of heat flux data at the various operating conditions.

Two injectors were designed for use with an uncooled, segmented, calorimetric thrust chamber (L* = 30 inches) designed for 2500-pound thrust (vacuum, ϵ = 60) at the midpoint of the experimental matrix (chamber pressure = 100 psia, mixture ratio = 12). One was a triplet pattern, in which LF_2 doublets impinged upon a central showerhead GH_2 jet; the other also employed self–impinging LF_2 doublets, with showerhead GH_2 jets on each side of the spray fan.

Particular attention was paid to the procedures used to obtain the experimental data, and analyses are presented covering their reliability and precision. Redundant measurements were made of all important parameters and characteristic velocity was calculated by two independent methods, one based on chamber pressure and the other on thrust. Average variation from the mean of the c* values obtained in the two ways was ±0.7 percent.

Both the triplet and the doublet/showerhead injector exhibited corrected c* efficiencies of 97 percent or greater over the entire chamber pressure/mixture ratio matrix, thus satisfying the requirements for the nozzle performance investigations.

Performance differences between the injectors, obscured in the 30-inch L* chamber, were brought out by use of shorter chamber lengths (L* = 10 inches and L* = 3.4 inches), in which the triplet pattern showed significantly higher c* efficiencies (approximately 3.5 percent) than the doublet/showerhead.

The performances of both injectors are discussed in terms of the degree of liquid atomization which they produce; in both designs, the gas jets perform an important atomizing function.

Heat flux was measured by a transient temperature technique using isolation segments machined into the chamber walls. Circumferential variations were random, and on the order of ±6 percent. Axial variations indicated heat transfer coefficients in the combustion chamber of approximately 3 Btu/in.^{2}/sec/F (at 50-psia chamber pressure) to approximately 11 Btu/in.^{2}/sec/F (at 200-psia chamber pressure); in the throat region, values ranged from approximately 6 Btu/in.^{2}/sec/F (50-psia chamber pressure) to approximately 13 Btu/in.^{2}/sec/F (at 200-psia chamber pressure).

There were no significant differences between the two injectors with regard to heat flux in the chamber or nozzle.

In the 10-inch L* chamber (with 3.2-inch combustion chamber), heat fluxes were approximately the same as at corresponding positions in the 30-inch L* chamber (with 13-inch combustion chamber). In the 3.4-inch L* chamber (with injector joined directly to the nozzle), heat fluxes were substantially higher, reflecting combustion in the nozzle.

The heat transfer results are discussed in terms of the relative magnitudes of the three sources of chamber wall heat flux: convection, radiation, and recombination. It is shown that use of overall, measured heat transfer coefficients to indicate the nature of local boundary layer regimes may be inappropriate under conditions of varying degrees of chemical recombination.

INTRODUCTION

Several characteristics of the fluorine-hydrogen propellant combina-
tion, including high specific impulse, hypergolicity, and low hydrogen
requirements, make it eminently suitable for high-energy space missions,
For simplicity and reliability, a low-chamber pressure, pressure-fed
propulsion system using this combination is indicated. Actual achieve-
ment of the high performance inherent in fluorine-hydrogen, however,
is predicated on attainment of nozzle expansion as close to shifting
equilibrium as possible, because for these propellants the difference
in specific impulse between the extremes of shifting and frozen expansion
is substantial. This is indicated in Fig. 1, which shows theoretical
vacuum specific impulse of LF_2/GH_2 for three expansion modes at chamber
pressure of 100 psia and expansion ratio of 60. The difference between
shifting and frozen specific impulse at mixture ratio 15 is 80 seconds
(about 20 percent), while that between shifting and frozen-at-the-throat
specific impulse at mixture ratio 15 is 64 seconds (about 16 percent).
Because of the sensitivity of mission capability to propellant performance,
these differences are highly significant. Hence, experimental determina-
tion of fluorine-hydrogen performance in conventional nozzles and in noz-
zles designed for maximum recombination is an essential prerequisite to
use of this combination in propulsion systems.

An experimental program to make such determinations of nozzle efficiency
has been carried out by Rocketdyne under NASA Contract NASw-1229. The
primary program objective was the determination under altitude conditions
of deliverable performance of the liquid fluorine-gaseous hydrogen pro-
pellant combination over a parametric range suitable for pressure-fed,
upper-stage applications, as a function of high-area-ratio nozzle contour.
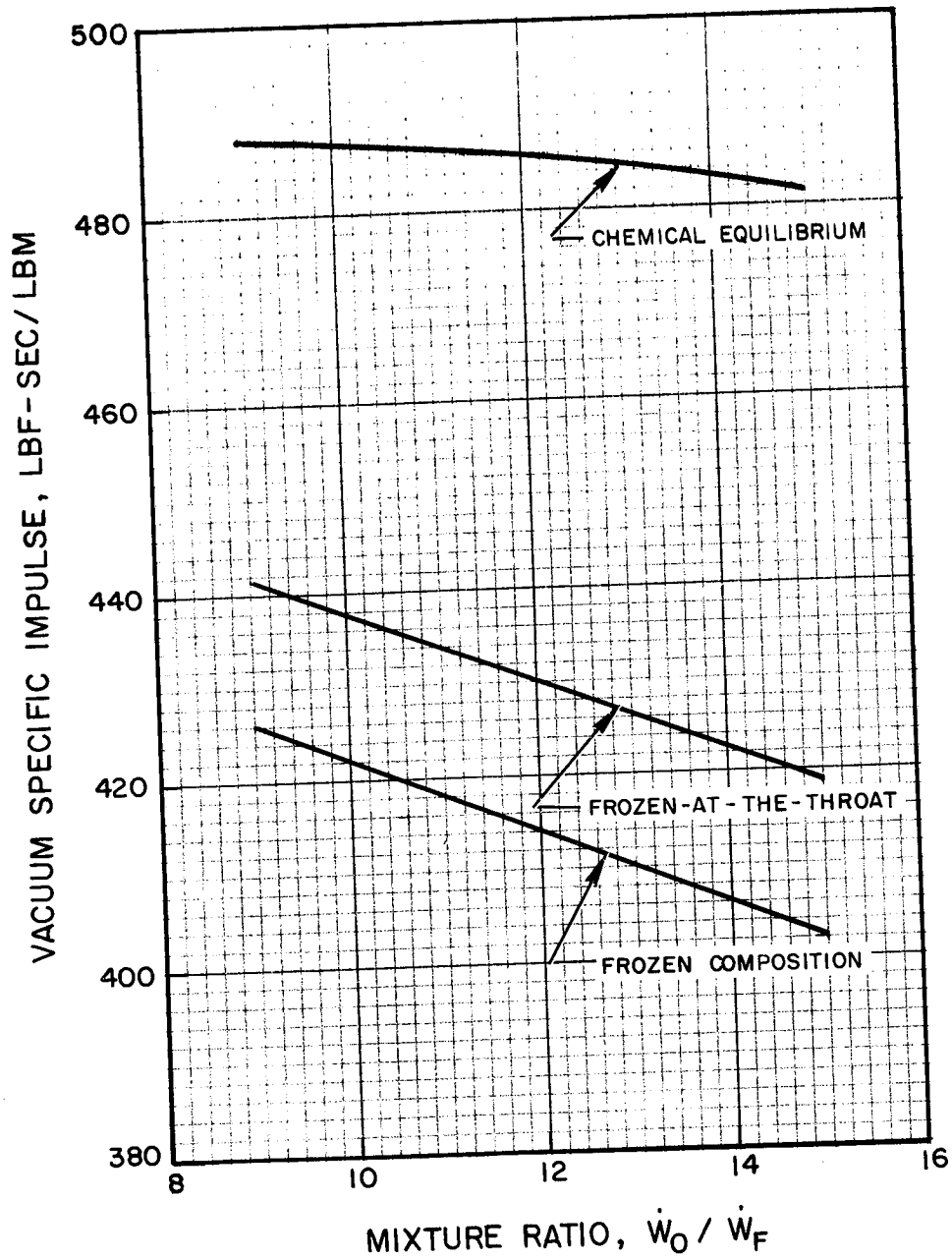
Figure 1. Comparison of LF_2/GH_2 Performance Models; Chamber Pressure = 100 psia, Expansion Ratio = 60.

A secondary objective was the acquisition of thrust chamber heat flux data, so that cooling requirements could be determined. A nine-point parametric matrix was selected for these investigations, consisting of three mixture ratio levels at each of three chamber pressures:

Chamber pressure = 50, 100, 200 psia
Mixture ratio   = 9, 12, 15

To evaluate the nozzles properly, a high-performance injector-chamber combination was required, so that combustion efficiency could be isolated from nozzle efficiency. Consequently, establishment of such a combination was an essential portion of the overall program, which was divided into the following separate tasks:

Task I: (a) Analysis and design to establish injector and
                chamber configurations
           (b) Nozzle performance analysis and contour design

Task II: Experimental demonstration of an injector/chamber
           configuration(s) which provides minimum corrected c*
           efficiency of 97 percent over the nine-point chamber
           pressure/mixture ratio matrix, and determination of
           thrust chamber longitudinal and circumferential heat
           transfer characteristics

Task III: Experimental evaluation of vacuum thrust coefficients
           attainable from 60:1 area ratio nozzles of 15-degree
           conical contour, 70-percent bell contour, and a "per-
           formance optimized" contour

7

The present report is concerned with those portions of the overall program relating to the analysis, design, and experimental evaluation of injectors and thrust chamber to meet the minimum performance requirement, and determination of the accompanying heat flux characteristics, Tasks I(a) and II.

Previous experimental studies of the LF_2/GH_2 propellant combination concerned with injector/chamber design and performance have been reported by NASA (Ref. 1 and 2) and by Rocketdyne (Ref. 3 and 4).

The results of these earlier investigations indicated that high c* efficiency could be obtained with properly designed, simple injector patterns over the chamber pressure/mixture ratio matrix of the present program, particularly since a comparatively long chamber (L* = 30 inches) could be employed. Two such injectors were designed and were found to give c* efficiencies in excess of the minimum required over the entire experimental parametric matrix.

Heat flux determinations were made by a transient conduction technique from temperature histories measured at isolation areas machined along the chamber and nozzle walls.

Following a summary of the sources and applications of the criteria used for injector design and of the experimental facilities and procedures, the experimental performance and heat flux results are presented and discussed. Analyses covering chamber design, computational methods, error limits, and minor experimental results are presented in a series of appendixes.

Gas-Liquid Injector Design Criteria

The design approach appropriate to gas-liquid injectors is the same as that for liquid-liquid types; their common goal is optimization of the processes of propellant atomization and distribution. Since one of the propellants is injected as a gas, which is rapidly and uniformly distributed, it follows that atomization/vaporization of the single liquid component is the rate-limiting step in the overall combustion process of a gas/liquid system.

A useful characteristic of gas/liquid propellants is the possibility of using the injected gas as a means of atomizing the liquid. In one such method, coaxial jet injection, the liquid is atomized by the shear forces at the liquid-gas interface which arise from the difference in velocities of the two propellants as well as by recirculation gases near the injector (Ref. 5). Another technique makes use of the gas momentum together with the kinetic energy of the liquid streams to provide a high degree of liquid atomization. Although coaxial jet injectors have been successfully used for the LF_2/GH_2 propellant combination (Ref. 1 and 2), they present substantially greater fabrication complexities than do simple orifice patterns. For this reason, and in view of previous work at Rocketdyne (Ref. 3 and 4) and NASA (Ref. 1) which indicated that high gas/liquid performance can be obtained with simple orifice geometries, impinging LF_2 streams with GH_2-augmented atomization were selected as the basic injection elements for the present program.

The ideal gas/liquid injector (i.e., one which gives maximum performance with minimum chamber length) must make optimum use of both liquid and gas momenta to effect liquid atomization. However, injector optimization to

the extent of designing such an ideal injector was not an objective of the present experimental study, because a relatively long chamber (L* = 30 inches, injector face-to-throat distance = 15.4 inches) was to be used.

Two basic simple-orifice designs were employed: (1) a doublet/showerhead pattern, in which showerhead GH_2 jets were positioned on both sides of the fans formed by impinging LF_2 doublets, and (2) a triplet pattern, in which two LF_2 streams impinged on a central showerhead GH_2 jet. The designs were similar in that both used self-impinging LF_2 doublets, which gave a primarily two-dimensional spray pattern in a plane perpendicular to the plane of the jets. In the first case, the gas jets interacted with the liquid after formation of the spray fan, while in the latter a gas jet was directed to the point of stream impingement. Design criteria for each of the patterns are discussed below.

Doublet-Showerhead Pattern. A combustion model in which propellant vaporization (and hence degree of atomization) is the rate-controlling process has been described by Priem and Heidmann (Ref. 6) who derived theoretical relationships between the initial size of a liquid droplet and the percentage of liquid vaporized within a given chamber length for various propellant combinations. These relationships are illustrated in Fig. 2, which shows calculated percentage of LF_2 vaporized for various initial drop sizes in chambers of varying combustion length (defined as cylindrical chamber length between point of droplet formation and start of nozzle convergence).
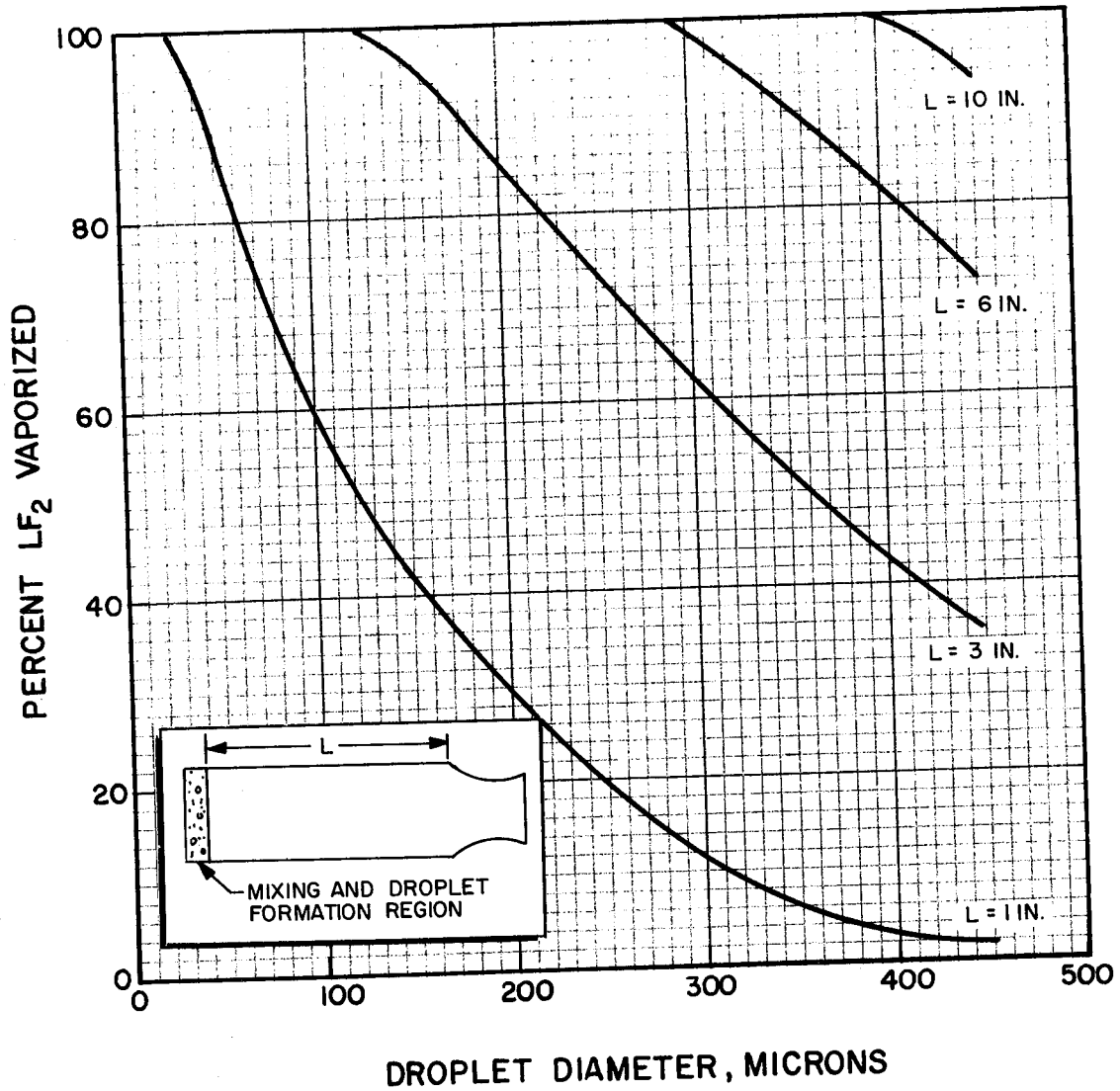
Figure 2. Effect of Fluorine Droplet Size and Combustion Chamber Length on Percent of LF_2 Vaporized; LF_2/GH_2 Combustion at Chamber Pressure of 300 psia, Initial Droplet Velocity of 100 ft/sec, Final Gas Velocity in Combustion Chamber of 800 ft/sec. Date from Ref. 6.

The curves in Fig. 2 indicate that for a combustion length of 12 inches (approximately the value in the 30-inch L* chamber used in this program), complete vaporization is obtained with droplet diameters no greater than about 400 microns.

Drop size distributions in the sprays formed from self-impinging doublet orifices in a uniform-velocity gas stream were experimentally determined by Ingebo (Ref. 7), who obtained the following correlation:

$$\frac{D_i}{D_{30}} = 2.64 \ (D_j V_j)^{1/2} + 0.97 \ D_j \ \Delta V \tag{1}$$

where

D_j = orifice diameter (assumed to be equal to diameter of the liquid jet), inches

D_{30} = volume-number-mean drop diameter (diameter of a droplet in a uniform spray whose volume and number of drops are equal to those of the original spray distribution), inches

V_j = velocity of liquid jet, ft/sec

ΔV = gas-liquid velocity difference, ft/sec

Maximum droplet sizes were approximately two to three times the volume-number-mean diameter.

On the basis of 200-psi maximum injector pressure drop (set by Task III altitude facility requirements) and 6-inch chamber diameter, 49 pairs of LF_2 orifices (D = 0.043 inches) were used in the doublet/showerhead injector. Values of D_{30} corresponding to this orifice diameter were calculated from the Ingebo equation for the two "worst" cases: $\Delta V = 0$,

which gives the poorest degree of atomization, and $V_{GH_2} = 0$, which does not include secondary atomization by the gas. Results are listed in Table 1 and indicate that even in these cases the LF_2 droplet sizes are within the approximate limits calculated by Priem (Ref. 6) for complete vaporization.

TABLE 1

VOLUME–NUMBER–MEAN DIAMETER OF LF_2 DROPS, DOUBLET/SHOWERHEAD
INJECTOR, CALCULATED FROM INGEBO EQUATION

	D_{30}, microns $(\Delta V = 0)$			D_{30}, microns $(V_{GH_2}) = 0)$		
Mixture Ratio	9	12	15	9	12	15
Chamber Pressure						
50	384	378	372	276	271	265
100	275	269	264	177	172	167
200	196	191	187	110	106	101

The fuel orifices in the doublet/showerhead injector were sized on the basis of equal numbers of oxidizer and fuel orifices and maximum GH_2 velocity at orifice exit of Mach 0.9. This resulted in GH_2 orifice diameters of 0.089 inches.

<u>Triplet</u>. In the triplet element (two LF_2 jets impinging in a central GH_2 showerhead jet), a high–velocity gas field is superimposed on the liquid jets, the effect of which is to enhance substantially the degree of liquid atomization. Detailed descriptions of the characteristics of this type of injector element are given in Ref. 8.

With the same requirements of oxidizer side ΔP, thrust per element, and injector size as for the doublet/showerhead injector, a square pattern of triplet elements was developed, with 64 pairs of LF_2 orifices and 64 GH_2 orifices. Oxidizer orifice diameters were 0.039 inches, which produce droplets within the approximate Priem-Ingebo criteria limits discussed above.

Fuel orifices were sized from a correlation developed for triplet injector patterns to relate c* efficiencies obtained with LF_2/GH_2 and LO_2/GH_2 to a function of gas injection velocity, mass of available gas, and mass of liquid to be atomized (Ref. 9). The general relationship is shown in Fig. 3, in which c* efficiency is plotted against the parameter α :

$$\alpha = K \frac{\left(V_{GH_2}\right)^a}{(r)^b} \qquad (2)$$

where

$$V_{GH_2} = GH_2 \text{ injection velocity}$$

$$r = \text{mixture ratio}$$

$$K, a, b = \text{correlating constants}$$

Values of this drop size parameter greater than about 4 are seen to correspond to high performance. Use of 0.109-inch-diameter GH_2 orifices gives GH_2 injection Mach numbers of 0.6 (at mixture ratio = 15) to 0.9 (at mixture ratio = 9), with respective drop size parameter values of 3 to 7.

Impingement distance is a significant parameter relating to the degree of liquid atomization produced by a triplet element, because of the structure of a gas jet expanding freely from a circular orifice (Ref. 10). An
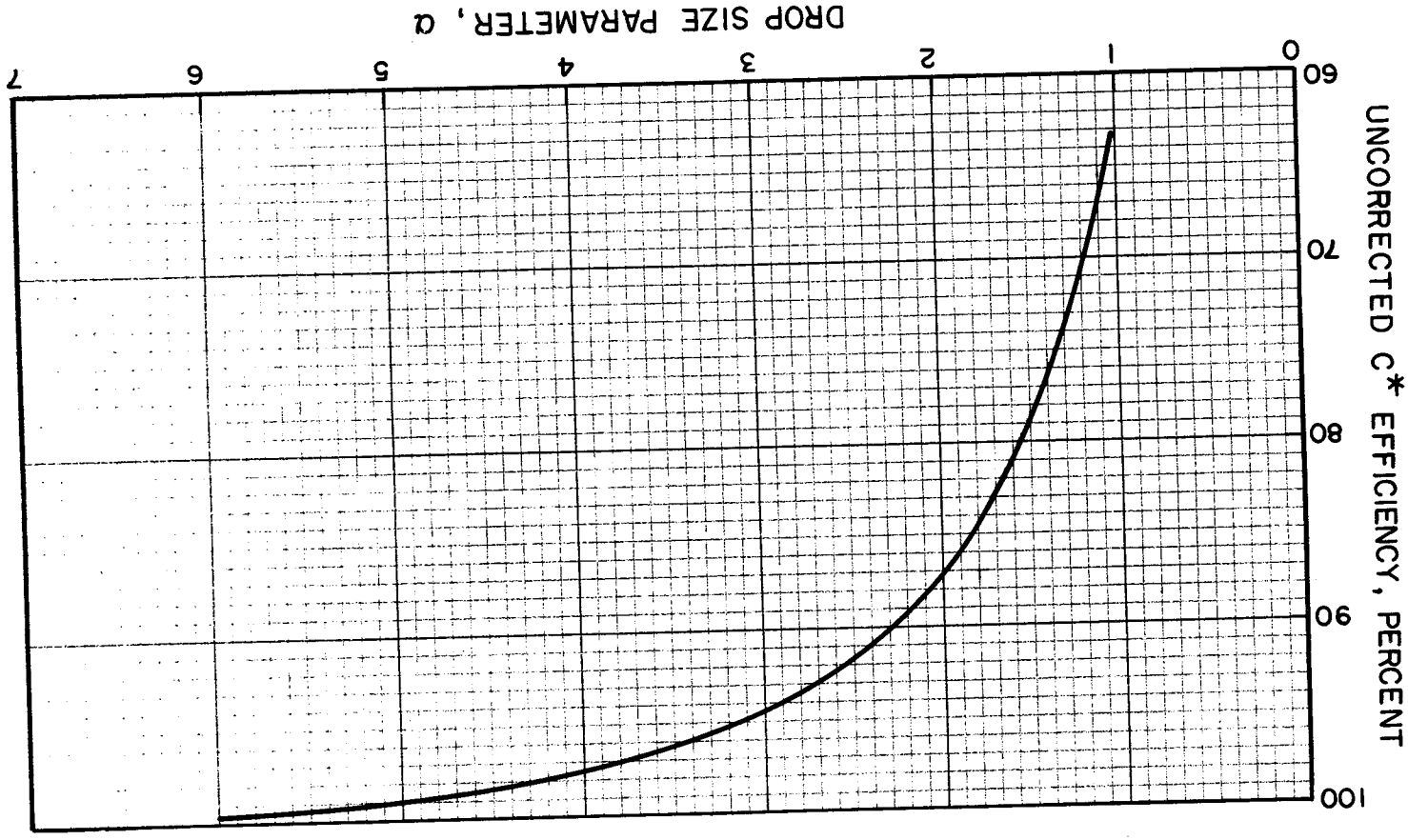
Figure 3. Effect of Drop Size Parameter (Equation 2) on c^* Efficiency of LF_2/GH_2 and LOX/GH_2 in Triplet Injectors. Data from Ref. 9.

important feature of this structure is the presence of a central, cone-shaped section, referred to as the potential core, within which the gas momentum is not significantly degraded. The potential core extends for a distance of about 3 jet diameters from the orifice (Ref. 8) with some evidence that its length increases slightly with increasing gas velocity. To make maximum use of gas momentum for liquid atomization, the impingement point of the liquid jets should fall within the potential core, because gas jet velocity decreases rapidly outside it. Hence, design impingement point of the triplet element was 2.8 jet diameters from the injector face.

Another important orifice parameter is the impingement angle between the liquid streams, which affects not only the nature of the spray formed, but also the amount of splash-back to the injector face. A general impingement angle design objective for high performance is to use the maximum angle consistent with absence of significant splash-back. Because injector face burning is fairly often observed with 90-degree impingement angles, but rarely with 60-degree angles, the latter was used in both injector patterns.

Specific Injector Designs

Doublet/Showerhead. Face pattern of the doublet/showerhead injector is shown in Fig. 4. Design parameters of this injector are given in Table 2.
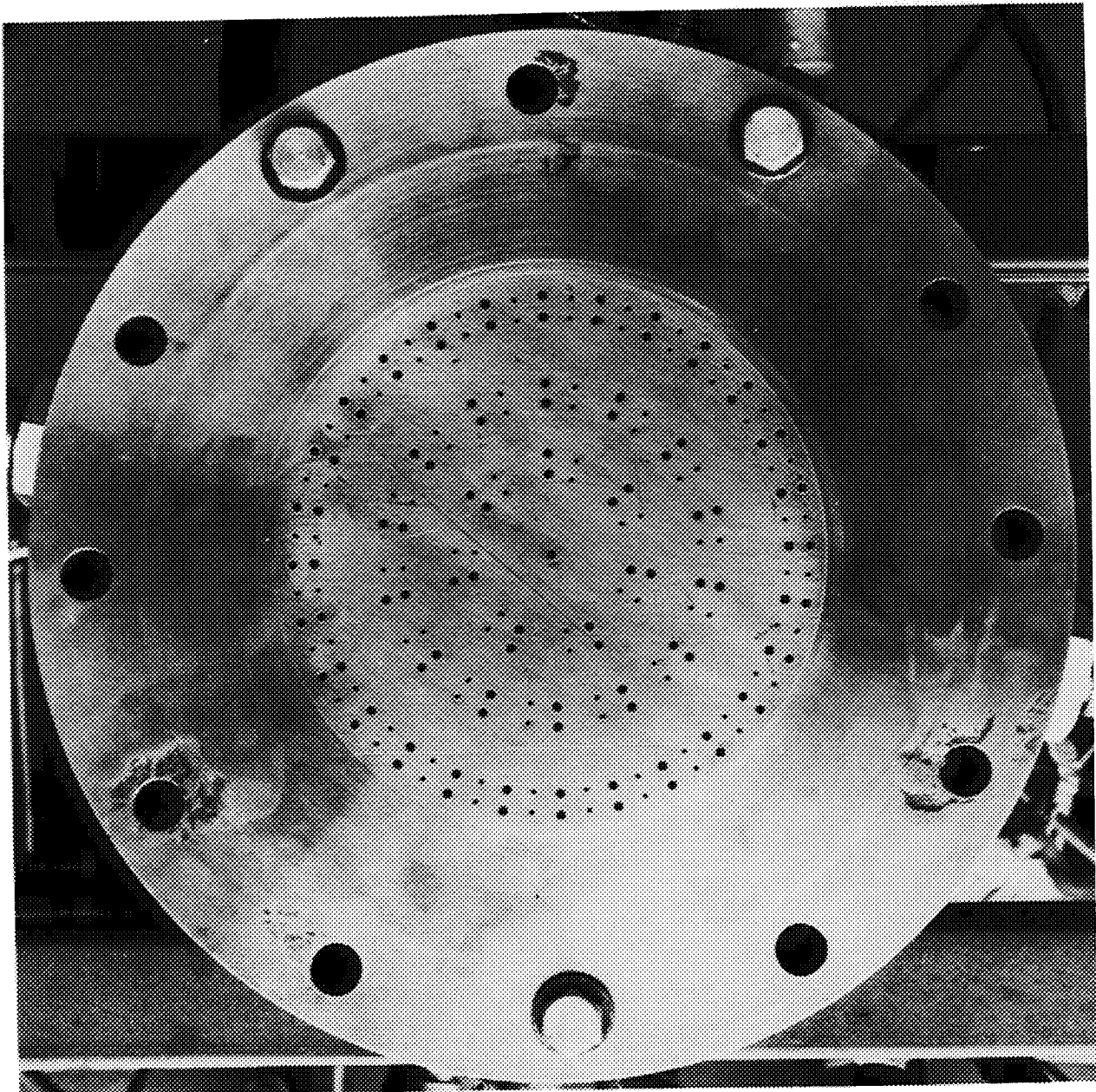
Figure 4. Face View of Doublet/Showerhead Injector Showing Orifice Pattern. Large Orifices: GH_2 Showerheads; Small Orifices: LF_2 Self-Impinging Doublets.

TABLE 2

DOUBLET/SHOWERHEAD INJECTOR, DESIGN PARAMETERS

	LF_2	GH_2
Number of orifices	98	99
Orifice diameter, inches	0.043	0.089
Doublet impingement angle, degrees	60	
Doublet impingement distance, inches	0.18	
Orifice L/D	6.5	3.5 to 4.9
Free stream L/D	4.9	

Alternate self-impinging LF_2 doublet elements and pairs of GH_2 showerhead orifices were located in three concentric rows, along diameters which, together with orifice spacing, were selected to provide uniform propellant distribution across the injector face. The outer row of fluorine doublets was canted 10 degrees inward to reduce asymmetrical wall heating and possible erosion by oxidizer impingement on the wall.

Fluorine feed passage velocity (from manifold to orifices) ranged from 3.1 ft/sec at the lowest flowrate to 13.4 ft/sec at the highest. Hydrogen feed passages were sized to provide less than 2 percent maximum difference in "driving" pressure between outer and inner orifices. Nominal vacuum thrust per element (consisting of an LF_2 doublet and two GH_2 showerhead orifices) ranged from 12.7 to 51.3 pounds at chamber pressures of 50 and 200 psia, respectively.

Orifice and manifold arrangement of the doublet/showerhead injector are sketched in Fig. 5; nominal and experimental pressure drops are given in Appendix B.
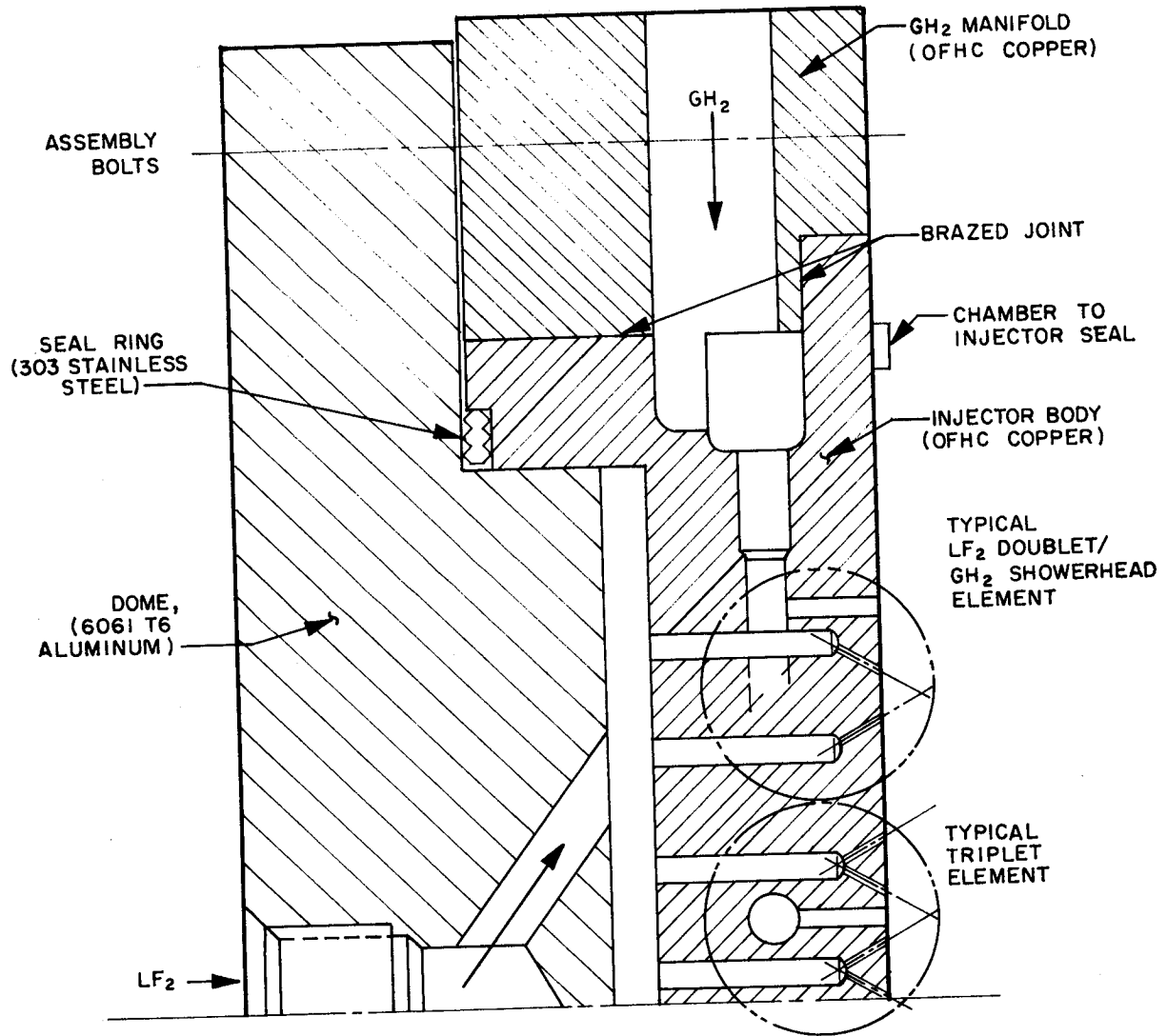
Figure 5. Method of Assembly of Injector, Fuel Manifold, and Oxidizer Dome, Showing Typical Orifice Feed Arrangements Used for the Triplet and Doublet/Showerhead Injector Patterns.

Triplet. Face pattern of the triplet injector is shown in Fig. 6. The important design parameters of this injector are given in Table 3.

TABLE 3

TRIPLET INJECTOR, DESIGN PARAMETERS

	LF_2	GH_2
Number of orifices	128	64
Orifice diameter, inches	0.039	0.109
Doublet impingement angle, degrees	60	
Impingement distance, inches	0.31	0.31
Orifice L/D	4.8	7.5
Free Stream L/D	9.0	

A "square" pattern was used to provide uniform propellant distribution across the injector face without excessive complication of the propellant feed passages. The triplet elements nearest the wall were oriented so that the fluorine fans were reasonably parallel to the wall, thus tending to minimize nonuniform heat flux to the chamber walls.

Fluorine feed passage velocity ranged from 3.0 ft/sec to 12/5 ft/sec; hydrogen feed passages provided less than 2 percent maximum difference in "driving" pressure between inner and outer orifices. Nominal vacuum thrust per element ranged from 19.3 to 78.5 pounds at 50- and 200-psia chamber pressure, respectively.

Figure 5 shows the orifice and manifold designs of the triplet injector; nominal propellant pressure drops and injection velocities are given in Appendix B.

21
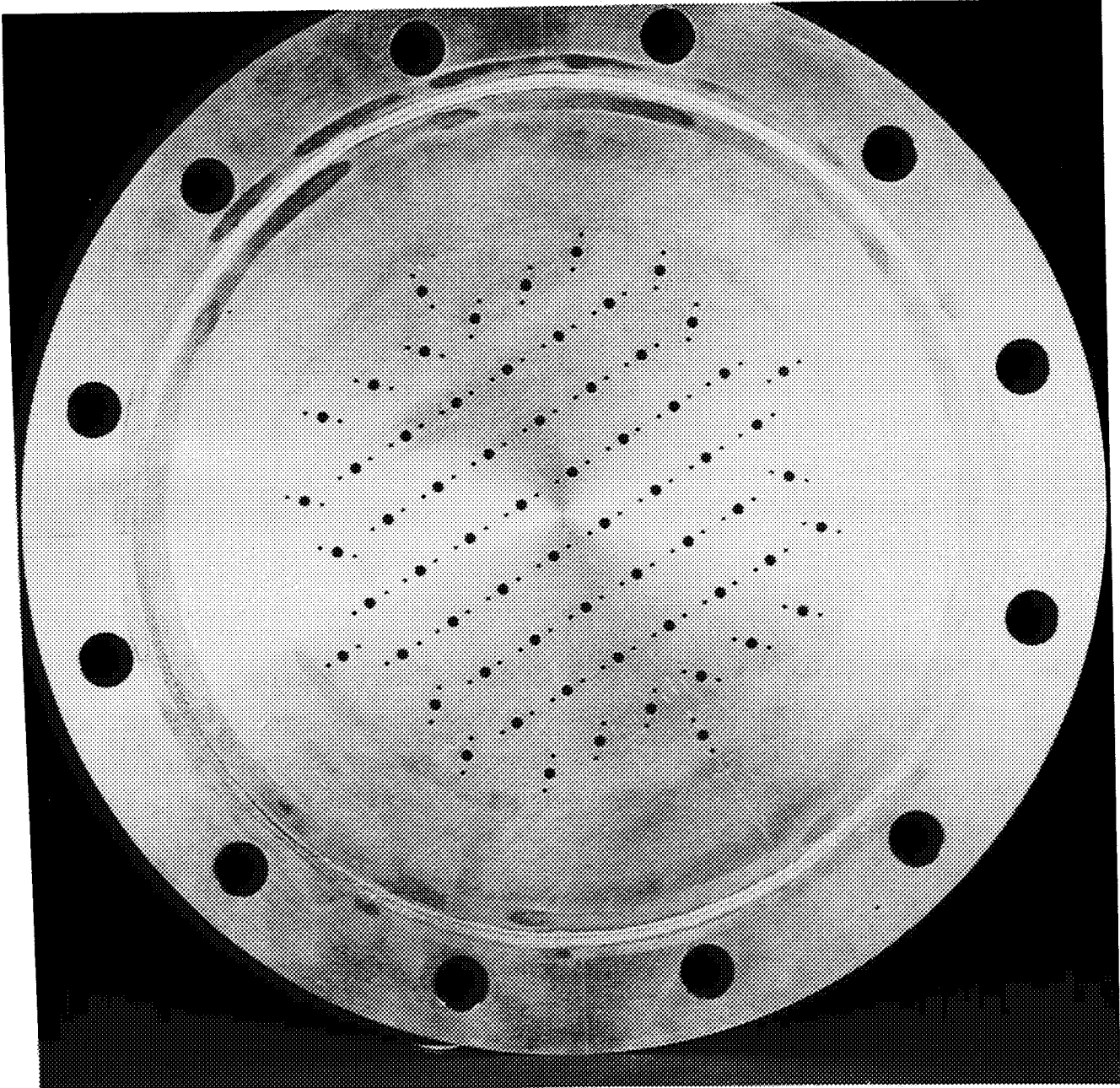
Figure 6. Face View of Triplet Injector Showing Orifice Pattern.
Large Orifices: GH_2 Showerheads; Small Orifices: LF_2
Self-Impinging Doublets.

Materials

The important injector material requirements were:

1. Suitable thermal conductivity characteristics to provide adequate cooling and protection from erosion

2. Compatibility with fluorine, hydrogen, and their combustion products

3. Good weldability or brazeability; this is required because the injector was welded to the annular fuel supply ring (Fig. 5) to provide positive assurance of separation of hydrogen from fluorine

4. Good workability, structural stability, and availability

These requirements are met by nickel and OFHC copper, with the latter as the material of choice except possibly for dependable integrity of weld or braze. This was ensured by designing the injector and fuel supply ring to provide a large braze surface extending in both radial and longitudinal directions (Fig. 5) to reduce thermal gradients across the braze seal during prefiring chilldown and firing, and by paying particular attention to dimensional control prior to brazing to ensure structural integrity of the braze joint.

THRUST CHAMBER

Chamber Design

A segmented, uncooled, calorimetric copper chamber was used consisting of three flanged segments and a nozzle section; its length could easily

be altered by removing one or more of the segments (Fig. 7 and 8). Additionally, design provisions were made for measurement of chamber wall heat flux.

The throat diameter was that required to produce nominal 2500-pound thrust at chamber pressure of 100 psia and mixture ratio of 12 for a 60:1 area ratio nozzle operating in vacuum. This expansion ratio was used in the altitude nozzle evaluation portion of the overall program (Task III). The actual expansion ratio used in the present experimental chamber was that for optimum expansion to test facility ambient pressure (13.8 psia), based on chemical equilibrium performance.

Pertinent chamber dimensions are noted in Table 4.

TABLE 4

THRUST CHAMBER DESIGN CHARACTERISTICS

Throat diameter, inches	4.20
Throat area, sq in.	13.85
Combustion zone diameter, inches	6.01
Combustion zone area, sq in.	28.41
Exit diameter, inches	5.80
Exit area, sq in.	26.38
Contraction ratio	2.05
Expansion ratio	1.90
Nominal characteristic length (L*), inches	30
Chamber length (injector to throat), inches	15.40
Contraction half angle, degrees	30
Expansion half angle, degrees	15
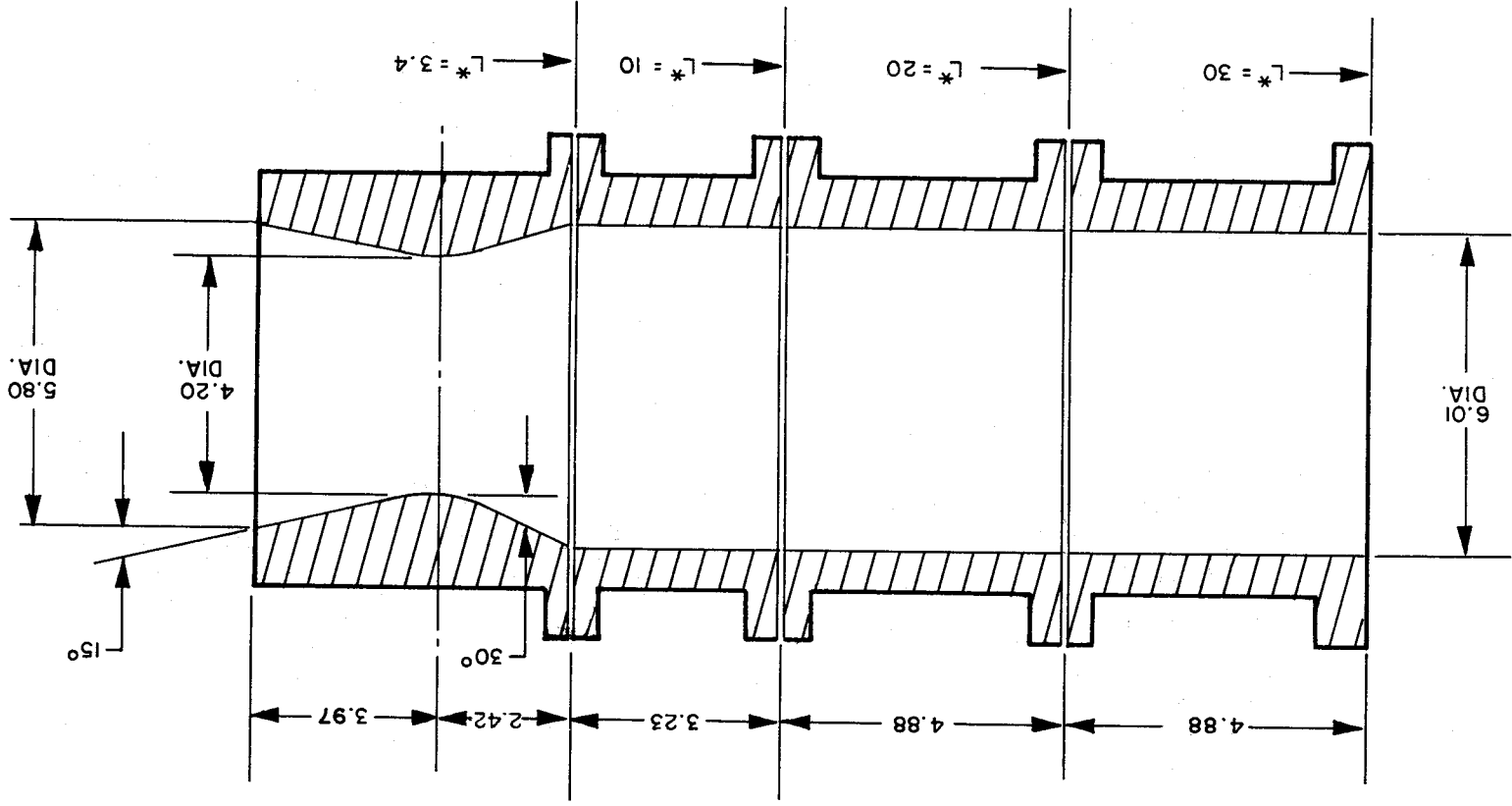
Figure 7. Thrust Chamber Schematic Showing Segmented Design and Dimensions.

25
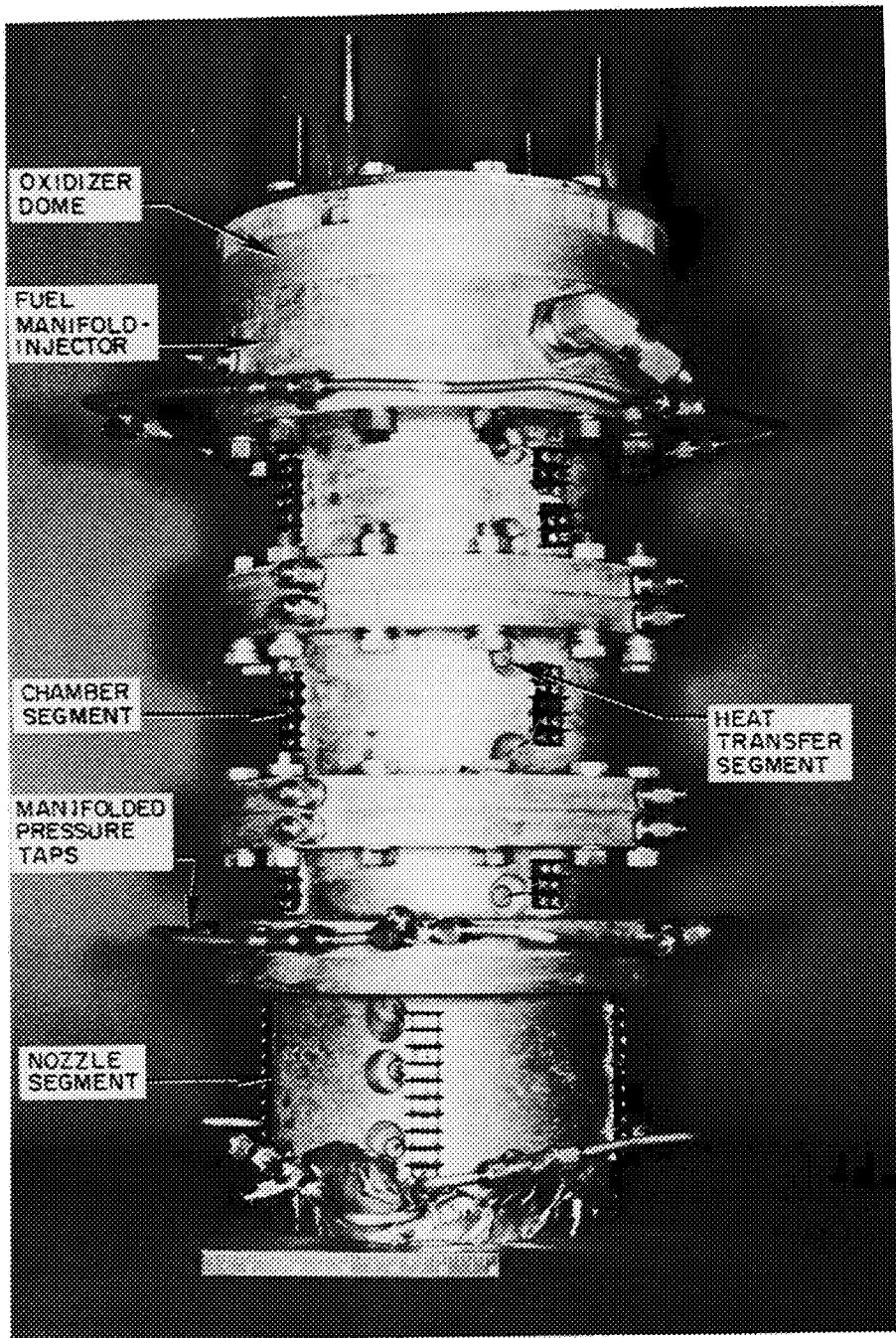
Figure 8. View of Assembled Thrust Chamber, Showing Segmented
Construction and Method of Joining.

Heat flux to the chamber and nozzle walls was determined by use of thermally isolated, half-inch-diameter segments machined into the chamber walls. Thermocouples peened to these segments provided cold-side temperature histories from which heat flux and heat transfer coefficients were calculated. Considerations involved in the design of the heat flux isolation areas are detailed in Appendix A. The final design consisted of four longitudinal rows of heat flux segments located approximately 90 degrees apart. The full-length chamber had eight elements per row, three in the nozzle and five in the combustion chamber; shorter length chambers retained the three nozzle segments and the appropriate number in the combustion chamber. Segment locations are indicated in Fig. 9.

PROPELLANT MANIFOLDS

Fuel Manifold

The fuel manifold was a machined ring fitting around the injector body and brazed to it (Fig. 5). Careful design of the mating surfaces permitted formation of a secure braze, as described above.

Oxidizer Dome

The oxidizer dome fabricated of 6061-T aluminum, was designed to set into the rear of the injector body, from which it was separated by a stainless steel serrated seal ring (Fig. 5). The ring serations on the aluminum dome against the copper injector provided a positive seal.
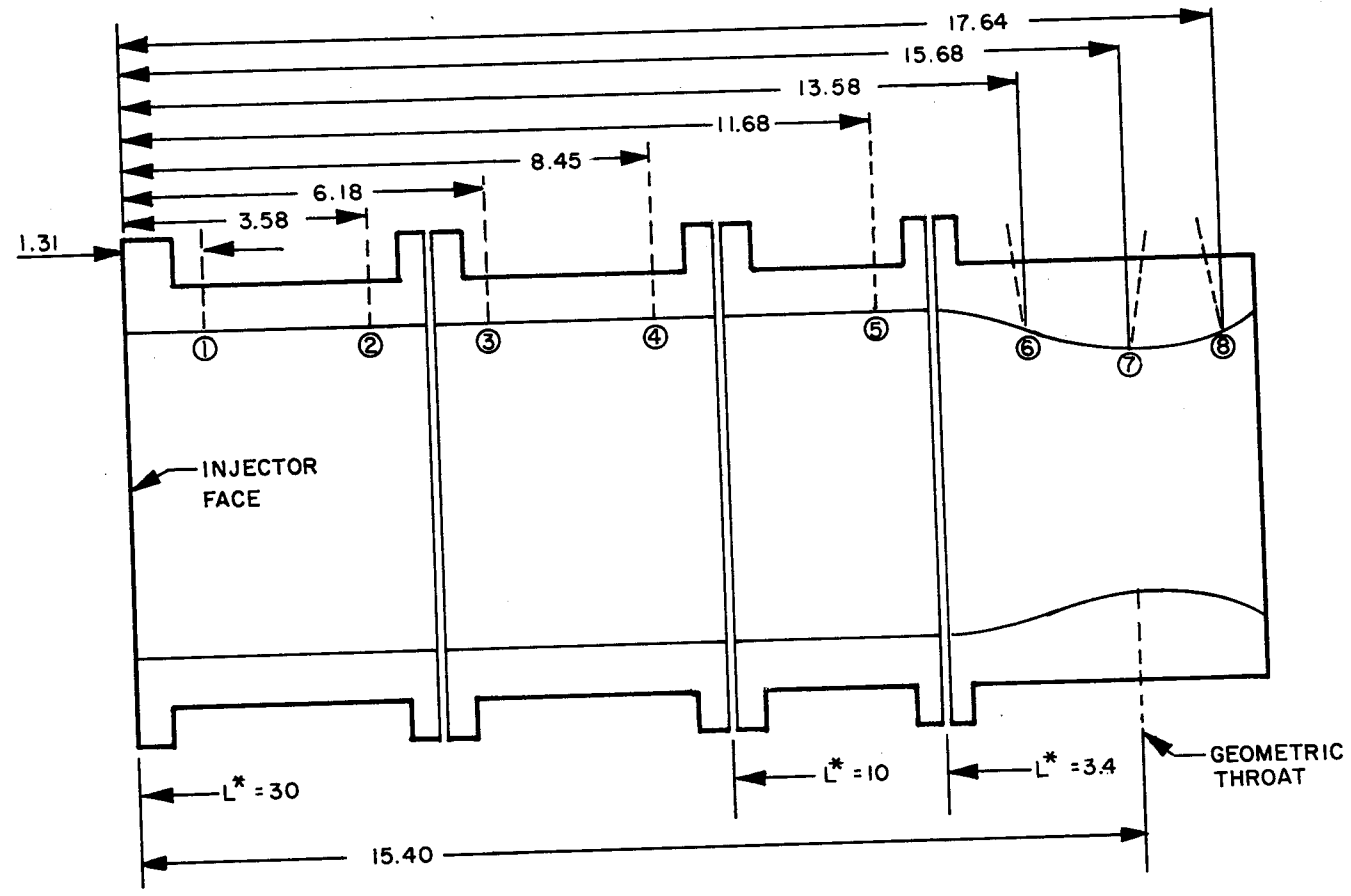
Figure 9. Thrust Chamber Schematic Showing Locations of Heat Transfer Isolation Segments in Chamber Wall. Circled Numbers Designate Axial Positions, for Reference.

EXPERIMENTAL FACILITIES AND PROCEDURES

TEST FACILITY

The experimental firings were carried out in the Propulsion Research Area fluorine facility. A schematic flow diagram of the stand is shown in Fig. 10. Liquid fluorine was obtained by condensation of GF_2 (supplied from manifolded 400-psi shipping cylinders) in a liquid nitrogen heat exchanger and was stored in a prechilled, 43-gallon, LN_2-jacketed run tank. The condensation and transfer procedures, developed in several previous experimental programs, were carried out routinely and without difficulty. Following completion of a set of firings, remaining LF_2 in the tank was allowed to gasify back into the supply bottles by dumping the LN_2 in the cooling jackets and replacing it first with flowing GN_2, then with water.

The fluorine flow system was chilled with jacketed LN_2 from the condenser to the main valve, as shown in Fig. 10. In addition, use of a three-way main oxidizer valve permitted prerun chilldown of the manifold and injector by an LN_2 bleed directly through the injector and thrust chamber, thus preventing fluorine flashing in the initial portion of the firing and minimizing flow transients. Filtered helium was used for fluorine tank pressurization.

Gaseous hydrogen was supplied from the area tank farm through a suitable pressure regulating system. Gaseous nitrogen purges were used on both oxidizer and fuel sides.

JACKET
FLUSH

JACKET
PURGE

SHUTOFF
LL

GN₂

SHUTOFF

GH₂   GN₂

SHUTOFF

DUMP

VENT

PRESS. VALVE

LF₂
TANK
GAL

GN₂

VENT

GN₂

He

SONIC
VENTURI

MAIN

SHUTOFF

LINE CHILL

PURGE

GN₂

INJ. CHILL

BY-PASS

PURGE

FLOWMETER
CHECK VALVE
FILTER
HAND VALVE
PNEUMATIC
VALVE 2-WAY
PNEUMATIC
VALVE 3-WAY
SOLENOID
VALVE
PRESSURE
REGULATOR
MOTORIZED
LOADER
HAND LOADER
PRESSURE
GAGE
PRESSURE
TRANSDUCER
SAFETY HEAD
RELIEF VALVE

30-2

Figure 10. Schematic Flow Diagram of Test Stand Yoke, Propulsion
Research Area, as Used in LF_2/GH_2 Experimental Program

30-1

INSTRUMENTATION

A schematic diagram indicating instrument locations is shown in Fig. 11. Redundant measurements were made of all important experimental parameters to increase data reliability. The particular transducers used for the various types of measurements are described below.

Thrust

The thrust chamber mount was supported on flexures which allowed free movement parallel to the engine axis, restrained in the thrust direction by a Baldwin-Lima-Hamilton double-bridge load cell (Model U-382).

Pressure

All pressures were measured with bonded strain gage transducers (Taber "Teledyne" Series 206). Chamber pressures were determined at three axial locations: near the injector face $(P_c - 1)$, at the start of nozzle convergence $(P_c - 2)$, and in the divergent section of the nozzle at $\epsilon = 1.5$ $(P_c - 3)$. At each location, four circumferential taps, 90 degrees apart, were manifolded together, with two pickup lines from each manifold to separate transducers. The other pressure measurements indicated in Fig. 11 were made with close-coupled transducers at each location.

Flowrate

Hydrogen. Hydrogen flowrate was measured by a sonic venturi meter (Flow-Dyne Model N-160350), with 0.3492-inch throat diameter. Redundant measurements of plenum pressure and temperature were made, as shown in Fig. 11.

31

INSTRUMENTATION

1. FLUORINE TANK PRESSURE
2. FLUORINE TANK TEMPERATURE
3. FLUORINE SUPPLY TEMPERATURE
4. FLUORINE FLOWRATE
5. FLUORINE FLOWRATE
6. FLUORINE SUPPLY TEMPERATURE
7. HYDROGEN SUPPLY PRESSURE
8. VENTURI INLET TEMPERATURE
9. VENTURI INLET TEMPERATURE
10. VENTURI INLET PRESSURE
11. VENTURI INLET PRESSURE
12. THRUST
13. HYDROGEN MANIFOLD PRESSURE
14. FLUORINE MANIFOLD PRESSURE
15. INJECTOR-END CHAMBER PRESSURE
16. INJECTOR-END CHAMBER PRESSURE
17. NOZZLE INLET CHAMBER PRESSURE
18. NOZZLE INLET CHAMBER PRESSURE
19. NOZZLE DIVERGENGE CHAMBER PRESSURE
20. NOZZLE DIVERGENCE CHAMBER PRESSURE

Figure 11. Schematic Flow Circuit of Experimental System Showing Types and Locations of Instrumentation Transducers.

Fluorine. Two turbine flowmeters in series were used to measure volu-
metric fluorine flowrates: a Fischer-Porter Model RF-1-50 and a Flocon
Model 1000-FT with Stellite-25 bearings.

Temperature

Fluorine. Reliable measurement of fluorine mass flowrate requires deter-
mination of liquid density as well as of volumetric flowrate. Density
of liquid fluorine is a moderately sensitive function of temperature, as
shown in Fig. 12. Hence, it was important to make careful measurements
of fluorine temperature as close to the flowmeters as practical. This
was done by use of two shielded platinum resistance bulbs (Rosemount
Model 176) immersed in the liquid stream, one upstream of the first flow-
meter and the other downstream of the second. These sensors are very
sensitive to temperature changes in the cryogenic region and are the pre-
ferred method of measurement. The first seven firings of the experimental
series were made prior to installation of the resistance bulbs. In these
firings, iron-constantan thermocouples in wells were used to measure
fluorine temperature; these usually gave erratic, nonduplicating read-
ings, whereas resistance bulb temperature measurements were within 1 to
2 degrees of each other.

Hydrogen. Hydrogen temperatures in the venturi plenum were measured with
iron-constantan thermocouples. Because temperatures were ambient and
flowrate is a function of the square root of absolute temperature, these
measurements were satisfactory.

Chamber Wall Isolation Segments. Temperature histories of the heat trans-
fer isolation segments (Appendix A) were measured by means of 10-mil
chromel-alumel thermocouples peened into the segment material.
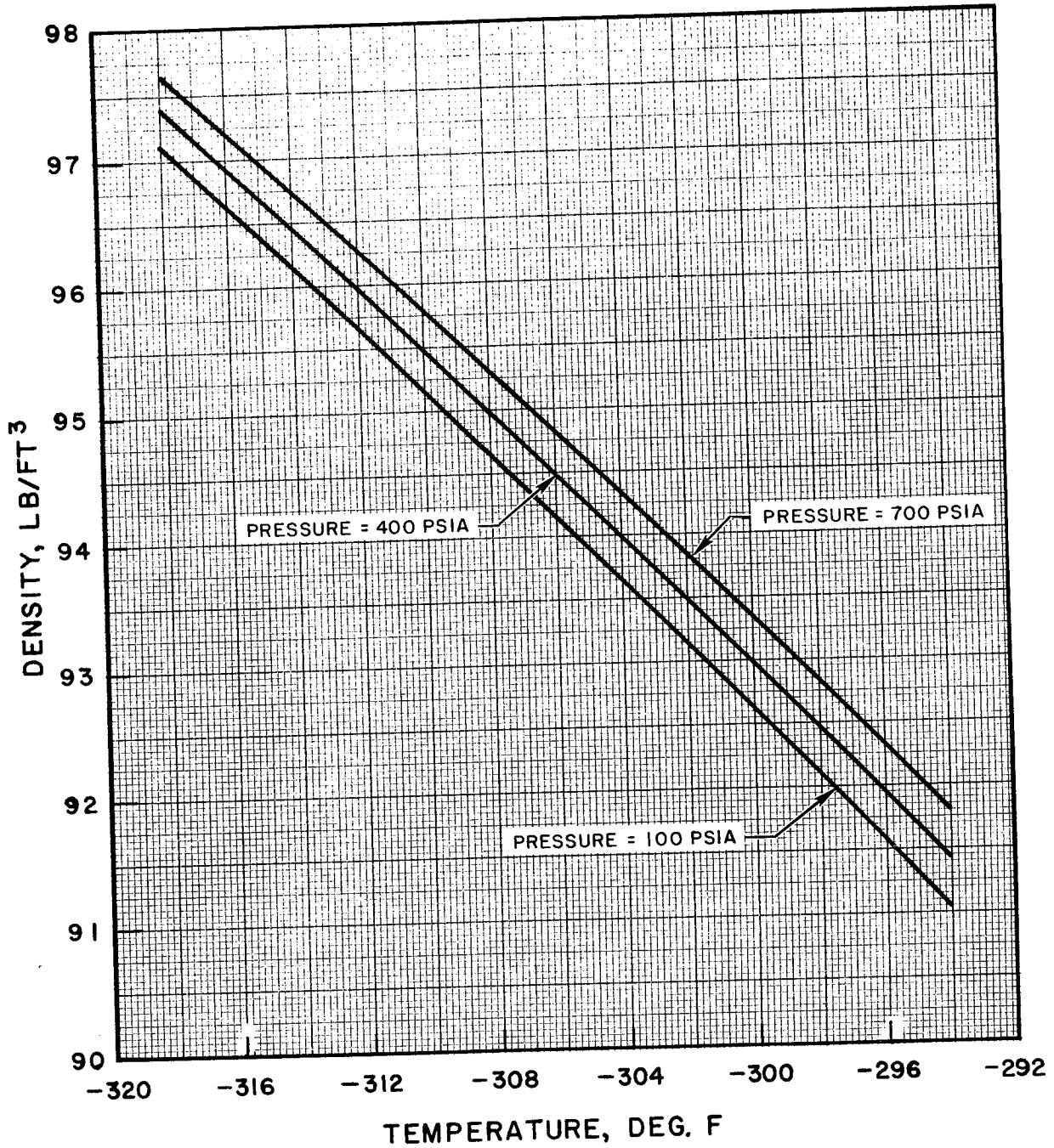
Figure 12. Variation of Liquid Fluorine Density with Temperature
at Indicated Pressures. Data Taken from Rocketdyne
Report No. PR-4114-1019, "Thermodynamic Property Values
of Gaseous and Liquid Fluorine", 19 November 1964.

Data Recording

All pressure, temperature, and flow measurements were recorded on tape
during each firing by means of a Beckman Model 210 Data Acquisition and
Recording System. This system acquires analog data from the transducers,
which it converts to digital form in binary-coded decimal format. The
latter are recorded on tapes which are then used for computer processing.

The Beckman Data Acquisition Unit sequentially samples the input channels
at a rate of 5625 samples per second. Programmed computer output consists
of tables of time vs parameter value (in engineering units), printed out
as the instantaneous values at approximately 10-millisecond intervals
during the firing, together with calibration factors, prerun and postrun
zero readings, and related data. The same computed results are machine
plotted and displayed as CRT outputs on appropriately scaled and labeled
grids for simple determination of gradients, establishment of steady
state, etc.

Primary data recording for these firings was on the Beckman 210 System.
In addition, the following auxiliary recording systems were employed:

1. An 8-channel Brush Mark 200 recorder was used in conjunction
   with the Beckman unit primarily to establish time intervals for
   computer data reduction and, additionally, for "quick-look"
   information on the most important parameters. This is a direct-
   inking system, with display on high-gloss, graduated paper mov-
   ing at 20 mm/sec.

2. A CEC, 36-channel, direct-reading oscillograph was used as
   backup for the Beckman 210 System and for indication of oscilla-
   tory combustion.

3. Direct-inking graphic recorders (DIGR's), either Dynalog rotary chart or Esterline-Angus strip chart, were used to set prerun fluorine tank and hydrogen supply pressures, for exclusive recording of propellant manifold pressures, to monitor prerun chilldown time, to provide quick-look information, and as secondary backup to the Beckman and oscillograph recorders.

4. An Esterline-Angus 20-channel event recorder was used for direct-inking recording of main propellant valve signal and travel, as well as for chart drive and camera actuations.

CALIBRATION PROCEDURES

Transducer calibrations were used not only to obtain appropriate factors for test data reduction, but to develop statistical histories for each transducer, so that estimates of short-term and long-term deviations could be made and probable error bands calculated (see Appendices C and E for detailed discussions). The calibration methods used for the various types of transducers are described below.

Thrust

The thrust-measuring load cell was calibrated in-place. A permanently mounted, manually operated, hydraulic force cell was employed which deflected the load cell exactly as did the engine, through a yoke-tension rod system. Known loads were applied to the force cell through a Morehouse compression-type, temperature-compensated, proving ring calibrated by the National Bureau of Standards.

This "end-to-end" calibration technique (i.e., one in which the complete measuring system is included, in addition to the transducer itself) provides for reliable determination of the thrust force acting on the load cell. For this thrust to be equal to that actually resulting from a firing, free movement of the engine mount is desirable; hence, flexible metallic tubing is generally used for propellant supply lines to the manifolds. Such tubing was used in the hydrogen feed line (Fig. 13). For the fluorine inlet line, special monel-lined flexible tubing was specified, because of previous experience in which flexible lines with stainless steel inner corrugations failed unpredictably in LF_2 service. However, because of long lead time for delivery of this item, rigid stainless steel tubing was used instead. An extensive series of thrust calibrations was made with the rigid line in place, chilled and unchilled, pressurized and unpressurized, to determine possible effects of line temperature and pressure on the thrust readings. The only significant effect found was that of line chill, which changed the zero setting, in effect, preloading the cell. Net transducer outputs (actual output less zero reading) over the entire calibration range were not affected by line condition (ambient, unpressurized; ambient, pressurized; chilled, unpressurized; chilled, pressurized). Line pressurization to run level (450 psi) had no significant effect on load cell output with either chilled or ambient temperature lines. These results indicated that load cell calibrations could be made with the fluorine inlet line at ambient temperature, but that prerun and postrun zero readings should be taken with the line chilled to the same extent as during firing. This was done by monitoring the output of an iron-constantan thermocouple soldered to the line. Further, an S-shaped LF_2 inlet line minimized the effect of line stiffness on thrust measurement.

No differences in transducer outputs were observed when the calibration series was repeated with a flexible line substituted for the rigid tubing. Hence the latter was used throughout the experimental program.
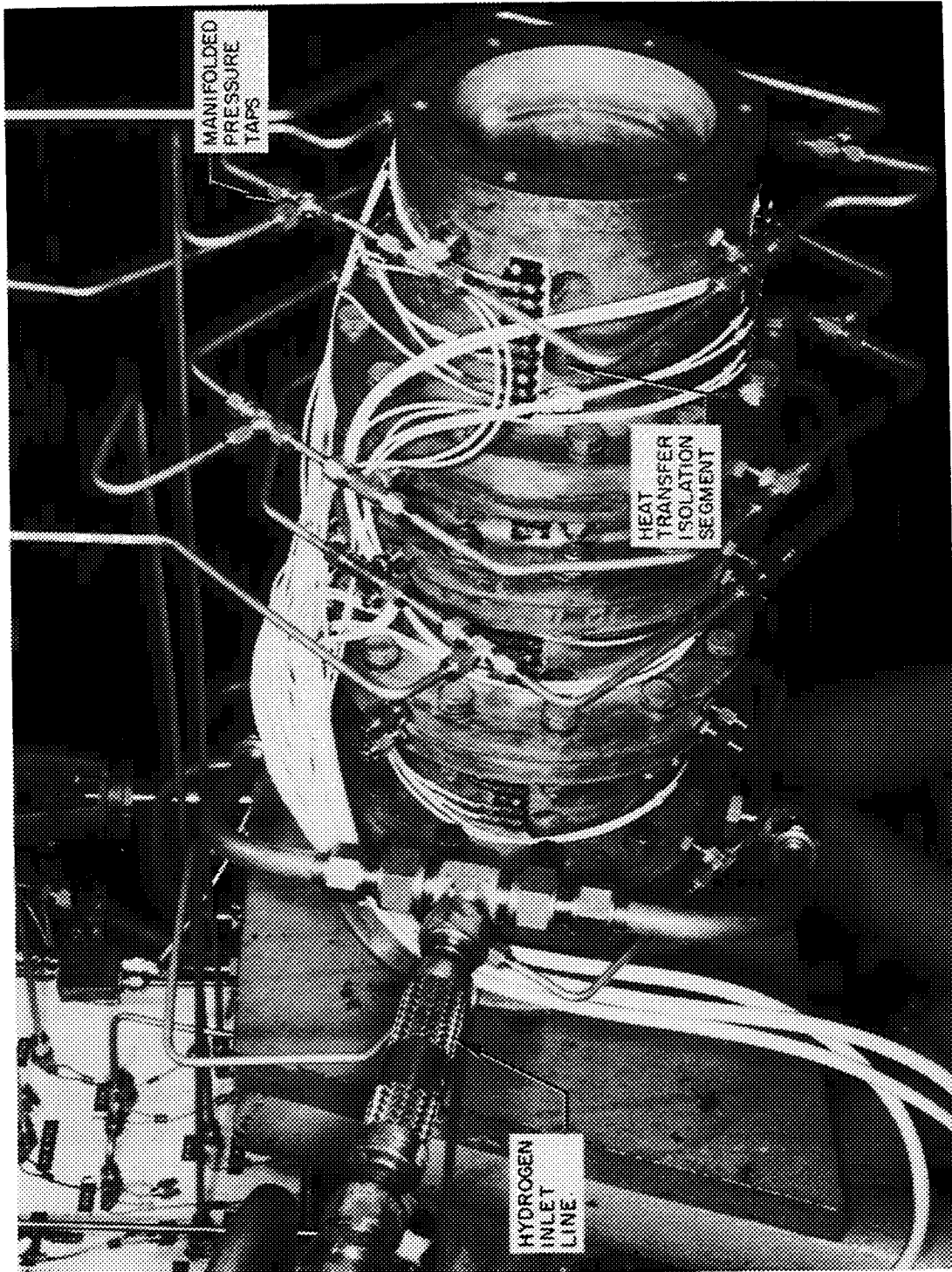
Figure 13. View of 30-inch L* Chamber Mounted on Thrust Stand.

Thrust calibrations for the first three firings of this series were made by an older procedure in which the oxidizer inlet line was chilled before start of the calibration. This neglected the gradual increase in line temperature during the calibration and the accompanying zero shift. A more reliable method, used for all subsequent firings, was to calibrate with all lines at ambient temperature, to obtain the thrust/load cell output curve. Zero readings were obtained immediately before and after every firing, with LF_2 inlet line chilled to run temperature. Because the thrust/output factors were not changed by the ambient-chilled zero shift, the ambient calibration was valid.

Pressure

Pressure transducers were calibrated end-to-end by mounting them on stand manifolds, in which pressures were read with high-precision Heise Bourdon-tube gages. The latter were calibrated periodically on Ruska dead-weight testers. Maximum length of pickup line from pressure tap to transducer was 3 feet.

Flowrate

Fluorine. Calibrations of the turbine flowmeters to obtain volume flow-rates as functions of rotational speeds were made with water. Transfer of these cycles-per-gallon factors to liquid fluorine usage requires application of corrections which allow for the differences in temperature and viscosity between water and LF_2. The temperature correction (70 F to -310 F), which is a function of meter material and not of meter size, has been estimated as 1.005 (Ref. 11) and 1.009 (Ref. 12), average: 1.007.

The viscosity correction, which is a boundary layer phenomenon and therefore depends on flowmeter size, was estimated as 0.992 (1-inch meter, Ref. 11), so that the net correction applicable to the water calibration factors was (1.007 x 0.992), or 0.999. This was within the readability limits of meter output and was therefore considered negligible. Hence volumetric flow factors determined with ambient-temperature water were used for liquid fluorine without correction.

<u>Hydrogen</u>. The sonic venturi meter was calibrated with hydrogen by the manufacturer.* Mass flowrate was determined from the following equation:

$$\dot{w} = \frac{K P}{\sqrt{T}} \tag{3}$$

where

$\dot{w}$ = hydrogen flowrate, lb/sec

P = static pressure in venturi plenum, psia

T = temperature of gas in venturi plenum, R

K = flow coefficient

The calibration established curves which gave values of K as functions of gas pressure and temperature. The flow coefficient curves were calculated from the A.S.M.E. equations (Ref. 13).

Calibration procedures for the pressure and temperature sensors used in conjunction with the venturi meter are described in another part of this section.

---

*Flow-Dyne Engineering, Inc., 1017 Norwood Street, Fort Worth, Texas 76107

Temperature

Resistance Thermometers. Resistance of the platinum thermometers used in the LF_2 line was converted to millivolt output by a triple-bridge system. This was calibrated by substituting a decade resistance box for the sensor, and setting it at various resistances corresponding to a temperature-resistance calibration supplied by the manufacturer* for each instrument. These precision platinum resistance sensors have no significant calibration drift. They were checked upon receipt by immersion in liquid nitrogen and liquid oxygen; temperature readings were correct within the limits of readability.

Thermocouples. Thermocouples were used on the basis of the standard NBS millivolt/temperature tables. Thermocouple recorders were electrically calibrated.

Calibration Frequency

Pressure transducers, thrust load cell, and resistance thermometers were calibrated before every set of firings (comprising three or four successive runs on the same day). Fluorine flowmeters were calibrated immediately prior to start and immediately following completion of the experimental program, with no significant variation in flow factors between the two calibrations. The hydrogen sonic venturi was calibrated immediately preceding start of the program.

---

*Rosemount Engineering Co., 4900 West 78th Street, Minneapolis 24, Minn.

FIRING PROCEDURES

Fluorine System Passivation

Prior to assembly, fluorine system components were carefully and thoroughly cleaned in accordance with standard prescribed procedures (Ref. 14). Passivation of the assembled system (to main oxidizer valve), by provision of protective fluoride films on exposed surfaces, was carried out as follows: low-pressure gaseous fluorine was introduced into the system and maintained for successive 15-minute periods at 5, 10, and 15 psi; finally, 20 psi was maintained for several hours.

The feed line-thrust chamber system downstream of the main valve was passivated immediately before each set of firings by flowing gaseous fluorine through the system for short intervals of time.

Run Procedure

Before each firing, liquid nitrogen was bled through the main oxidizer valve to chill the fluorine inlet line to the temperature at which thrust zeros were to be taken and which was maintained by LF_2 during the run. The firing itself was sequenced through an automatic timer which controlled operation of propellant main valves, chart drives, and cameras. Run durations were approximately 3.0 seconds at 100-psia chamber pressure, slightly longer at 50 psia, and slightly shorter at 200 psia.

A slight fuel lead (approximately 50 milliseconds) was maintained at the start of the firing, together with a fuel-rich shutoff (approximately 200 milliseconds). Motion picture coverage, primarily for hardware monitoring, included three Fastax and two Bell and Howell cameras.

RESULTS

Results reported in this section are for the experimental portion of the present program, which is Task II of the overall program (see Introduction). Results of Task I(a), which is the other part of the present program and comprises injector analysis and design, were presented in the section describing experimental apparatus.

To carry out Task II objectives, a total of 45 experimental firings was made, of which one was a preliminary checkout run and two were terminated prematurely. Results obtained from the remaining 42 firings are presented below.

PERFORMANCE

Data Summary

The basis of comparison of injector performance was corrected c^* efficiency, obtained from independent measurements of chamber pressure and thrust. Characteristic velocity was calculated from the standard equations, with suitable corrections for energy losses, throat area changes, and departures from ideal one-dimensional flow. Details of the procedures used for these computations and for estimation of applicable correction factors are given in Appendix D.

A measurement error analysis was carried out (Appendix E) to obtain estimates of the uncertainty intervals associated with the determinations of c^* efficiency from both chamber pressure and thrust. This analysis indicated the following probable error bands over the entire chamber

pressure/mixture ratio matrix:

± 1.0 percent at 95 percent confidence level (2σ)

± 0.5 percent at 68 percent confidence level (1σ)

A summary of the performance results is given in Table 5, in which the column headings refer to the following parameters:

P_c-1: static pressure measured 0.4 inch downstream of injector face

P_c-2: static pressure measured 0.4 inch upstream of start of nozzle convergence

P_c-3: static pressure measured in divergent portion of nozzle at $\epsilon = 1.5$

$(P_c)_o$: stagnation chamber pressure, derived from P_c-2

$\dot{w}_T$: total propellant flowrate

A_t: measured geometric throat area

F(meas); measured thrust

F(vac): vacuum thrust, $F(vac) = F(meas) + P_a A_e$

where P_a = ambient pressure

A_e = area of nozzle exit

c^*_{theo}: theoretical characteristic velocity based on shifting equilibrium

η_{c^*}: c* efficiency, based on P_c or F

Values of c* efficiency listed in Table 5 are based on theoretical, shifting-equilibrium characteristic velocity. Curves of these theoretical values are shown in Fig. 14 at the three chamber pressure levels used

Run Number	Injector Type	L*, inches	P_c-1, psia	P_c-2, psia	P_c-3, psia	$(P_c)_o$, psia	$\dot{w}_T$, lb/sec	Mixture Ratio	A_t, sq in.
156	Doublet	30	99.8	92.8	17.1	97.9	5.55	11.7	13.80
157	→	30	97.5	92.9	16.7	98.0	5.47	8.9	13.80
158		30	99.4	93.0	17.1	98.1	5.61	14.3	13.80
159		30	48.6	45.6	8.0	48.1	2.67	10.6	13.80
160		30	46.8	44.6	8.1	47.1	2.78	11.6	13.80
161		30	48.7	45.3	9.0	47.8	2.87	15.0	13.80
162		30	47.8	45.2	7.7	47.7	2.73	8.4	13.80
163	Doublet	30	172	161	28.4	170	9.31	10.1	13.80
164	→	30	201	187	33.7	197	11.11	12.0	13.80
165		30	205	189	34.5	199	11.29	15.4	13.80
166		30	47.6	45.5	8.7	48.0	2.67	11.5	13.80
167		30	48.9	46.1	7.8	48.6	2.70	8.7	13.80
168		30	48.1	45.2	8.6	47.7	2.71	13.6	13.80
169		30	100.7	93.9	16.8	99.1	5.54	12.1	13.80
170		30	100.1	94.1	16.7	99.3	5.66	15.4	13.80
171		30	100.9	95.4	16.6	100.6	5.44	9.0	13.80
172	Triplet	30	48.9	46.0	9.7	48.5	2.67	10.7	13.80
173	→	30	49.5	46.6	9.0	49.2	2.75	8.5	13.80
174		30	49.5	46.3	10.5	48.8	2.84	14.5	13.80
175		30	49.5	46.4	10.6	49.0	2.82	14.6	13.80
177		30	99.3	93.2	16.4	98.3	5.46	11.6	13.80
178		30	99.8	93.7	16.8	98.9	5.58	14.6	13.80
179		30	100.0	94.6	16.4	99.8	5.44	9.3	13.80
192		30	192	183	32.7	193	10.71	11.8	13.80
193		30	198	180	32.0	190	11.07	15.6	13.80
194		30	195	182	32.2	192	10.61	9.1	13.80
202	Triplet	3.4	-	-	15.3	-	5.46	11.8	13.80
203	→	3.4	-	-	18.1	-	5.61	15.2	13.80
204		3.4	-	-	14.5	-	5.66	9.3	13.80
205	Doublet	10	90	87	15.5	92	5.46	12.3	13.80
206	→	10	100	96	17.3	101	5.73	15.3	13.80
207		10	95	92	16.3	97	5.44	9.2	13.80
208		3.4	-	-	16.7	-	5.45	12.7	13.76
209		3.4	-	-	19.4	-	5.73	15.5	13.76
211		3.4	-	-	18.5	-	5.24	8.9	13.76

*Peak-to-peak oscillation amplitude >5 percent of mean
**Peak-to-peak oscillation amplitude <5 percent of mean
(1)Same as shown on page 46

...eas), ...unds	F(vac), pounds	c*(theo), ft/sec	η_{c*} (corr),% Based on P_c	η_{c*} (corr),% Based on F	Remarks
...541	1903	7770	95.9	95.9	(1)
...506	1868	7975	95.0	95.9	(1)
...478	1840	8120			Combustion oscillation at 250 cps*
...490	3852	7840	95.0	97.2	
...420	3782	8077	97.8	96.3	
...531	3893	8248	99.8	98.3	
...679	2041	8635	98.0	98.3	

...own for run 234

TA SUMMARY

(meas), pounds	F(vac), pounds	c*(theo), ft/sec	η_{c*} (corr),% Based on P_c	η_{c*} (corr),% Based on F	Remarks
1463	1825	8023	97.8	94.9	LF_2 temperatures and/or thrust
1464	1826	8179	97.5	94.5	calibrations are uncertain in
1442	1804	7895	98.5	94.3	Runs 156-162. These runs are
559	921	7991	100.6	100.2	repeated in Runs No. 166 through
550	912	7943	95.5	96.2	171.
571	933	7768	95.8	97.2	
571	933	8130	96.0	97.7	
2850	3212	8150	99.5	97.0	
3371	3733	8090	97.2	95.0	
3412	3774	7915	98.8	96.5	
550	912	7950	100.6	99.3	
577	939	8110	99.3	99.1	
561	923	7845	100.3	100.3	
1519	1881	8005	99.4	97.4	
1524	1886	7830	99.8	97.8	
1565	1927	8171	100.6	99.5	
562	924	7985	101.7	99.9	
604	966	8125	98.5	99.9	
594	956	7798	98.6	99.7	
585	947	7794	99.5	99.4	
1526	1888	8028	99.8	99.0	
1535	1897	7878	100.1	99.0	
1551	1913	8152	100.1	99.2	
3311	3673	8100	98.7	96.8	
3363	3725	7907	96.3	97.3	
3303	3665	8243	97.4	95.9	
1293	1655	8017			Combustion oscillation at 90 cps*
1396	1758	7845	(1)	90.9	
1452	1814	8152			Combustion oscillation at 90 cps*
1394	1756	7995			Combustion oscillation at 300 cps*
1463	1825	7838	(1)	92.5	
1479	1841	8158			Combustion oscillation at 300 cps*
1310	1672	7975			Combustion oscillation at 250 cps*
1340	1702	7827	(1)	86.4	Combustion oscillation at 250 cps**
1302	1664	8180	(1)	88.4	

Run Number	Injector Type	L^*, inches	P_c-1, psia	P_c-2, psia	P_c-3, psia	$(P_c)_o$, psia	$\overset{\circ}{w}_T$, lb/sec	Mixture Ratio
232	Triplet	10	102	96	16.9	101	5.81	16.4
233	↓	10	100	95	16.2	100	5.56	12.7
234		10	88	83	14.2	88	5.53	9.6
235	Triplet	30	207	185		195	11.55	16.7
236		30	200	188	34.0	198	11.12	12.3
237	↓	30	206	193	34.2	204	10.99	9.1
238		30	105	100	16.1	106	5.53	4.1

*Peak-to-peak oscillation amplitude >5 percent of mean; therefore,
(1) η_c^* based on chamber pressure is not presented for the short
  L^* firings because of combustion occuring downstream of the
  pressure measurement location

in the present investigation. The performance calculations were made on the basis of LF_2 injected at -306 F and GH_2 injected at 77 F, both very close to the experimental conditions.

Effect of Mixture Ratio and Chamber Pressure
on Performance

The important consideration in this program was injector performance in the 30-inch L* chamber over the specified ranges of chamber pressure and mixture ratio. Corrected c* efficiency in this chamber, calculated independently from measurements of chamber pressure and thrust, is plotted as a function of mixture ratio at each of the three nominal chamber pressures in Fig. 15 (doublet/showerhead injector) and Fig. 16 (triplet injector).

Figures 15 and 16 include all experimental data obtained with the 30-inch L* chamber, except those of the first seven firings (Runs No. 156 to 162), in which LF_2 temperature measurements were uncertain and/or prerun thrust zeros were taken with insufficiently cooled oxidizer lines, as described in a previous section of this report. These firings were repeated (Runs No. 166 to 171). Minor gas leaks between the injector and chamber were evident in three of the triplet injector firings at 200 psia (Runs No. 192 to 194). Data from these runs, however, are quite comparable to data from subsequent firings without leaks under the same conditions (Runs No. 235 to 237) and are therefore included in Fig. 16. It may be noted that several of the η_c* efficiencies shown in Fig. 15 and 16 are slightly greater than 100 percent. However, the deviations from the mean curve drawn through the data is well within experimental accuracy as indicated in Appendix E, Table E-1.

Agreement between values of corrected c* efficiency obtained from measurements of chamber pressure and thrust is good; the average deviation from the mean, for all of the firings in the 30-inch L* chamber with both injectors, is ±0.7 percent.
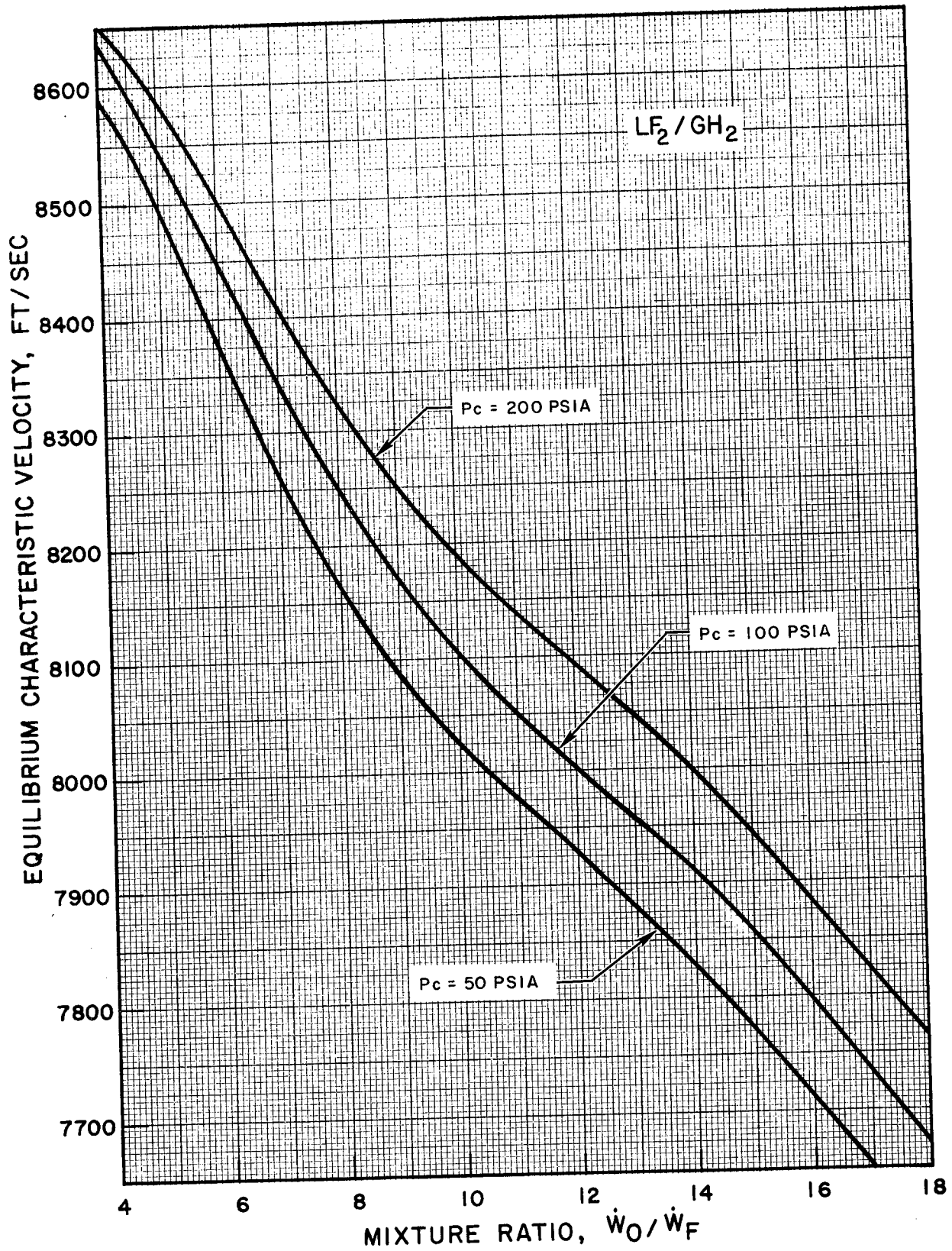
Figure 14. Theoretical LF_2/GH_2 Shifting Equilibrium Characteristic Velocity at Indicated Chamber Pressures.
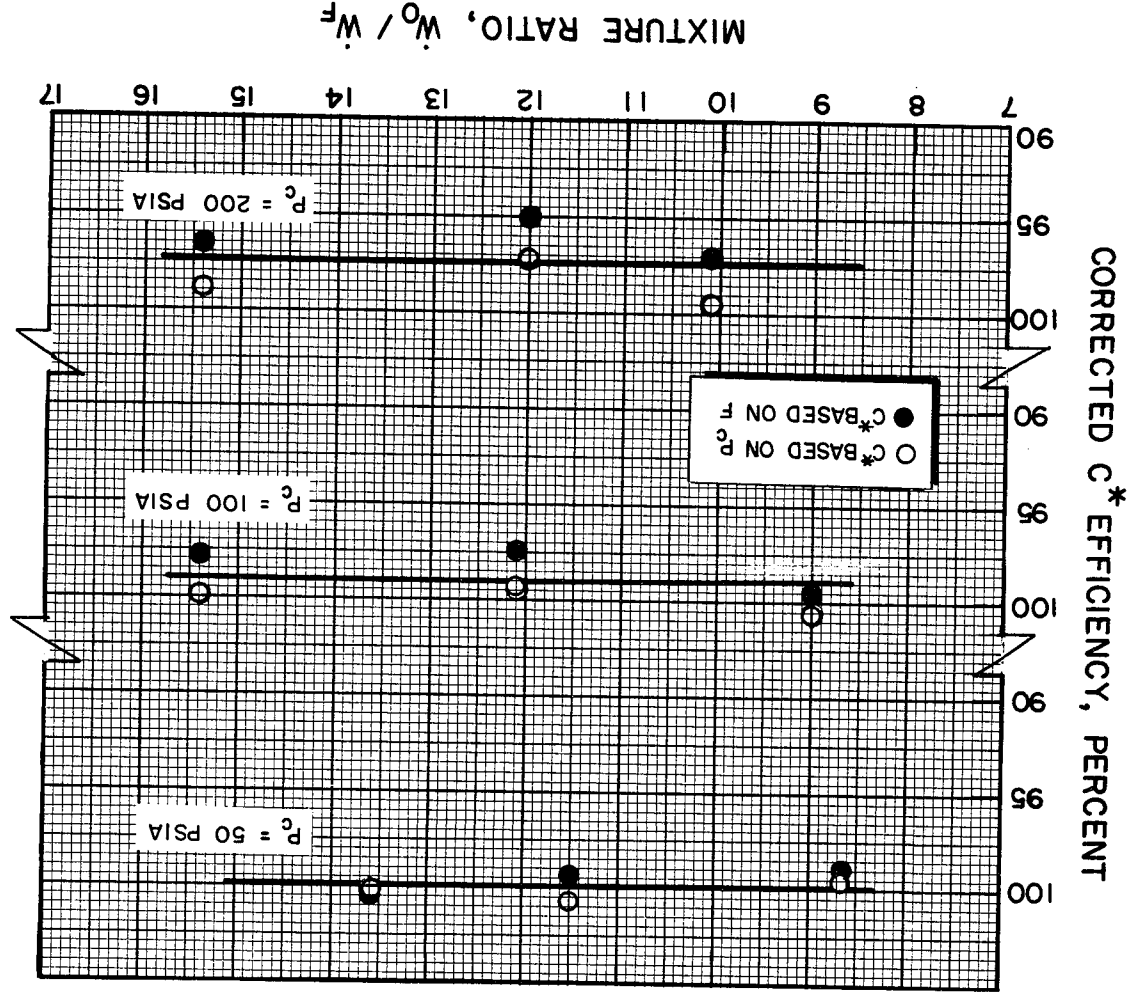
Figure 15. Corrected c* Efficiency, Doublet/Showerhead Injector, at Indicated Nominal Chamber Pressures. L* = 30 inches.

MIXTURE RATIO, $\dot{W}o/\dot{W}f$

CORRECTED C* EFFICIENCY, PERCENT

● c* BASED ON F
○ c* BASED ON Pc

Pc = 200 PSIA

Pc = 100 PSIA

Pc = 50 PSIA
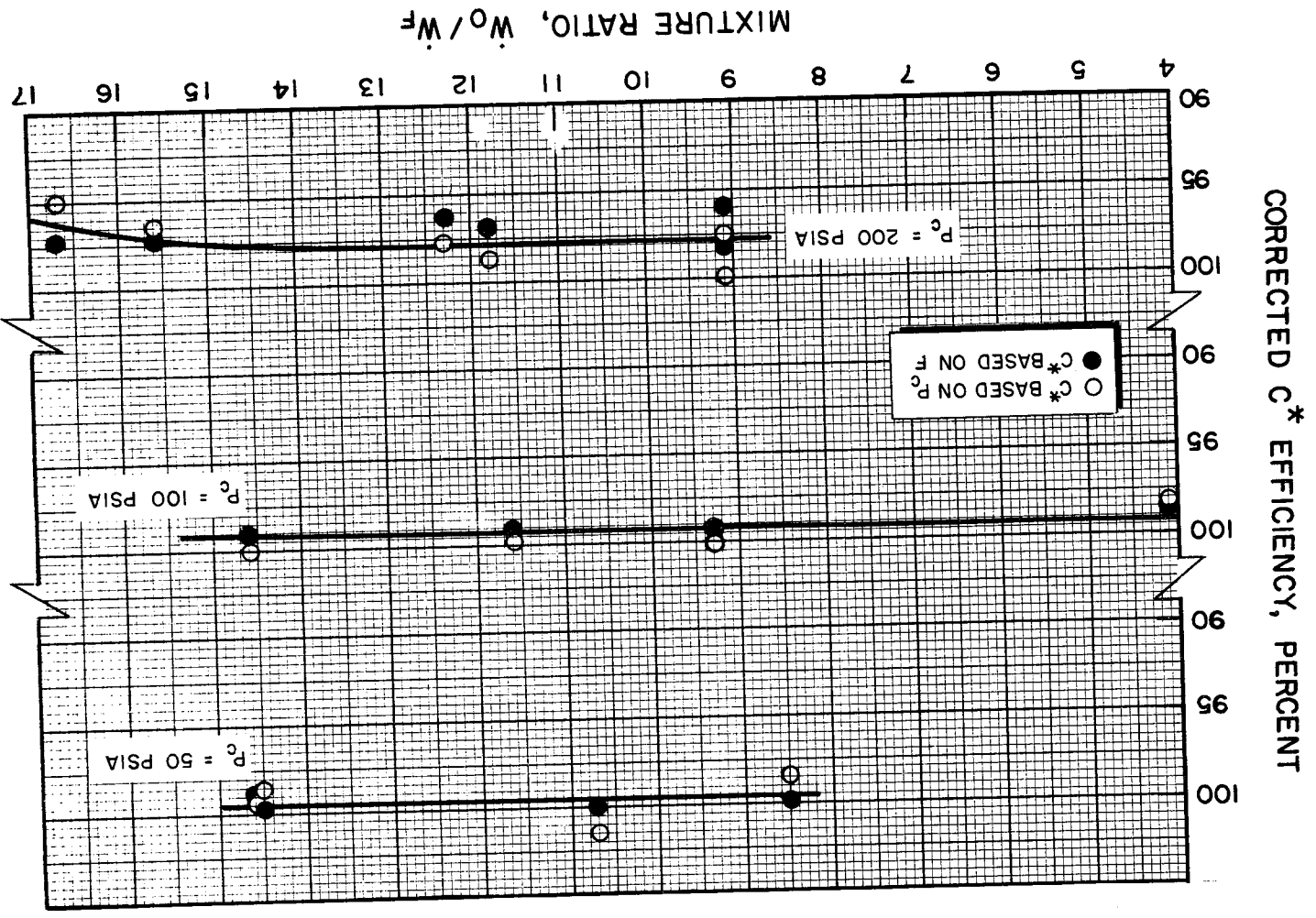
Figure 16. Corrected c* Efficiency, Triplet Injector, at Indicated Nominal Chamber Pressures. L* = 30 inches.

It is apparent from Fig. 15 and 16 that for both injectors, within the mixture ratio range of interest (9 to 15), c* efficiency does not vary with mixture ratio, and varies very slightly with chamber pressure in the 50- to 200-psia range. The indicated values of corrected c* efficiency are summarized in Table 6.

TABLE 6

CORRECTED c* EFFICIENCY, PERCENT

(L* = 30 inches, Mixture Ratio = 9 to 15)

Nominal Chamber Pressure	50	100	200
Injector:			
Triplet	100	99	98
Doublet/Showerhead	100	99	97

There is no significant difference between the injectors as far as c* efficiency is concerned when used in the 30-inch L* chamber, and both injectors fulfill the specific requirement for this portion of the over-all program; i.e., they provide minimum corrected c* efficiency of 97 percent over the specified matrix of chamber pressure (50, 100, 200 psia) and mixture ratio (9, 12, 15).

Effect of Chamber Length on Performance

Twelve experimental firings were carried out at 100-psia nominal chamber pressure in chambers with characteristic lengths of 10 inches and 3.4 inches. Chugging-mode combustion oscillations were observed in seven of these firings, with peak-to-peak amplitudes exceeding 5 percent of the mean value in six, and less than 5 percent in one. A brief discussion of the unstable runs is given in Appendix F.

Because of the difficulty in making reliable measurements of chamber pressure and thrust in the presence of oscillatory combustion of significant amplitude, c^* efficiencies were calculated only for the six low-L^* firings which were stable or in which peak-to-peak oscillation amplitude was less than 5 percent of the mean value. In the absence of a combustion chamber, or when it is very short, combustion takes place in the nozzle, in which case stagnation pressures at the nozzle entrance and throat are not equal. For this reason, c^* efficiencies observed in the low-L^* chambers were based on measurements of thrust. These efficiencies are shown in Fig. 17. Effect of chamber length on combustion efficiency for both injectors at nominal mixture ratio of 15 and 100 psia chamber pressure is shown in Fig. 18.

Differences between triplet and doublet/showerhead injectors, which are obscured in the 30-inch L^* chamber, are evident at the shorter chamber lengths.

Injector Pressure Drops

Nominal and experimental values of oxidizer and fuel side injector pressure drops, as well as corresponding propellant injection velocities, are given in Appendix B.

Hardware Durability

No significant problems were encountered with any of the hardware or with the test facility during the experimental program. Hardware changes observed over the course of the firings consisted only of discoloration of the injector faces and of the interior chamber and nozzle walls; the throat area decreased very slightly (13.80 sq in. to 13.72 sq in.).
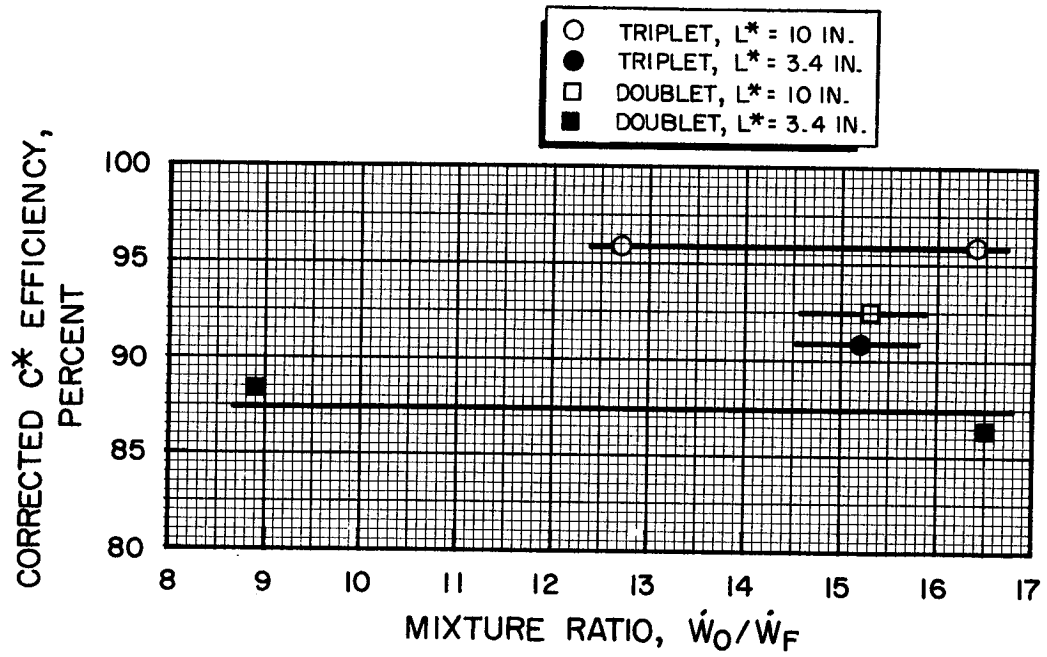
Figure 17. Corrected c* Efficiencies of Triplet and Doublet/
Showerhead Injectors in 3.4-Inch and 10-Inch L*
Chambers at Nominal Chamber Pressure of 100 psia.
(Table 5 contains data shown above.)
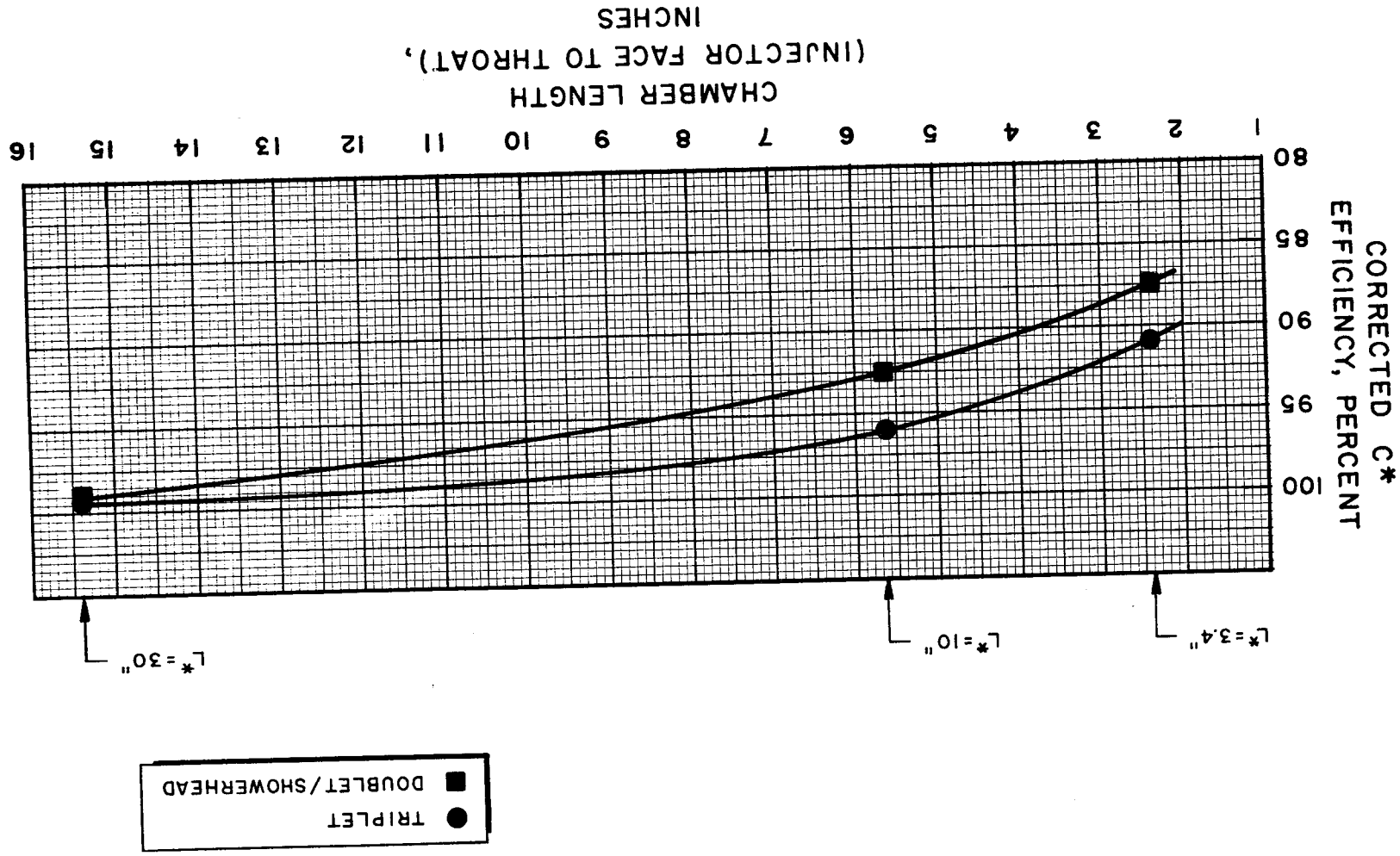
Figure 18. Variation of Corrected c^* Efficiency With Chamber Length at Nominal Chamber Pressure of 100 psia and Mixture Ratio of 1.5.

HEAT TRANSFER

Transient temperature-time data were obtained on the cold sides of the isolated segments (Appendix A) machined into the chamber and nozzle walls. Local values of heat flux and of the corresponding heat transfer coefficients were calculated from these temperature histories. Computational procedures are described in Appendix H.

Most of the heat transfer results are presented in terms of an effective convective heat transfer coefficient, h_g; this allows more general utility of the data than does heat flux, because h_g is less sensitive to actual thrust chamber wall temperature and to adiabatic wall temperature.

Circumferential Variation

Typical circumferential variations of the heat transfer coefficient for the doublet/showerhead and triplet injectors are shown in Fig. 19 and 20, respectively. Locations of start of nozzle convergence, geometric throat, and sonic throat (calculated by method of Sauer, Ref. 15) are indicated in these and in subsequent data plots. The curves are drawn as dotted lines near the start of convergence and in the region of the throat to indicate extrapolations of experimental measurements. Average observed circumferential variation in h_g values was approximately ±6 percent; maximum variation (near the nozzle exit) was ±12 percent.

Circumferential values were randomly distributed at the various axial locations, i.e., none of the rows gave consistently higher or lower values than the others. The mean of the four circumferential measurements at each axial location was therefore taken as the value at that location.
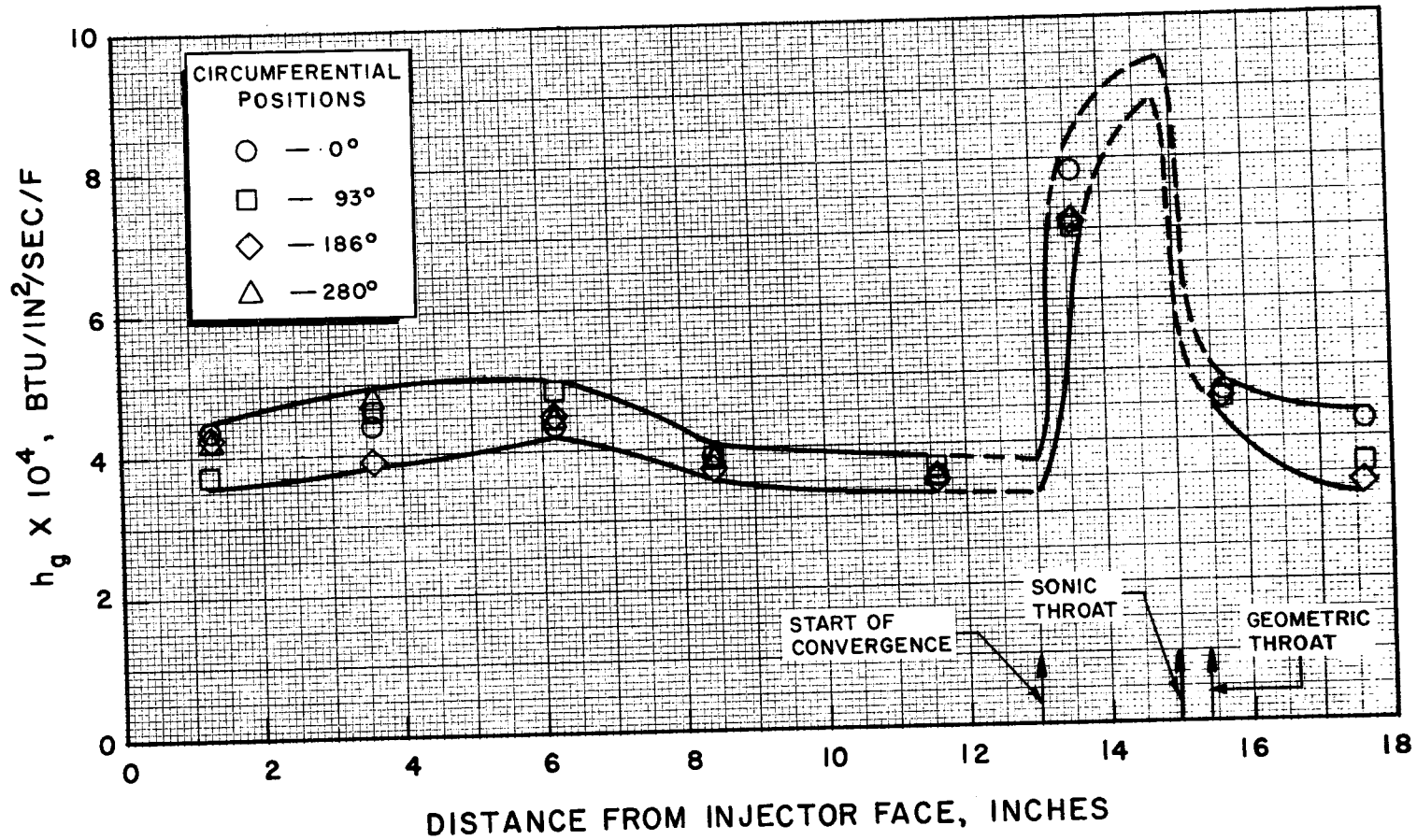
Figure 19. Typical Circumferential Variations of Heat Transfer Coefficient, Doublet/Showerhead Injector, P_c = 100 psia, M.R. = 12, Run No. 169. Band Width Shows Maximum Circumferential Variation. Dashed Lines Indicate Extrapolations from Measured Values.
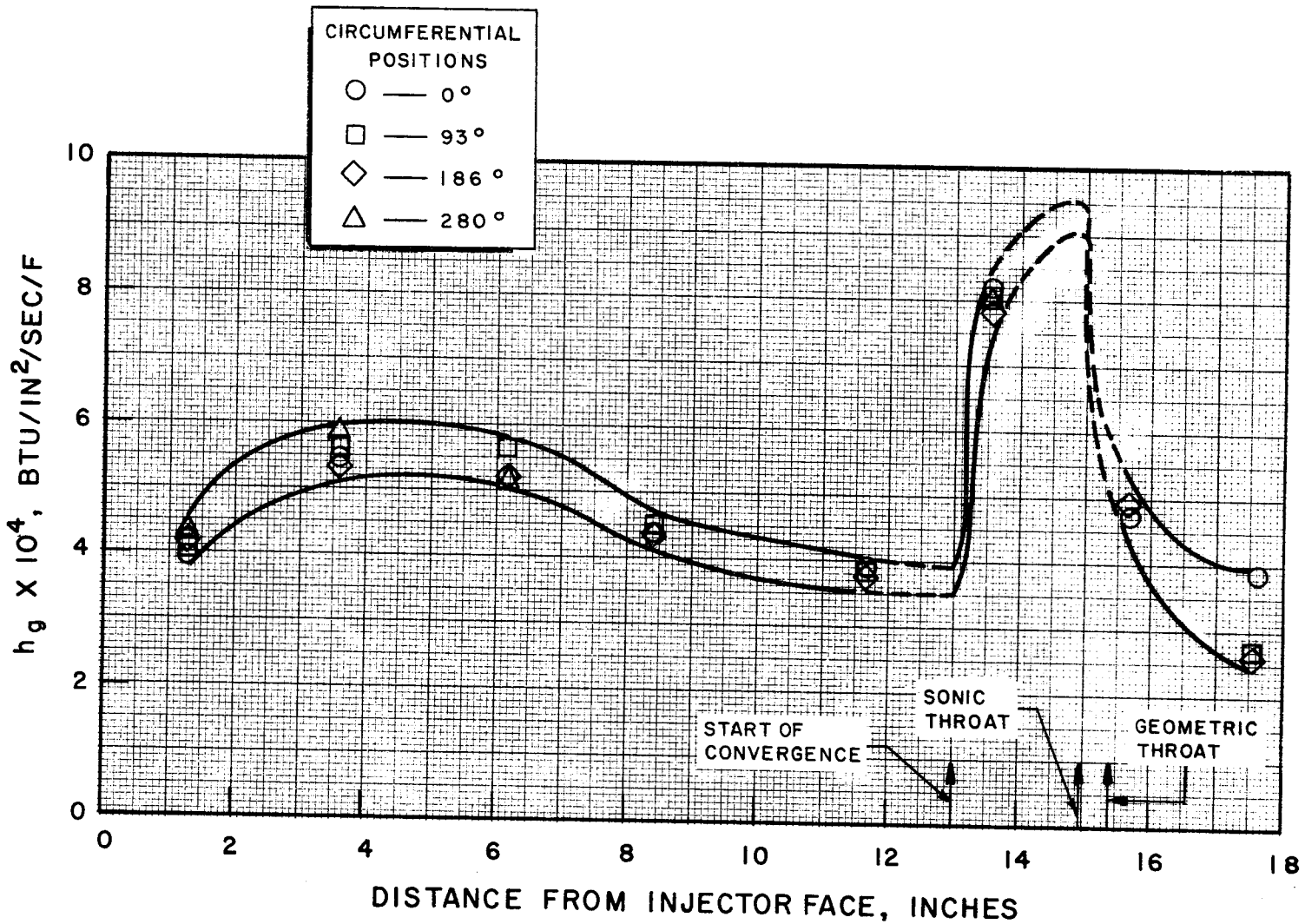
Figure 20. Typical Circumferential Variation of Heat Transfer Coefficient, Triplet Injector, P_c = 100 psia, M.R. = 12, Run No. 177. Band Width Shows Maximum Circumferential Variation. Dashed Lines Indicate Extrapolations from Measured Values.

Axial Variation

Experimental values of the heat transfer coefficient are plotted again
axial location in Fig. 21 and 22 for the doublet/showerhead and triple
injectors, respectively, at 50-, 100-, and 200-psia nominal chamber pr
sure in the 30-inch L* chamber. Data points are shown as the actual
half-inch lengths covered by the isolation segments. Corresponding a:
variations of local heat flux are shown in Fig. 23 and 24 for the doul
showerhead and triplet injectors, respectively.

The values of h_g are approximately the same for both injector pattern
at each chamber pressure. Peak values occur at the axial position
slightly upstream of the geometric throat. In the combustion chamber
the highest heat transfer coefficients occur within a short distance
the injector face. For both injectors at 200-psia chamber pressure,
values of the heat transfer coefficients near the injector approach t
at the nozzle throat.

Indicated values of h_g at the intersection of the sonic plane with tl
nozzle wall (0.45 inches upstream of the geometric throat) are summa:
in Table 7. Because these values were obtained by extrapolation fro
upstream and downstream sides, they are subject to significant uncer
and should be used to indicate relative orders of magnitude, rather
absolute values.

Effect of Mixture Ratio

Experimental heat transfer coefficients at the following three axia.
tions in the 30-inch L* chamber (see Fig. 9) are shown in Fig. 25, !
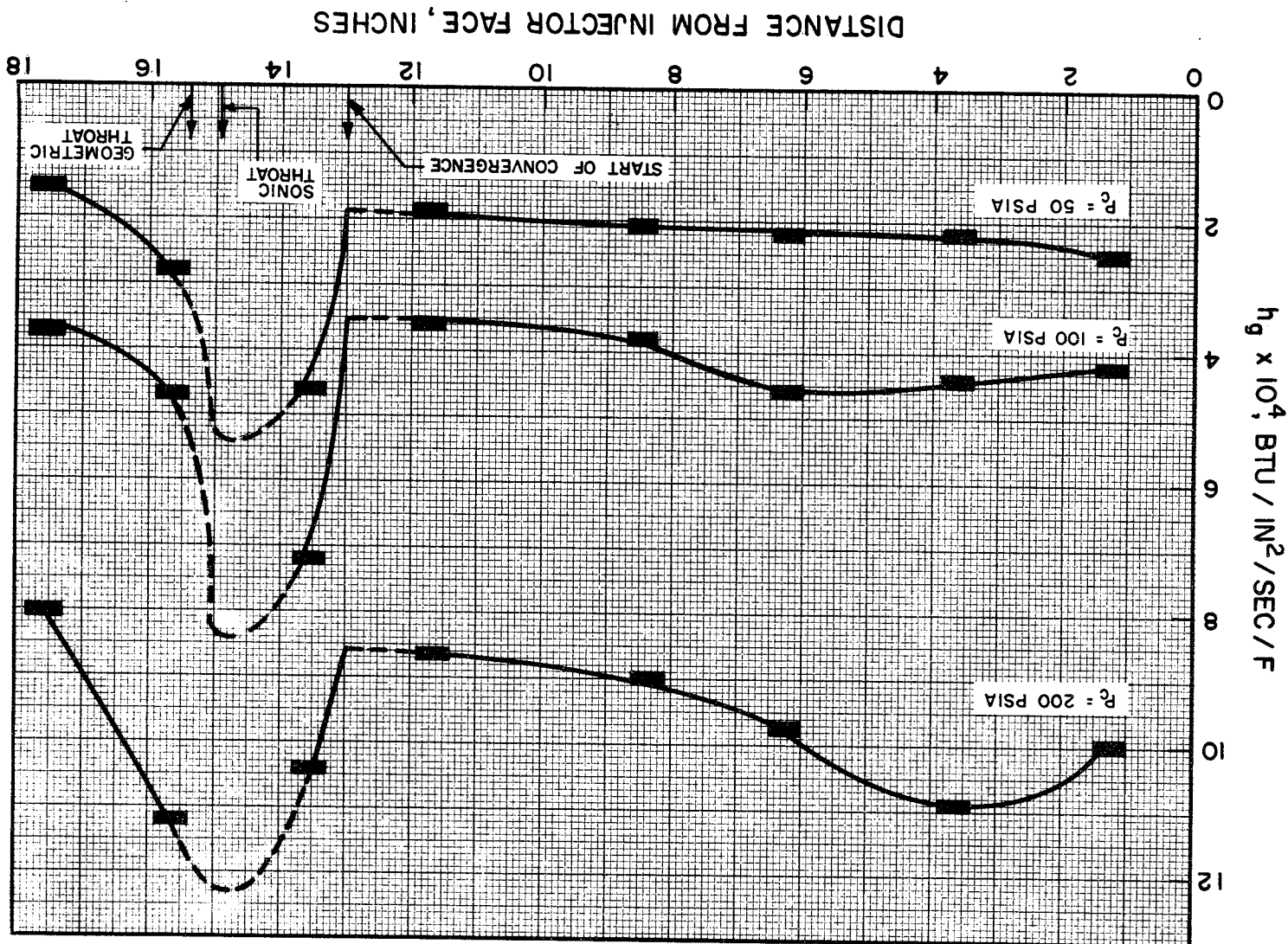
Figure 21. Axial Variation of Heat Transfer Coefficient, Doublet/Showerhead Injector at Indicated Nominal Chamber Pressures and Mixture Ratio of 12. Dashed Lines Indicate Extrapolations from Measured Values.
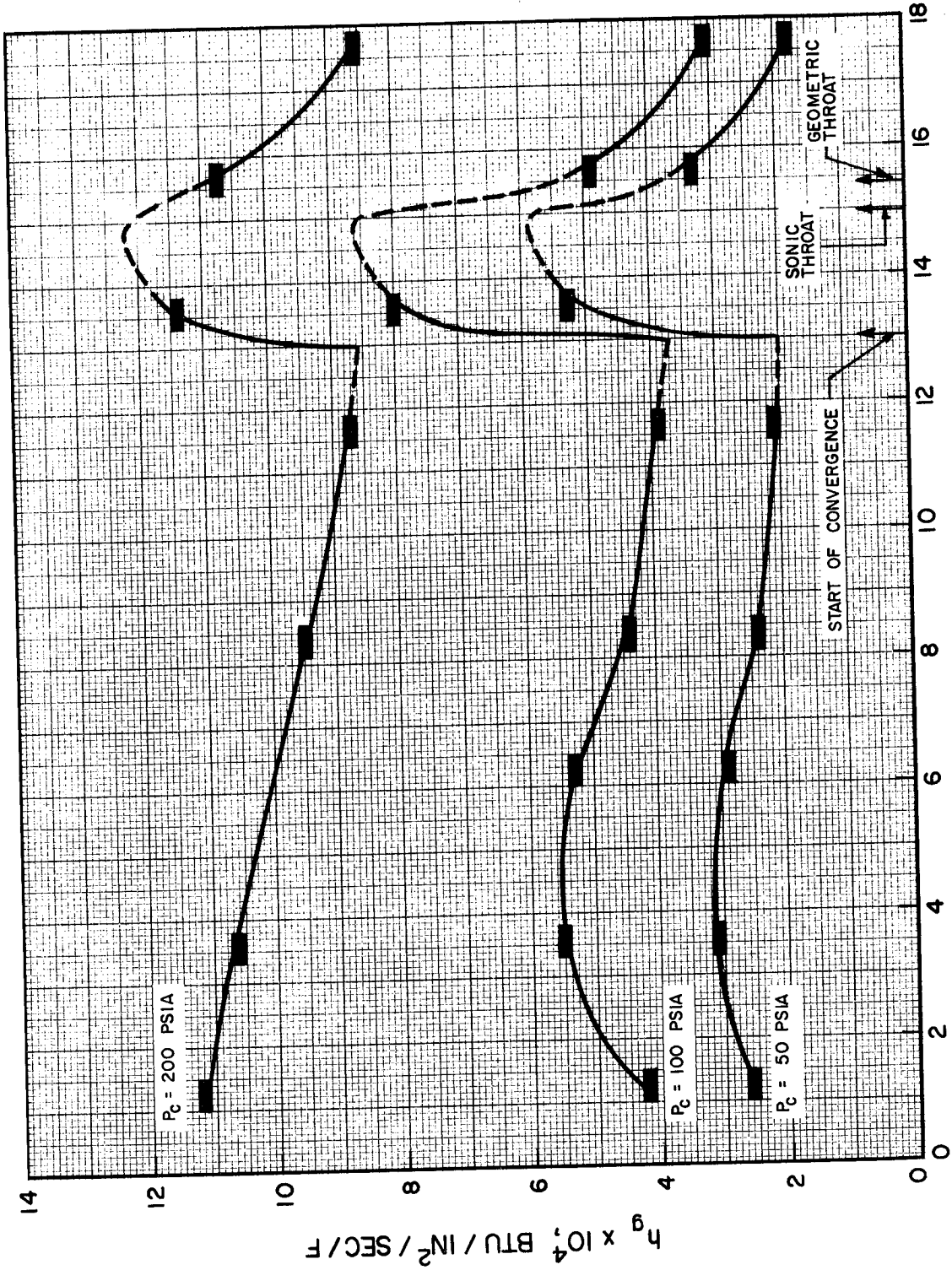
DISTANCE FROM INJECTOR FACE, INCHES

Figure 22. Axial Variation of Heat Transfer Coefficient, Triplet Injector at Indicated Nominal Chamber Pressures and Mixture Ratio of 12. Dashed Lines Indicate Extrapolations from Measured Values.
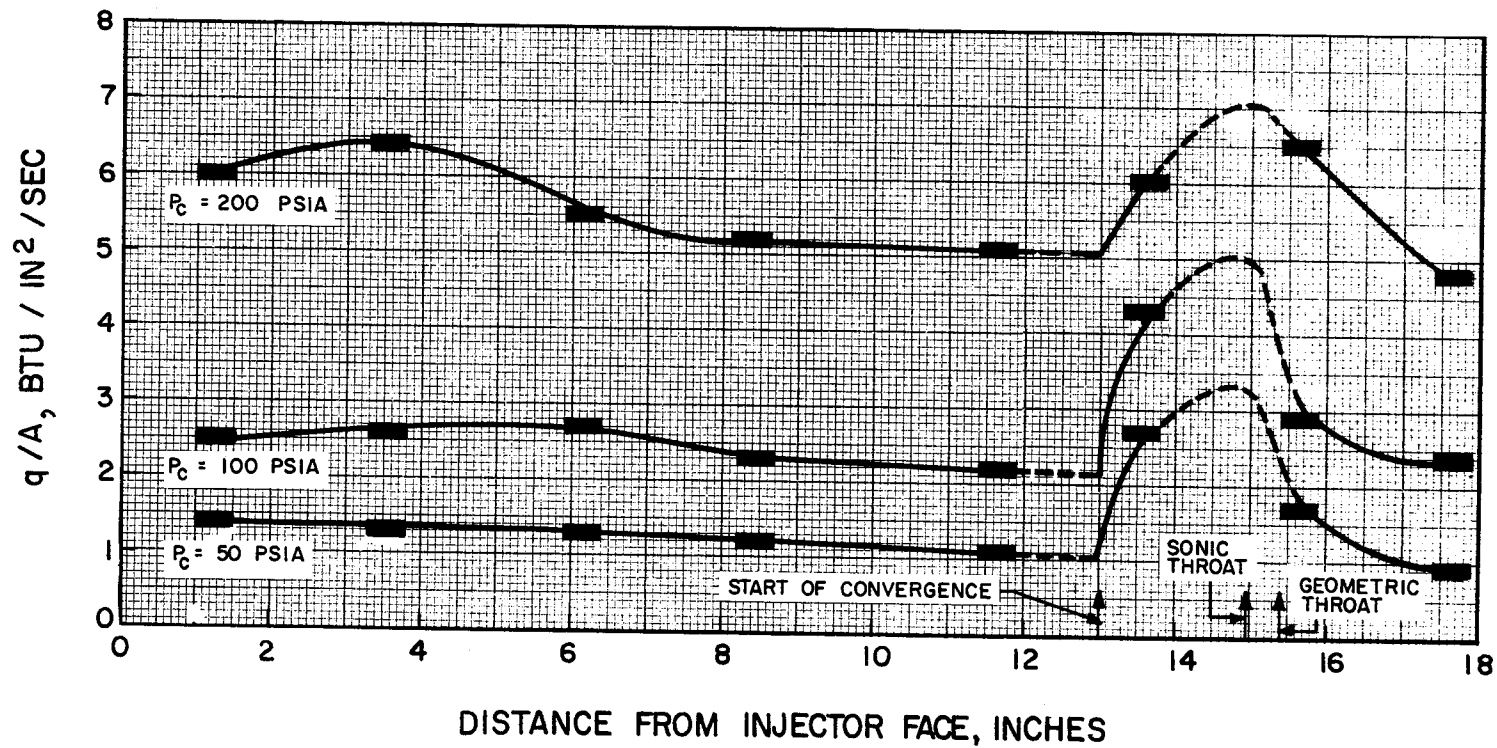
Figure 23. Axial Variation of Heat Flux, Doublet/Showerhead Injector at Indicated Nominal Chamber Pressures and Mixture Ratio of 12. Dashed Lines Indicate Extrapolations from Measured Values.

Figure 24. Axial Variation of Heat Flux, Triplet Injector at Indicated Nominal Chamber Pressures and Mixture Ratio of 12. Dashed Lines Indicate Extrapolations from Measured Values.

TABLE 7

ESTIMATED HEAT TRANSFER COEFFICIENTS AT

SONIC POINT IN NOZZLE THROAT

$(h_g$ in $Btu/in.^2/sec/F)$

$(L* = 30$ inches$)$

Injector Type	Nominal Mixture Ratio	Nominal Chamber Pressure, psia		
		50	100	200
Triplet	9	6.0×10^{-4}	8.8×10^{-4}	12.6×10^{-4}
	12	5.9	8.6	12.2
	15	5.8	8.5	11.9
Doublet/ Showerhead	9	5.3×10^{-4}	8.6×10^{-4}	12.7×10^{-4}
	12	5.3	8.4	12.4
	15	5.3	8.2	12.1

27 as functions of mixture ratio at each of the nominal chamber pressures employed:

1. Immediately upstream of the start of nozzle convergence, axial position 5

2. In convergent section of nozzle, upstream of the throat, axial position 6

3. Immediately downstream of geometric throat, axial position 7

In the mixture ratio range 9 to 15, h_g in the nozzle decreases slightly with increasing mixture ratio. This effect is most pronounced at 200-psia chamber pressure and least at 50 psia, at which level the variation is negligibly small.
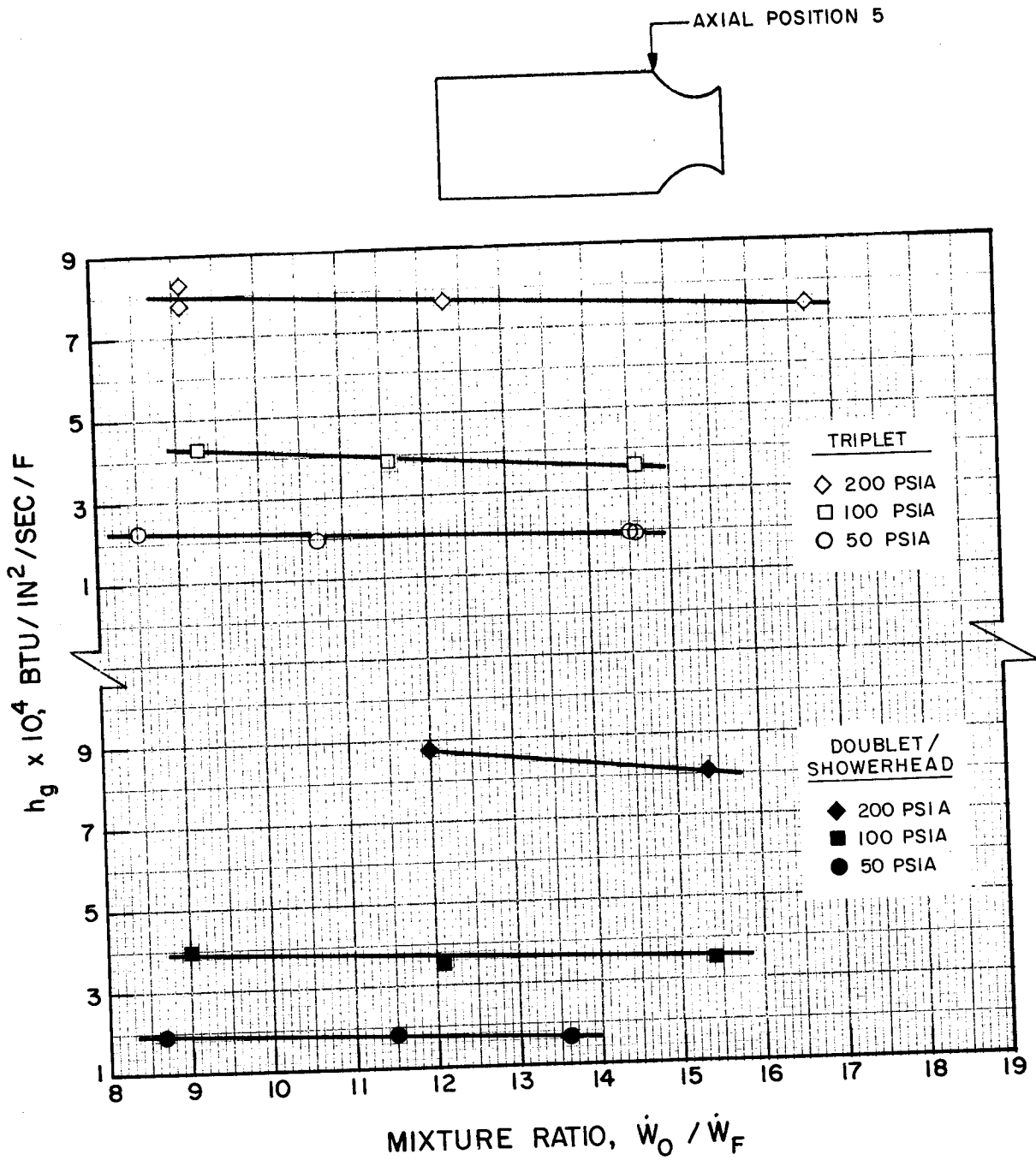
Figure 25. Heat Transfer Coefficient as Function of Mixture Ratio at Axial Position 5 (11.7 Inches from Injector Face) for the Triplet and Doublet/Showerhead Injectors at Indicated Nominal Chamber Pressures.
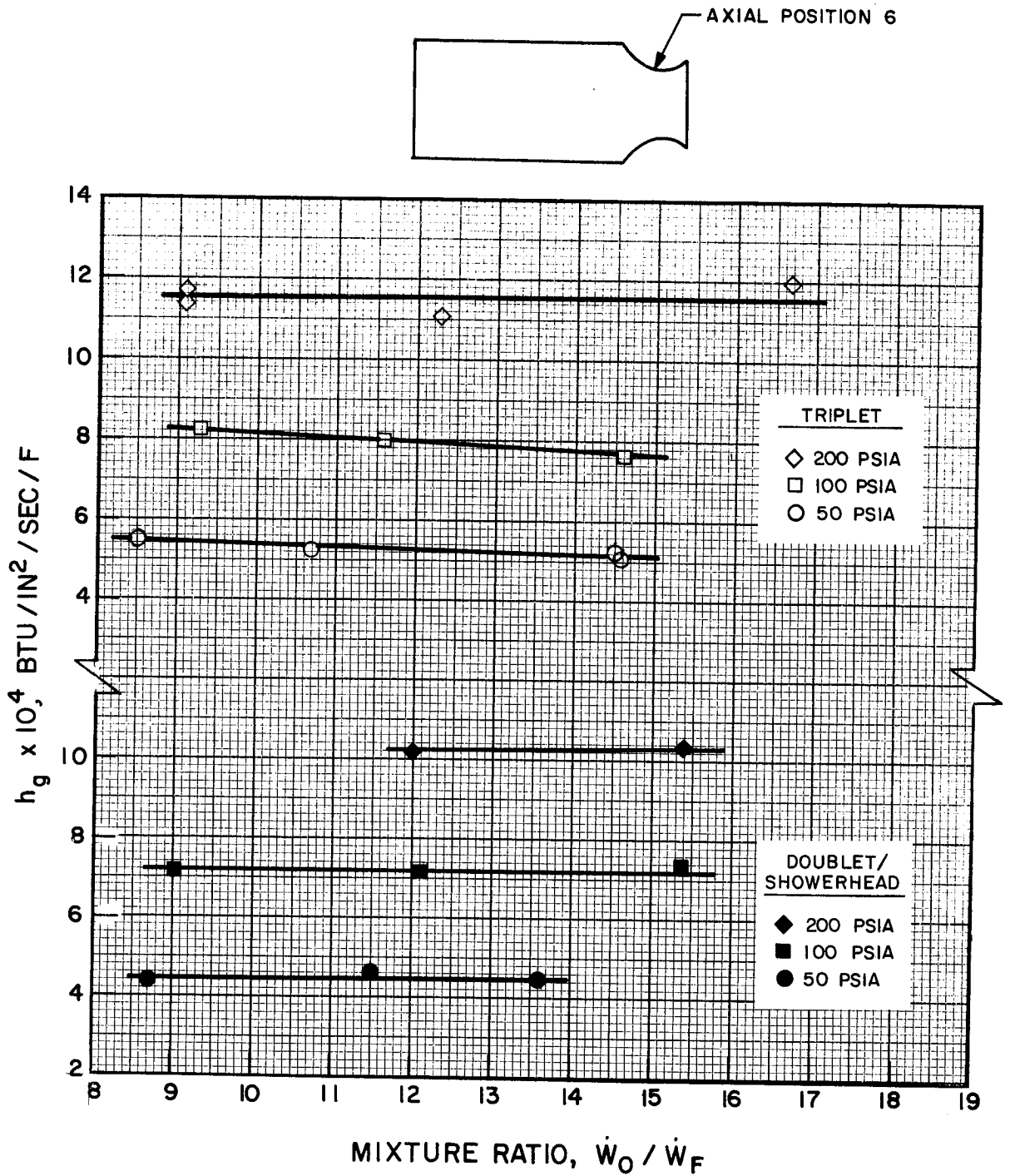
Figure 26. Heat Transfer Coefficient as Function of Mixture Ratio at Axial Position 6 (1.8 Inches Upstream of Throat) for the Triplet and Doublet/Showerhead Injectors at Indicated Nominal Chamber Pressures.
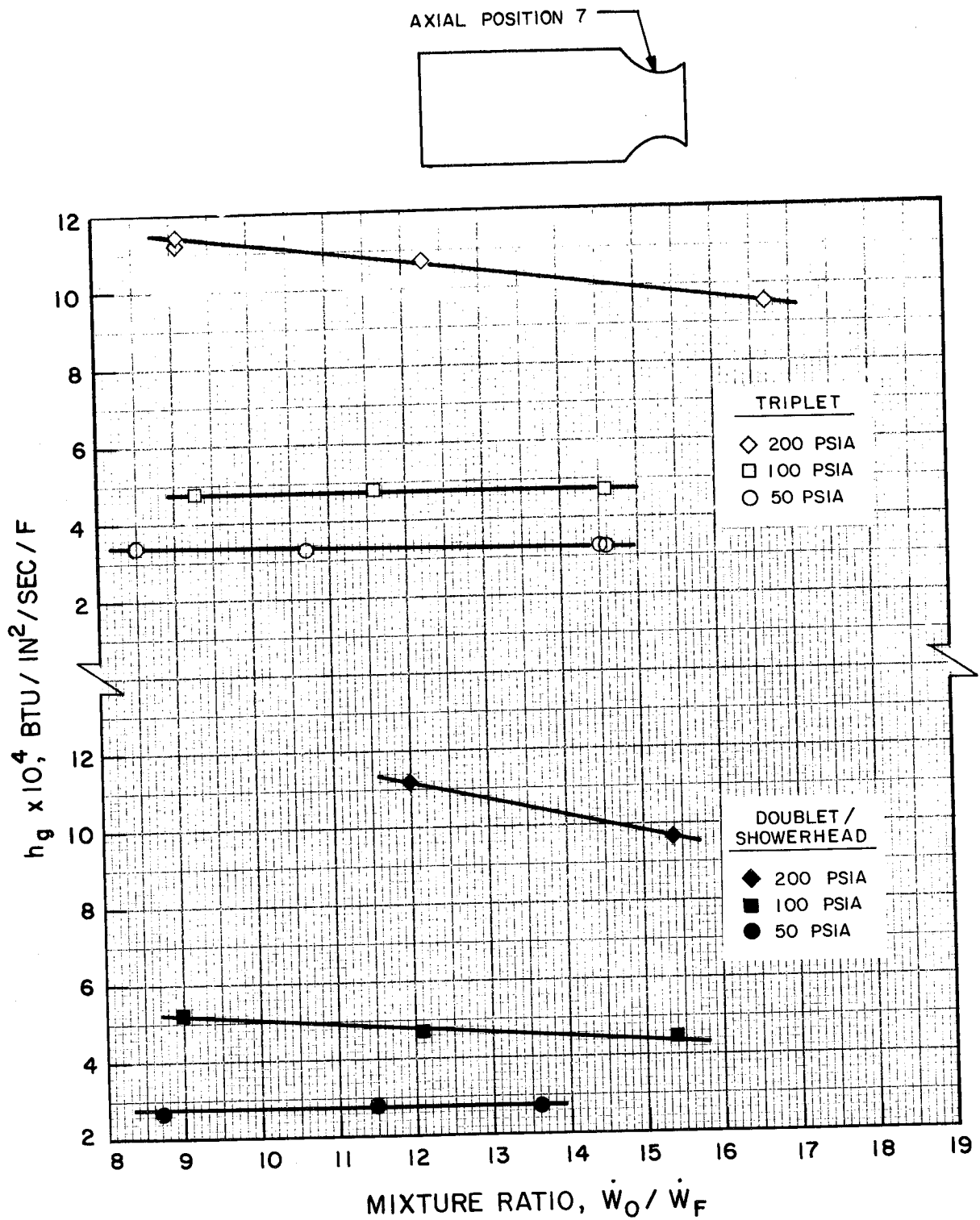
Figure 27. Heat Transfer Coefficient as Function of Mixture Ratio at Axial Position 7 (0.3 Inches Downstream of Throat) for the Triplet and Doublet/Showerhead Injectors at Indicated Nominal Chamber Pressures.

Effect of Chamber Length

Some of the firings carried out in shortened chambers, at L* values of
3.4 and 10 inches, exhibited low-frequency combustion oscillations (Appen-
dix F). Those at nominal mixture ratio of 15, however, were either stable
(three out of four) or showed very low amplitude oscillations. Heat
transfer coefficients obtained in these firings, all at nominal chamber
pressure of 100 psia, are shown in Fig. 28.

At a chamber L* of 3.4 inches (injector face located at the start of
nozzle convergence), the maximum experimental values of h_g for both in-
jectors occur at the station just downstream of the geometric throat,
whereas at a chamber L* of 10 inches, as at 30 inches (Fig. 21 and 22),
the highest experimental values occur at the station in the nozzle con-
vergent section. The levels of the convective heat transfer coefficient
were approximately the same with chamber characteristic lengths of 10
and 30 inches. However, the convective heat transfer coefficients in
the 3.4-inch L* chamber at the axial station just downstream of the geo-
metric throat increased by a factor of approximately two over the values
in the 10 and 30 inch L* chambers.

The presence of even a very short combustion chamber at 10-inch L* per-
mits most of the combustion and boundary layer development to take place
upstream of the nozzle. Hence heat flux within the nozzle is quite
similar to that observed with the 30-inch L* chamber. When combustion
occurs in the nozzle, however, as in the 3.4-inch L* chamber, the heat
transfer processes are completely altered, and the indicated heat trans-
fer coefficients represent a complex interaction of the effects of com-
bustion heat release, thin boundary layers, and nozzle flow.
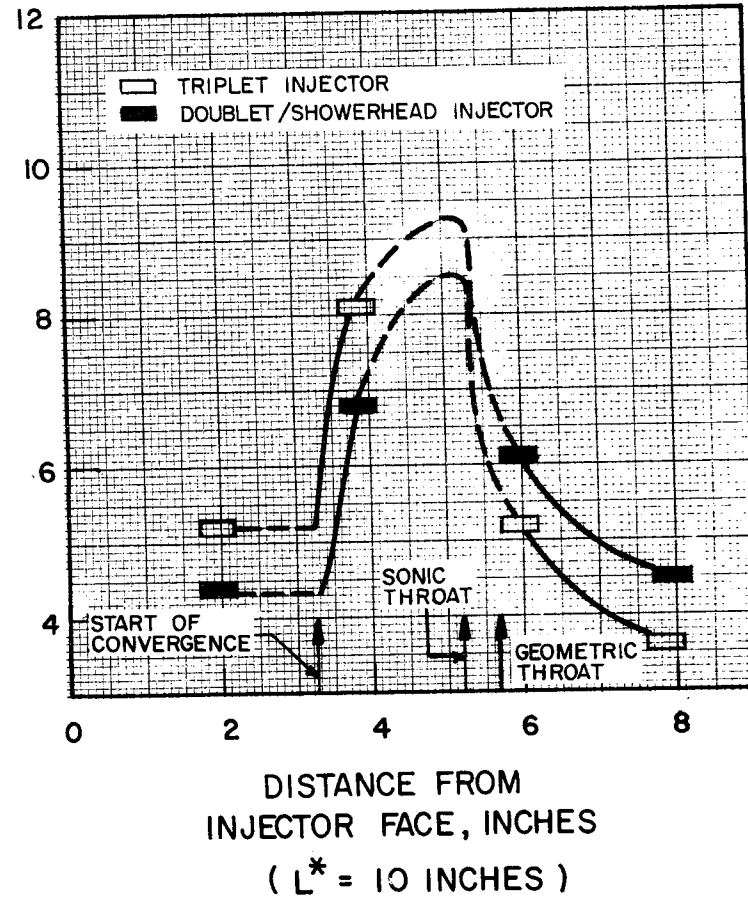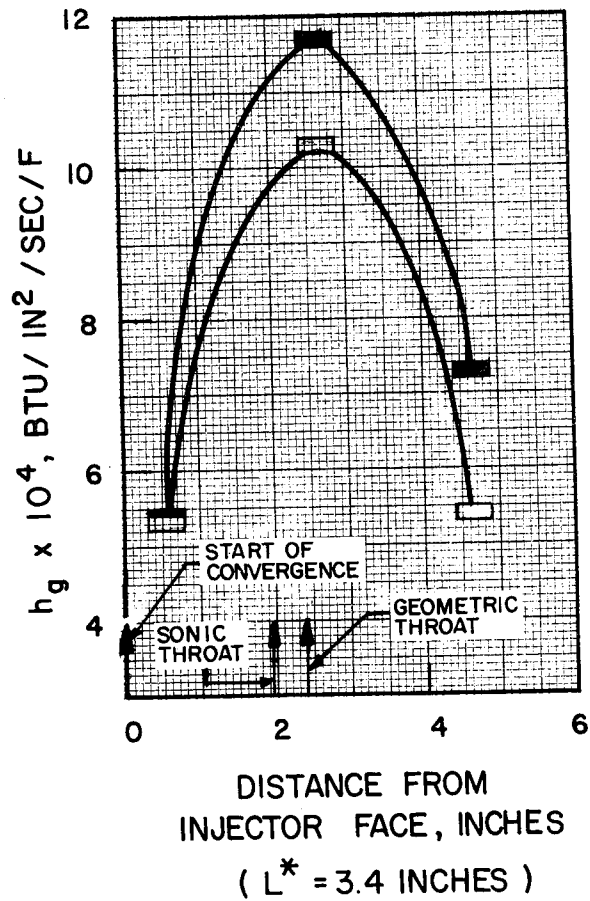
Figure 28. Heat Transfer Coefficients of Triplet and Doublet/Showerhead Injectors in 3.4-inch and 10-inch L* Chambers. Nominal P_c = 100 psia, M.R. = 15.

DISCUSSION OF RESULTS

PERFORMANCE

Performance obtained with the LF_2/GH_2 propellant combination is mainly dependent upon the fluorine vaporization rate which is, in turn, a function of the degree of fluorine atomization, because the vapor phase fluorine-hydrogen reaction may be considered essentially instantaneous and propellant distribution is maximized by rapid diffusion of gaseous hydrogen. Consequently, the primary purpose of LF_2/GH_2 injectors is to establish a degree of fluorine atomization such that the droplets produced are small enough to vaporize completely within the available chamber length. Insofar as degree of fluorine atomization is insufficient to produce complete vaporization, combustion is incomplete and performance is degraded. A theoretical relationship between LF_2/GH_2 performance and percent of fluorine vaporized, based on Priem's calculations (Ref. 6), is nearly linear, as shown in Fig. 29.

The difference in the degrees of atomization produced by the doublet/ showerhead and triplet injectors is obscured in the 15.4-inch chamber $(L^* = 30$ inches$)$, in which both designs produce essentially complete combustion. Residence time in this chamber is long enough for complete vaporization of even the larger fluorine droplets, so that attainment of maximum degrees of atomization is not needed. Performance in the shorter chambers, in which the difference between the injectors is brought out, is evidence of the better atomization produced by the triplet. Neverthe- less, the comparatively high c* efficiency of the doublet/showerhead injector in the short chambers shows that this pattern also gives good atomization.
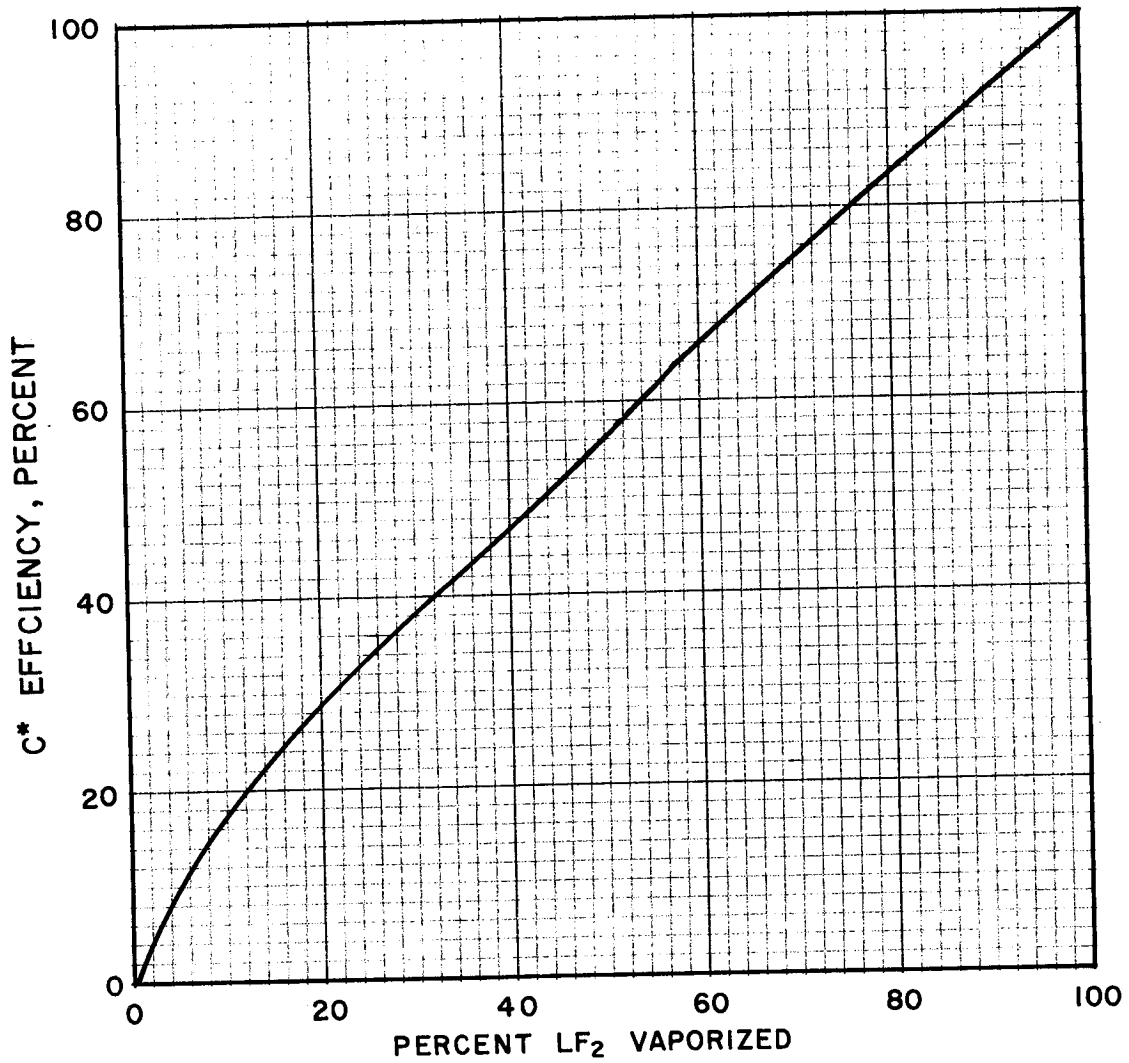
Figure 29. Theoretically Derived Variation of c^* Efficiency with Percent of Liquid Fluorine Vaporized in LF_2/GH_2 Combustion. P_c = 300 psia. Data from Ref. 6.

In both injectors, degree of fluorine atomization is dependent upon the action of the gaseous hydrogen. The dominant effect that gas velocity can have on the degree of atomization resulting from the impingement of two liquid streams is brought out by Ingebo's relationship (Eq. 1); for example, with liquid orifice diameter of 0.039 inches and velocity of 70 ft/sec, a gas-to-liquid velocity difference of only 250 ft/sec can decrease the volume-mean-number diameter of the droplets about 70 percent from the value obtained with zero velocity difference (230 microns to 70 microns). Applicability of Eq. 1, derived from experimental data obtained from heptane jets impinging in an ambient air stream, to fluorine jets in a 100-psia combustor may be determined by means of the following relationship, which establishes the effect of liquid and gas properties on volume-mean-number drop size (Ref. 16).

$$D_{30} \propto \left(\frac{\sigma\mu}{\rho}\right)^{1/4} \left(\frac{1}{\rho_g}\right)^{1/4} \tag{4}$$

where

σ = liquid surface tension

μ = liquid viscosity

ρ = liquid density

ρ_g = gas density

The fluorine/heptane D_{30} ratio, from Eq. 4, is very nearly unity, so fluorine droplet sizes are essentially the same as heptane droplet sizes, under the above-mentioned conditions.

The triplet and doublet/showerhead injector patterns are characterized by different mechanisms of gas-augmented liquid atomization. Under the design conditions selected, the high injection momentum of the gaseous hydrogen is used to break up and atomize the fluorine jets in the triplet injector, whereas, in the doublet/showerhead, initial atomization results from momentum interchange of the two impinging jets, with secondary atomization by the hydrogen downstream of the impingement point.

The nature of the atomization processes in both the triplet and doublet/showerhead injectors is shown in a series of microflash and schlieren photographs of sprays from single-element injectors of both patterns, with water and helium as fluorine and hydrogen simulants. Details of the simulated injector parameters and photographic procedures are given in Appendix G.

The photographs are reproduced in Fig. 30 (microflash) and Fig. 31 (schlieren). Figures 30 (a) and (b) show water flow only and indicate that a fairly coarse spray is produced by liquid impingement alone under the given flow conditions. When gas flow is added in the doublet/showerhead element, Fig. 30 (c) and (d), the sides of the fan are cleanly cut and atomized. The degree of atomization in the central portion of the spray is also substantially improved by the gas momentum. In the triplet element, Fig. 30 (e) and (f), the fine degree of atomization is evident. Figure 30 (e) shows that the liquid streams do not impinge upon each other, but are spread by the gas jet, which does all of the atomizing. These and related company-funded studies (Ref. 8) show that, for the triplet design used, atomization under firing conditions employed in this program is due entirely to the action of the gaseous hydrogen.

Schlieren photographs of the doublet/showerhead element flowing helium alone, Fig. 31 (a) and (b), show the intersection of the gas jets within

EDGE
VIEWS $\longrightarrow$
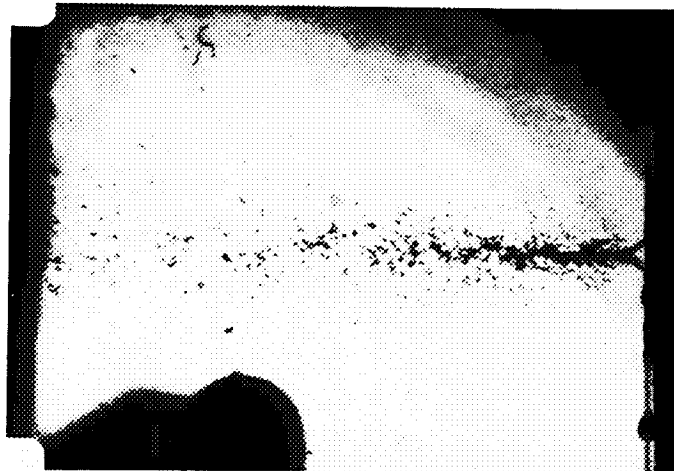
(a)
3"

FAN
VIEWS $\longrightarrow$

(b)
WATER ONLY

EDGE V

SHOWERHEAD
GAS ORIFICES —

73-1

(c)
3"

(e)
3"

(d)
WATER AND HELIUM,
JBLET/SHOWERHEAD PATTERN
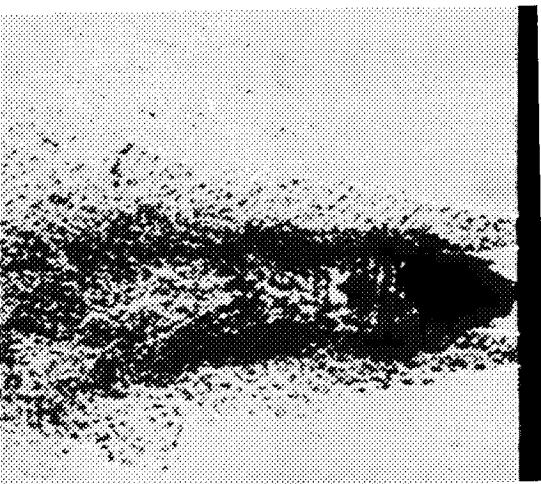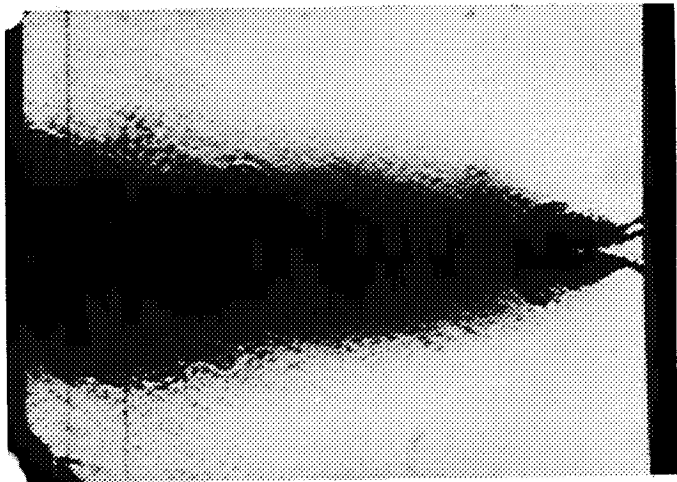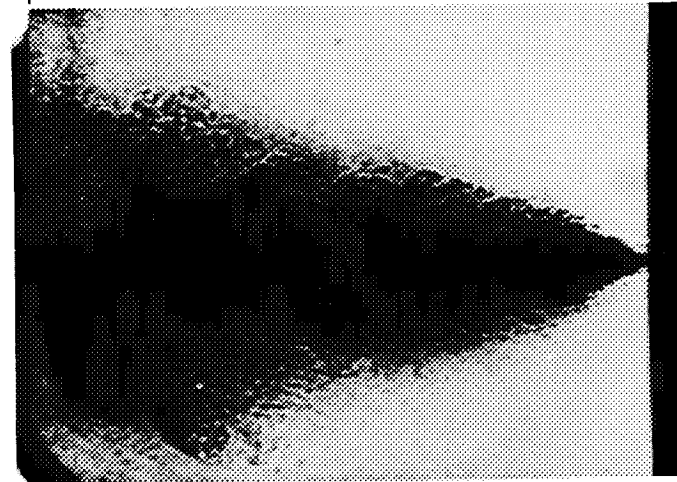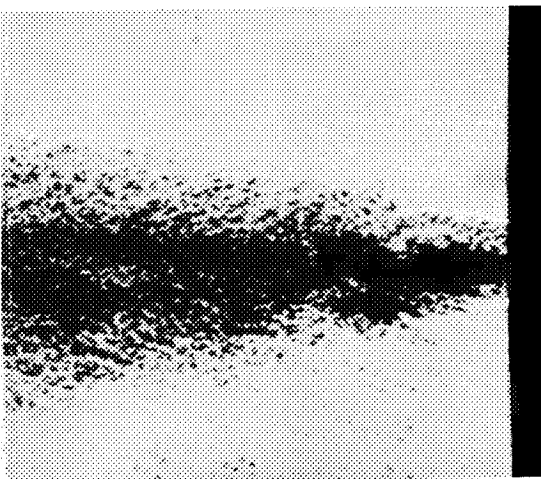
(f)
WATER AND HELIUM
TRIPLET PATTERN

FAN VIEW

SELF-IMPINGING
LIQUID ORIFICE

₵ SPRAY FAN

_ET / SHOWERHEAD PATTERN

FAN VIEW

EDGE VIEW

SHOWERHEAD
GAS ORIFICE

₵ SPRAY FAN

TRIPLET PATTERN

Figure 31. Schlieren Photographs--Cold Flows
of Single-Element Injectors With Water and
Helium. Simulation Condition:
$(\text{Momentum Ratio})_{\text{Hot Firing}} =$

$(\text{Momentum Ratio})_{\text{Cold Flow}}$

(c)
3"

(e)
3"
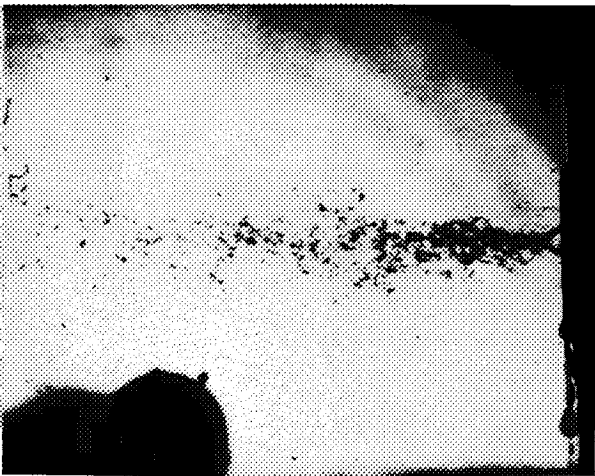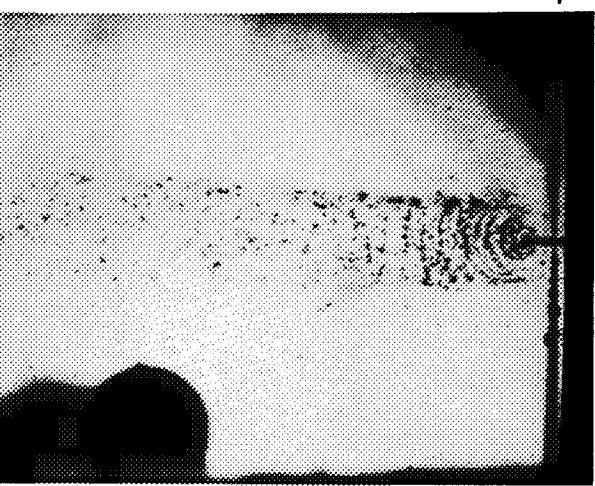
(d)
WATER AND HELIUM,
DOUBLET / SHOWERHEAD PATTERN

(f)
WATER AND HELIUM
TRIPLET PATTERN
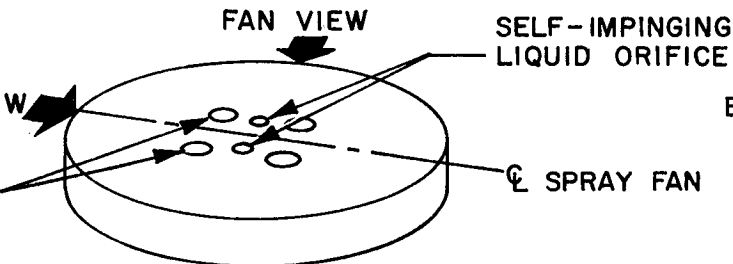
DOUBLET / SHOWERHEAD PATTERN
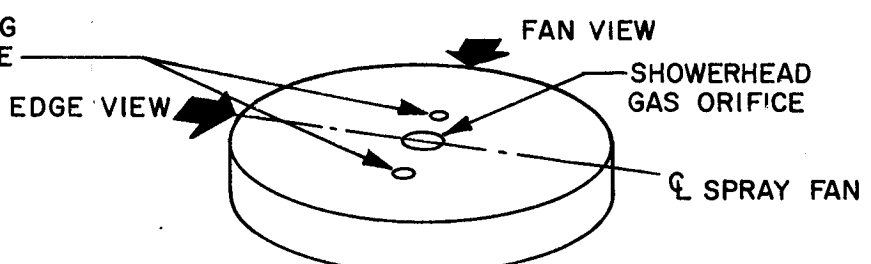
TRIPLET PATTERN

Figure 30. Microflash Photographs--Cold Flows
of Single-Element Injectors With Water and Heliu
Simulation Condition: $\frac{(\text{Momentum Ratio})_{\text{Hot Firing}}}{(\text{Momentum Ratio})_{\text{Cold Flow}}}$

EDGE
VIEWS →

FAN
VIEWS →

(a)
3"
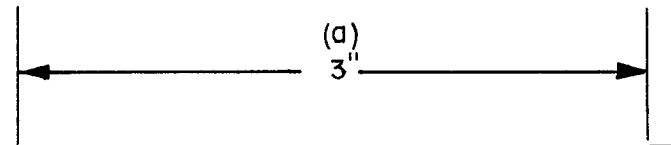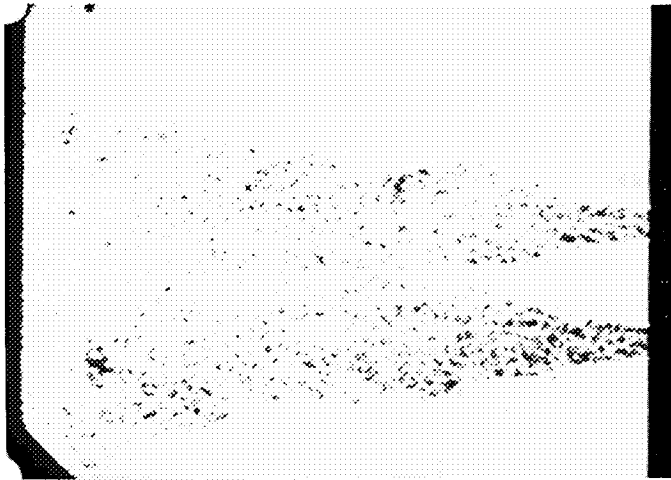
(b)
HELIUM ONLY

EDGE VIEW

SHOWERHEAD
GAS ORIFICES

DO

74-1

a very short distance from the injector face. With the addition of water, Fig. 31 (c) and (d), the thorough mixing of gas and liquid and the effective atomization of the latter is evident. The mist-like spray obtained with the triplet injector flowing both helium and water is shown in Fig. 31 (e) and (f). Imaginary superposition of corresponding photographs taken under the same flow conditions, Fig. 30 (c) and (d) with Fig. 31 (c) and (d), and Fig. 30 (e) and (f) with Fig. 31 (e) and (f), permits visualization of the actual atomization processes occurring.

The reason for the comparatively high performance of the doublet/showerhead injector is indicated by the degree of atomization which it produces. In this pattern, the gaseous hydrogen jets affect the liquid atomization by intersection with the spray fans. The gas jet structure is characterized by a potential core, in which velocity is essentially equal to injection velocity, and a downstream region whose axial velocity decreases with distance from the orifice (Ref. 10). Axial variations of gas jet velocity with distance from orifice at various ambient stream velocities, based on experimental data as well as theoretical calculations, are shown in Fig. 32 (Ref. 10), which may be used to estimate gas velocity at points of intersection with the liquid spray fans. Thus, at zero ambient velocity (most conservative case), with 0.089-inch gas orifice diameter (GH_2 orifice size), and at a point 1 inch downstream of the injector, the axial GH_2 velocity is about one-half the injected gas velocity.

The lowest hydrogen injection velocity, obtained at the highest mixture ratio, is approximately 2400 ft/sec (Mach Number 0.56; see Appendix B). Hence, at a distance of 1 inch from the doublet/showerhead injector face, the GH_2 axial velocity is about 1200 ft/sec. Nonaxial velocities at this point may be estimated from Fig. 33 (Ref. 10) which gives velocity distributions as a function of distance from injection plane and jet radius.
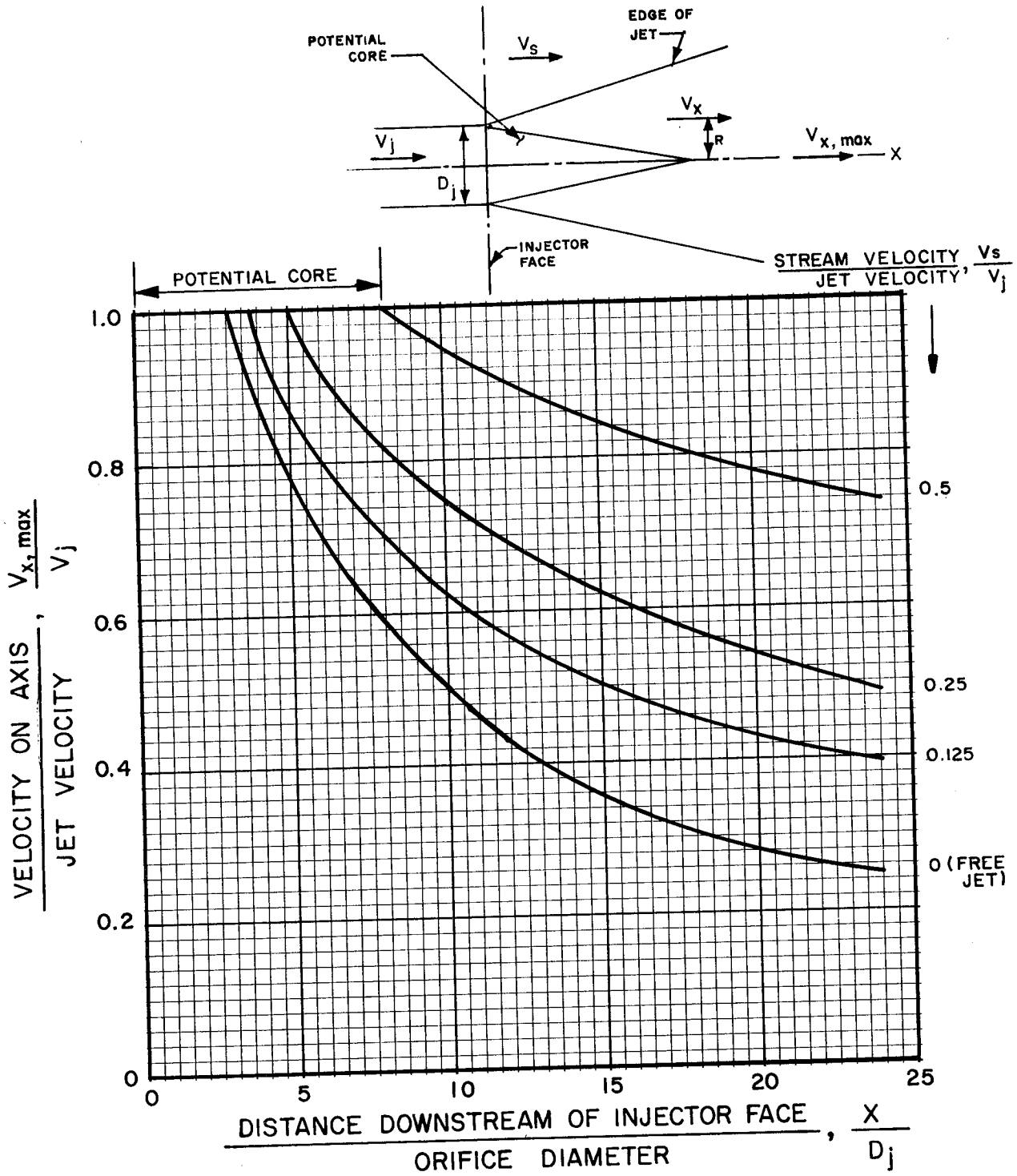
Figure 32. Theoretically Derived Distribution of Velocity Along Axis of Circular Gas Jet. Data from Ref. 10.
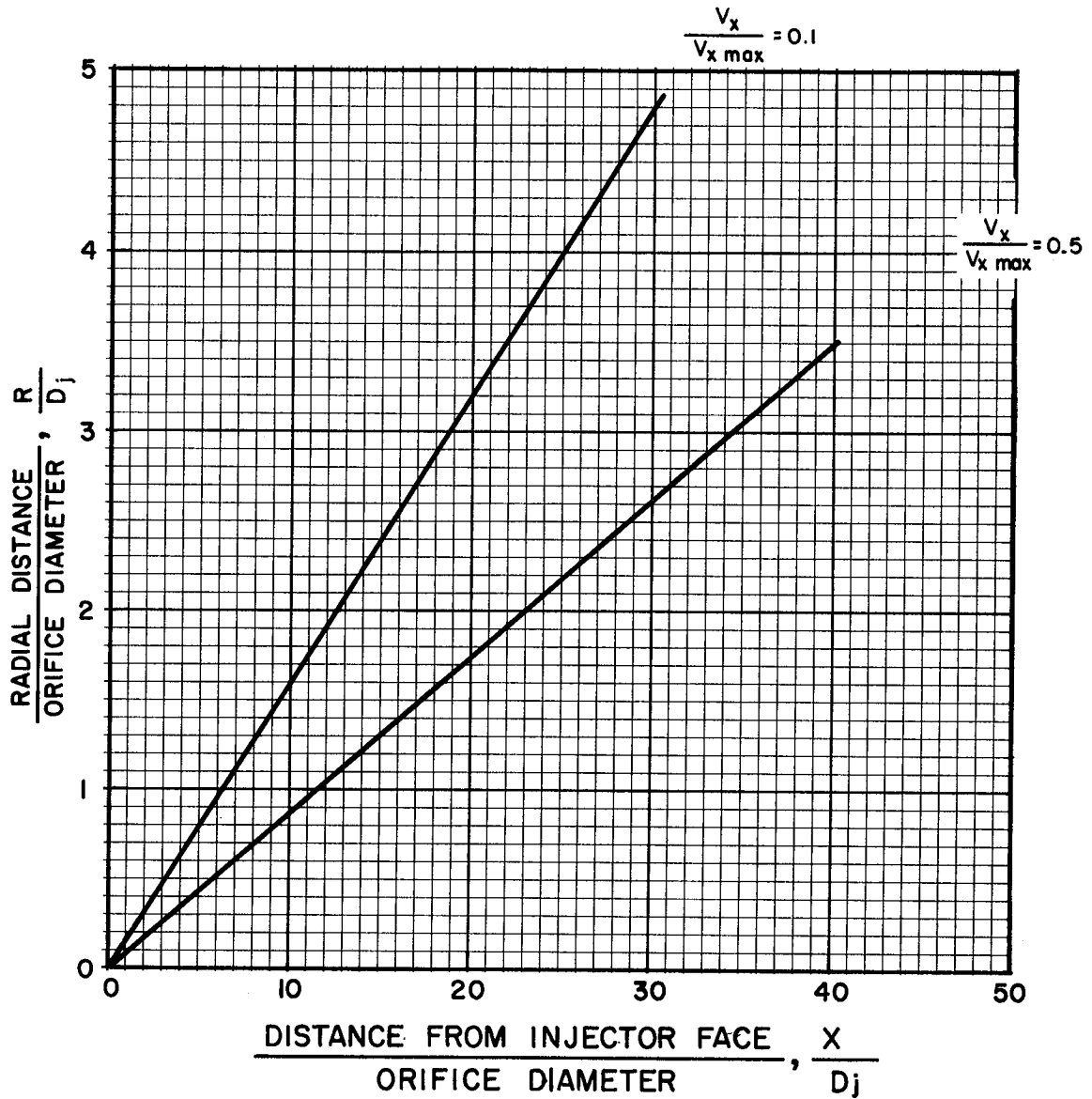
Figure 33. Theoretically Derived Velocity Distributions in Axisymmetric Free Circular Gas Jet. Symbols are Defined in Figure 32. Data from Ref. 10.

Figure 34 shows, to scale, a typical doublet/showerhead element, and indicates the intersections of 500 ft/sec and 100 ft/sec gas jet diameters with the LF_2 fan at a 1 inch distance from the injection plane. This sketch shows qualitatively that the hydrogen jets have a significant enhancing effect on the fluorine atomization, and hence that the doublet/ showerhead pattern should exhibit comparatively high performance.

Both injector designs provide well-atomized sprays, but by different mechanisms. Atomization with the triplet injector involves momentum interchange between the fluorine streams and much higher velocity hydrogen jets, because liquid-gas contact occurs very close to the injector face. The liquid streams are atomized by the gas jet before they impinge upon each other*. With the doublet/showerhead injector, atomization proceeds in two steps: (1) momentum interchange between the impinging streams to form ligaments and large drops, followed by (2) atomization of the liga- ments and large drops by momentum interchange with the diverging, decreasing- velocity gas jets. The end results (atomization of streams by high-velocity gas or of ligaments-large drops by lower-velocity gas) are similar, with the triplet atomization somewhat better than that of the doublet/showerhead.

*Other Rocketdyne investigations (Ref. 8) have indicated that an improved triplet design would allow the liquid streams to impinge, to utilize the liquid momentum for atomization as well as that of the gas. This could be accomplished, for example, by reduction of gas injection velocity.
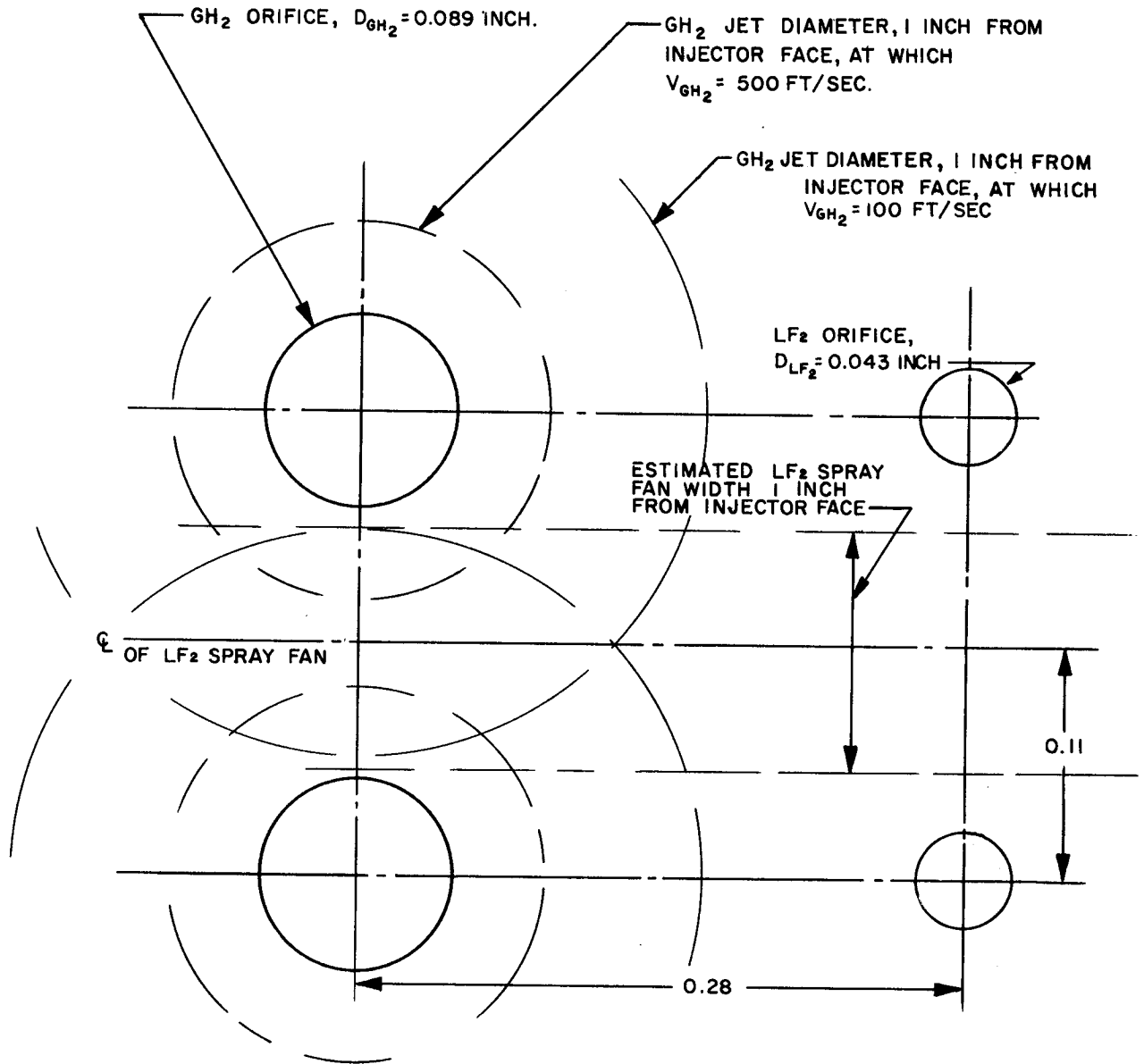
Figure 34. Typical Geometry, Doublet/Showerhead Injector, Showing Intersection of LF_2 Fans with GH_2 Jets at Varying Distances from Injector Face.

HEAT TRANSFER

Boundary Layer Correlations and Heat Transfer Modes

The major portion of thrust chamber heat flux is convective, with secondary contributions of varying magnitude arising from radiation and chemical recombination. Correlations of thrust chamber heat transfer data may be made by application of the standard pipe-flow equation for forced convection heat transfer:

$$Nu = K_1 \, (Re)^m \, (Pr)^{0.33} \tag{5}$$

where

$$Nu \quad = \quad \text{Nusselt number} = h_g'' \, D/k$$

$$Re \quad = \quad \text{Reynolds number} = \rho \, U \, D/\mu$$

$$Pr \quad = \quad \text{Prandtl number} = \mu c_p / k$$

$$K_1, m \quad = \quad \text{constants}$$

$$h_g'' \quad = \quad \text{convective heat transfer coefficient, } Btu/in^2\text{-sec-F}$$

$$D \quad = \quad \text{diameter, in}$$

$$k \quad = \quad \text{thermal conductivity, } Btu/in\text{-sec-F}$$

$$\rho \quad = \quad \text{local gas density, } lb/cu\ in.$$

$$U \quad = \quad \text{free stream local gas velocity, } in/sec$$

$$\mu \quad = \quad \text{viscosity, } lb/in\text{-sec}$$

$$c_p \quad = \quad \text{specific heat, } Btu/lb\text{-F}$$

Variations in boundary layer regime are indicated by changes in the value of m, the Reynolds number exponent, in Eq. 5. Thus, for laminar flow, m = 0.5 (Ref. 17), and for turbulent flow, m = 0.8 (Ref. 18). In the transition region from laminar to turbulent boundary layers, the value of m is generally in the range 1 to 2. It follows that an indication of the nature of the local boundary layer may be experimentally obtained by establishment of the applicable value of the Reynolds number exponent.

Equation 5 may be written in the form

$$\frac{h''_g D}{k_r} = K_1 \left(\frac{D U \rho_r}{\mu_r} \right)^m \left(\frac{\mu_r c_{p_r}}{k_r} \right)^{0.33} \tag{6}$$

where the subscript r indicates property evaluation at a reference temperature (T_r) which is the arithmetic mean of static (T_s) and wall (T_w) temperatures:

$$T_r = 1/2 \left(T_s + T_w \right) \tag{7}$$

Equation 6 reduces to

$$h''_g = \left[\frac{K_1}{D (Pr)^{0.67}} \right] \left[\left(\frac{D U \rho_s}{\mu_r} \right) \left(\frac{\rho_r}{\rho_s} \right) \right]^m \left[\mu_r c_{p_r} \right] \tag{8}$$

where

ρ_s = combustion gas static density

At constant pressure, such as exists at a given axial chamber location,

$$\frac{\rho_r}{\rho_s} = \frac{T_s}{T_r} = \frac{T_o \, (T_s/T_o)}{1/2 \, (T_s + T_w)} = \frac{2T_o \, (T_s/T_o)}{T_o \, (T_s/T_o) + T_w} \qquad (9)$$

where

T_o = stagnation temperature

Further,

$$U \, \rho_s = \dot{w}_T/A \qquad (10)$$

where

$\dot{w}_T$ = total flowrate

A = local cross-sectional chamber area

If $(Pr)^{0.67}$ is assumed to be constant (the actual variation over the experimental range was ±0.5 percent), substitution of Eq. 9 and 10 into Eq. 8 gives:

$$\frac{h''_g}{\mu_r c_{p_r}} = K_2 \left[\left(\frac{2.55 \, \dot{w}_T}{D \, \mu_r} \right) \left(\frac{T_s}{T_s + T_w} \right) \right]^m \qquad (11)$$

where

K_2 = constant

The value of m at a given axial location may be determined from a plot
of the left-hand side of Eq. 11 against the quantity within the brackets.
With reference to convective heat transfer only, the slope of such a
curve provides an indication of the nature of the boundary layer under the
given experimental conditions.

The experimentally measured heat transfer coefficients necessarily include
effects of radiation from the combustion gases and of chemical recombination
at the chamber walls. Hence, suitable corrections for these nonconvective
heat fluxes must be applied; their magnitudes were established as described
below.

Recombination effects were calculated from the following equation (Ref. 19)
by assuming that the combustion gas exists in a state of chemical equilibrium
defined by the local static temperature and that dissociation is not signif-
icantly affected by pressure at the wall temperature of interest:

$$\frac{(h_g)_{recom.}}{(h_g)_{frozen}} = \frac{(\Delta H)_{equilibrium}}{(\Delta H)_{frozen}} = \frac{(H_{gas} - H_{wall})_{equilibrium}}{(c_p)_{frozen}(T_{gas} - T_{wall})} \quad (12)$$

where

H = total enthalpy, obtained from performance calculations, cal/gram

c_p = specific heat, cal/gram/K

T = temperature, K

Equation 12 gives the maximum potential increase in heat transfer coefficient
caused by recombination. The heat flux actually provided by this source is
a function of the particular experimental conditions and may not reach the
maximum equilibrium value.

Radiation heat flux from the combustion gases to the chamber walls was estimated from the Stefan-Boltzmann equation by the method of Ref. 19, assuming that HF was the only important emitting species and defining the geometric beam length, ℓ, as follows:

$$\ell = \left(\frac{4\ V}{A}\right)^{0.9}$$

where

V = volume of radiating gas

A = area being irradiated

This method of calculation estimates the gray gas emissivity of HF from theoretical spectral data for the 2.7-μ fundamental vibration band, as a function of temperature and HF partial pressure-beam length product $(P_{HF}\ell)$. Contributions of the HF harmonic bands are not included, hence the true radiative heat flux is probably underestimated, to a small degree, by this calculation.

Figure 35 shows the ratio of radiative to total (i.e., measured) heat flux

$$\left(\frac{q}{A}\right)_{RAD} \Big/ \left(\frac{q}{A}\right)_{MEAS}$$

in the combustion chamber (average of axial positions 4 and 5, which were nearly identical) and immediately upstream of the throat (axial position 6). Data from both injectors are comparable. In the chamber, the proportion of radiative heat flux increases with decreasing chamber pressure and is slightly dependent upon mixture ratio. This figure illustrates that radiation may be
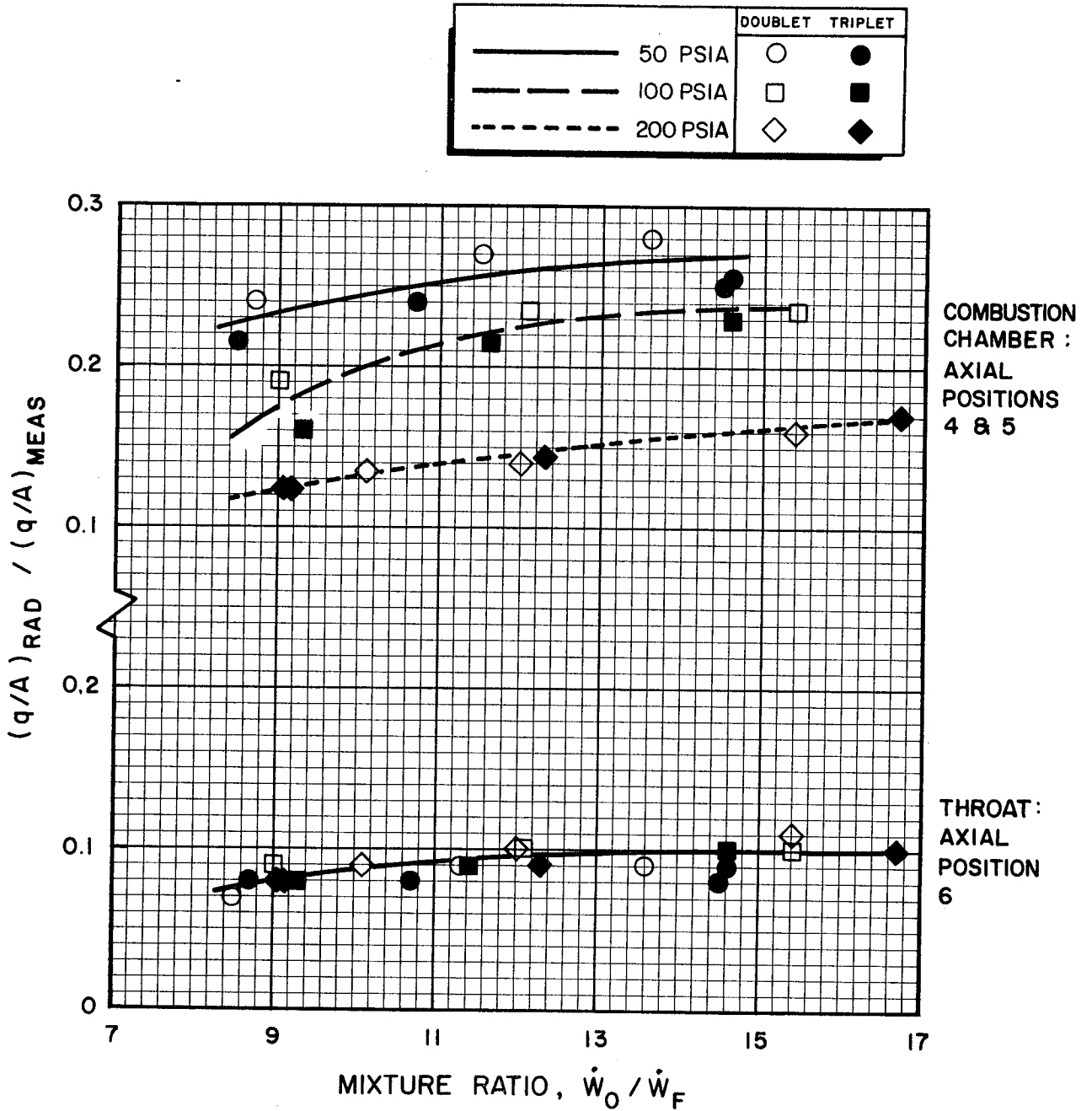
Figure 35. Estimated Heat Flux due to Radiation as Fraction of Total Measured Heat Flux.

an important contributor to chamber heat flux (up to 25 percent of total), particularly at the lower chamber pressures. Corresponding ratios at the throat section indicate no significant variation with chamber pressure and only very slight dependency upon mixture ratio. The ratio of radiative to total heat flux at this location is 8 to 10 percent over the experimental chamber pressure-mixture ratio matrix.

Measured heat transfer coefficient, h_g, is a lumped, effective value defined by the equation:

$$\left(\frac{q}{A}\right)_T = h_g \ (T_{aw} - T_w) \tag{13}$$

where

$\left(\frac{q}{A}\right)_T$ = total (i.e., measured) heat flux

h_g = overall heat transfer coefficient

T_{aw} = adiabatic wall temperature

T_w = wall temperature

Equations 12 and 13 may be used to define another heat transfer coefficient, h''_g, which relates only to convective transfer, by the following expression:

$$\left(\frac{q}{A}\right)_T = \left[h''_g \ (T_{aw} - T_w)\right] \left[\frac{H_{aw} - H_w}{\left(c_p\right)_{frozen} \left(T_{aw} - T_w\right)}\right] + \left(\frac{q}{A}\right)_{RAD} \tag{14}$$

where

$\left(\dfrac{q}{A}\right)_T$ = heat flux

h''_g = convective heat transfer coefficient

T = temperature

H = enthalpy

c_p = specific heat

Subscripts:

T = total or measured

aw = adiabatic wall

w = wall

RAD = radiation

Thus,

$$ h''_g = \left[\left(\frac{q}{A}\right)_T - \left(\frac{q}{A}\right)_{RAD} \right] \left[\frac{(c_p)_{frozen}}{H_{aw} - H_w} \right] \tag{15} $$

Ratios of the "convective" heat transfer coefficient, h''_g, to overall heat transfer coefficient, h_g, are plotted in Fig. 36, for the combustion chamber and throat. The former are averages of values at axial position 4 and 5, which are nearly identical to each other, and the latter are averages of values at axial positions 6 and 7, which also are nearly identical.

With increasing proportion of heat flux contribution from radiation and recombination, the ratio h''_g/h_g decreases. Increasing mixture ratio (and accompanying increasing temperature) at a given chamber pressure increases

87
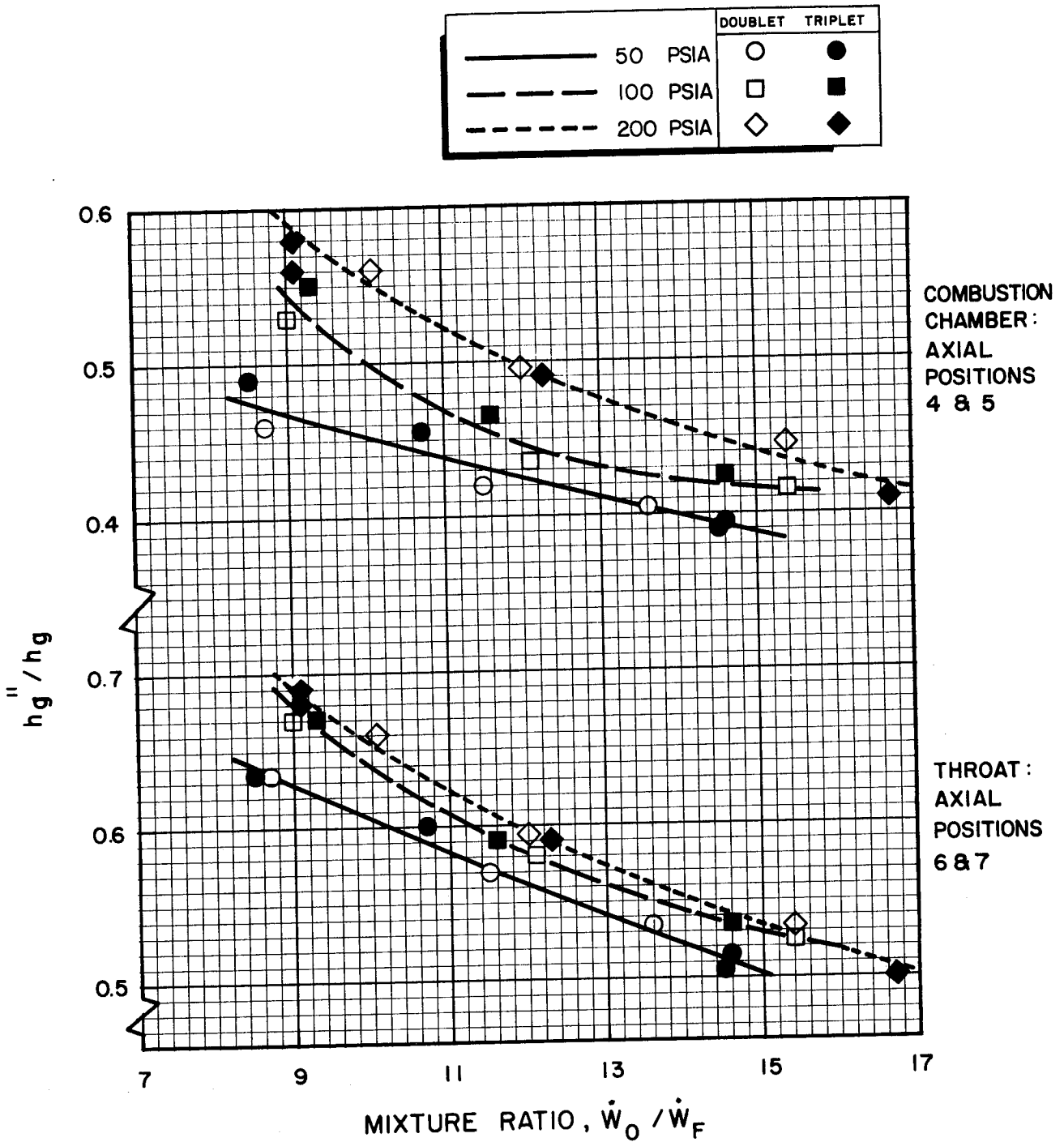
Figure 36. Ratio of Convective Heat Transfer Coefficient (h_g'') to Measured Heat Transfer Coefficient (h_g), after Correcting for Estimated Contributions of Radiation and Chemical Recombination.

the radiative contribution, but increase in chamber pressure (and accompanying decreasing ratio of radiative to total heat flux) raises the h''_g/h_g ratio. At low chamber pressures and high mixture ratios, heat flux arising from recombination and radiation may account for up to 60 percent of the total flux in the combustion chamber and up to 50 percent in the throat, provided recombination proceeds to equilibrium.

To obtain possible indications of the nature of the boundary layer regimes along the thrust chamber under varying experimental conditions, Eq. 11 was plotted at each axial location. Three heat transfer coefficients were used:

h_g = overall heat transfer coefficient

h'_g = overall value less radiative contribution

h''_g = convective heat transfer coefficient (overall value less radiative and maximum recombination contributions)

Typical plots, one in the combustion chamber and one in the nozzle, are shown in Fig. 37 (axial position 4, 8.5 inches from injector face) and Fig. 38 (axial position 6, 1.8 inches upstream of geometric throat) respectively. For convenience, the h''_g points are all at mixture ratio 12, while the h_g and h'_g points include mixture ratios 9 and 15 as well, to illustrate the range of values.

Convective pipe-flow heat transfer correlations, such as Eq. 11, should be applied to experimental thrust chamber heat flux data only when corrections are made for heat fluxes caused by radiation and recombination, or when these sources can be shown to have no significant effects upon the correlations. For the particular case of fluorine-hydrogen combustion in the 50- to 200-psia chamber pressure range, not only are radiation heat
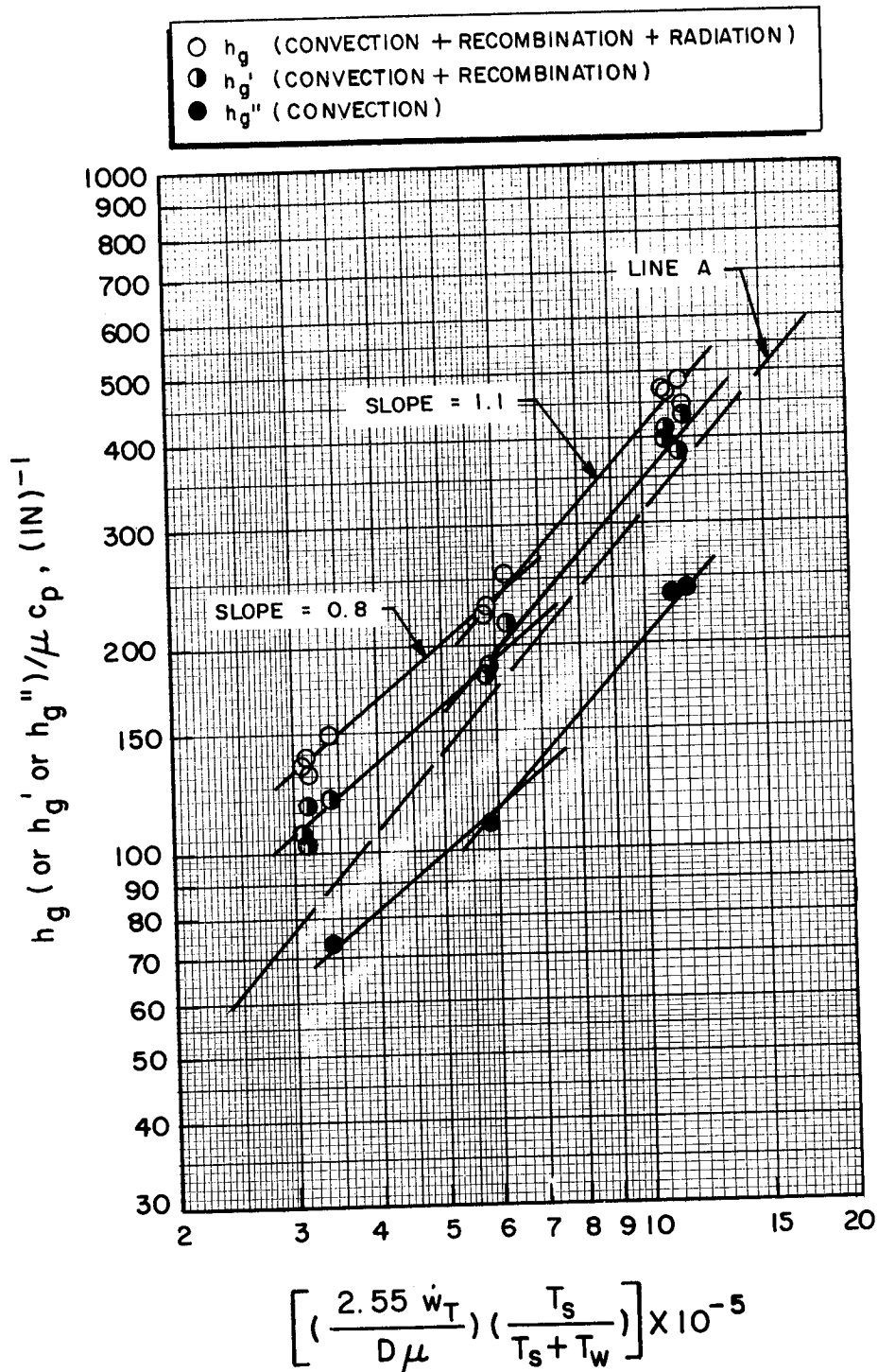
Figure 37. Plots of Equation 11, for Each of the Three Indicated Heat Transfer Coefficients. Triplet Injector, Axial Position 4 (in Combustion Chamber)

Figure 38. Plots of Equation 11, for Each of the Three Indicated Heat Transfer Coefficients. Triplet Injector, Axial Position 6 (Immediately Upstream of Geometric Throat)
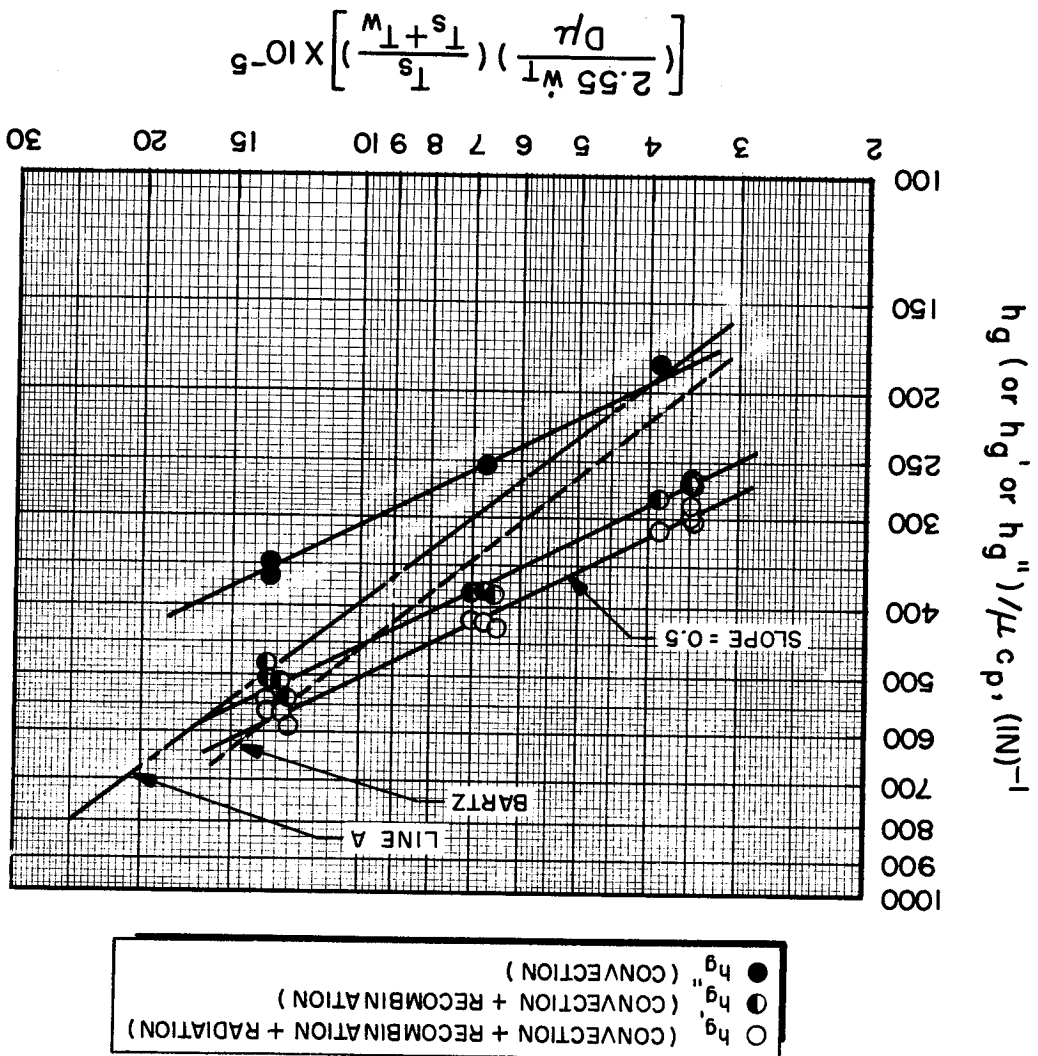
fluxes of significant magnitude, but the extent of the kinetically limited recombination reactions in the boundary layers is not known. Hence conclusions as to the nature of the local boundary layer regime based upon slopes of lines through h_g, h_g', or h_g'' may not be valid.

As an example, consider Fig. 37. Although slopes of the lines representing h_g, h_g', or h_g'' are all 0.8 at the lower level and 1.1 at the higher, this should not be construed as necessarily indicating a turbulent boundary layer $(m = 0.8)$ transforming to transitional $(m = 1.1)$. Because recombination effects increase with decreasing chamber pressure, the true convective heat transfer coefficients may be represented by a line such as line A $(m = 1.2)$ indicating transitional boundary layers over the entire range of flowrate.

At the axial position representing throat conditions (Fig. 38), similar considerations apply. Although $m = 0.5$ for all of the lines representing h_g, h_g', and h_g'', this is not necessarily an indication of laminar boundary layers. The true convective heat transfer coefficients, represented, for example, by line A, may have a slope closer to $m = 0.8$ because of greater recombination effects at the lower flowrates. Comparison of the experimental data with calculations based upon the Bartz equation for turbulent boundary layers (Ref. 20), also shown in Fig. 38, indicates that this may indeed be the case.

Comparison of Experimental Results with Predicted Values

Estimates of thrust chamber heat transfer coefficients are most frequently made by application of the Bartz simplified solution (Ref. 20) or the Mayer analysis (Ref. 21). The Bartz solution assumes turbulent boundary layers and is based on the pipe-flow correlation of Eq. 5. The Mayer boundary layer analysis is based on an approximate solution of the energy

integral equation and develops results for both turbulent and laminar boundary layers.

Other analytical predictions, based on boundary layer analyses or upon simple pipe-flow relations, have been reported. For example, one method (Ref. 22), which modifies the turbulent boundary layer analysis of Ref. 23, predicts heat transfer characteristics when nozzle geometry, wall temperatures, and free-stream properties are specified and initial values of boundary layer thicknesses are assumed. Another method (Ref. 24) uses a form of the pipe-flow equation for fully developed flow in which both the thermal and velocity boundary layers extend to the centerline and there is no significant pressure gradient. The Bartz and Mayer predictions are indicative of the orders of magnitude obtained from typical analyses.

Realistic predictions of thrust chamber heat transfer coefficients should be based on convective contributions estimated from appropriate boundary layer analyses augmented by applicable chemical recombination and radiative contributions. Customarily, however, the estimates obtained from the Bartz or Mayer equations are used, both based on convective turbulent boundary layer analyses, so that when nonturbulent boundary layers exist and/or when recombination and radiation effects are significant, these estimates may differ substantially from experimental values.

Comparisons of experimental values of h_g (overall) with the Bartz and Mayer predictions are shown in Fig. 39, 40 and 41 for the nozzle region of the 30-inch L* chamber, at mixture ratio 12, and chamber pressures of 50, 100, and 200 psia respectively. Predicted values were calculated by use of existing Rocketdyne computer programs (Ref. 25). The curves of Fig. 39, 40, and 41 indicate that:

1. In the converging portion of the nozzle, experimental heat transfer coefficients are approximately 40 percent higher
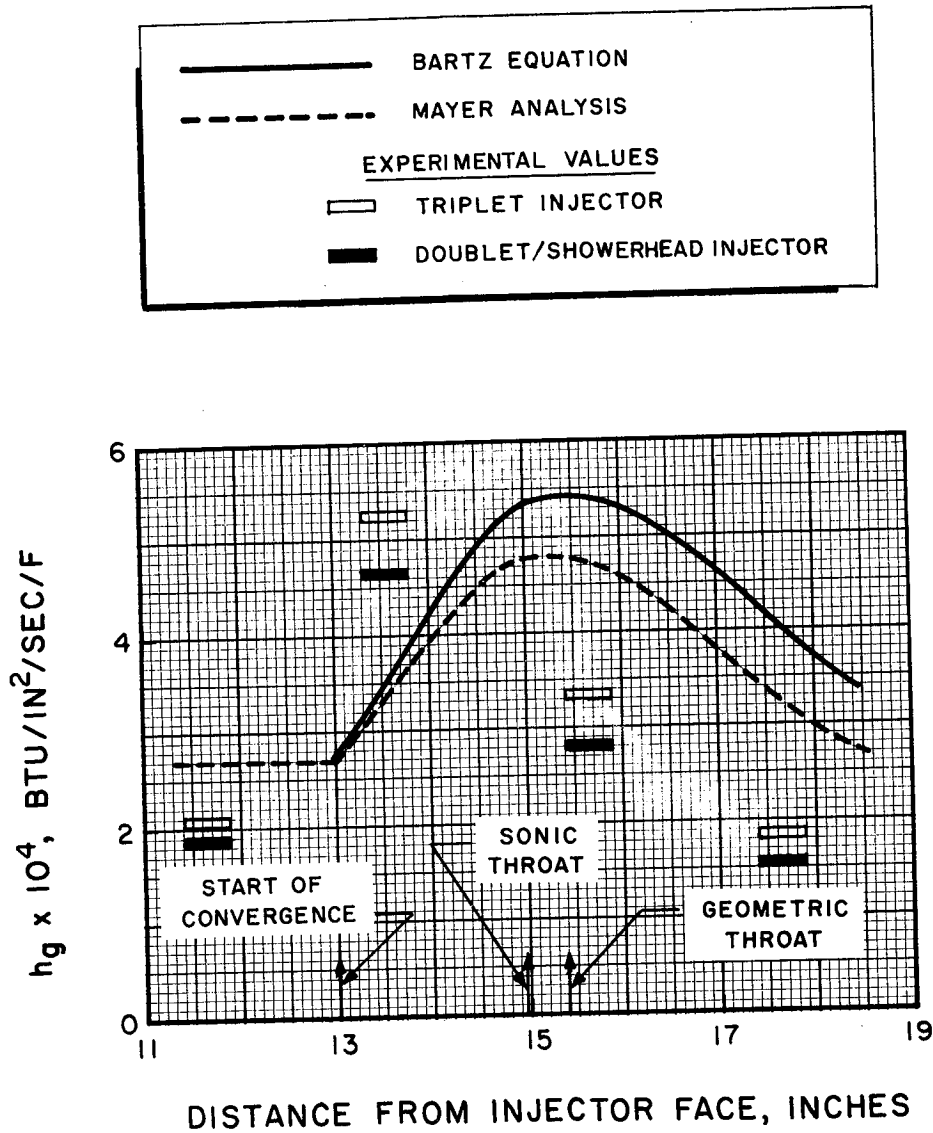
Figure 39. Comparison of Experimentally Observed Heat Transfer Coefficients in the Nozzle Region of the 30-Inch L* Chamber with Values Obtained from the Bartz and Mayer Calculations. P_c = 50 psia, M.R. = 12.
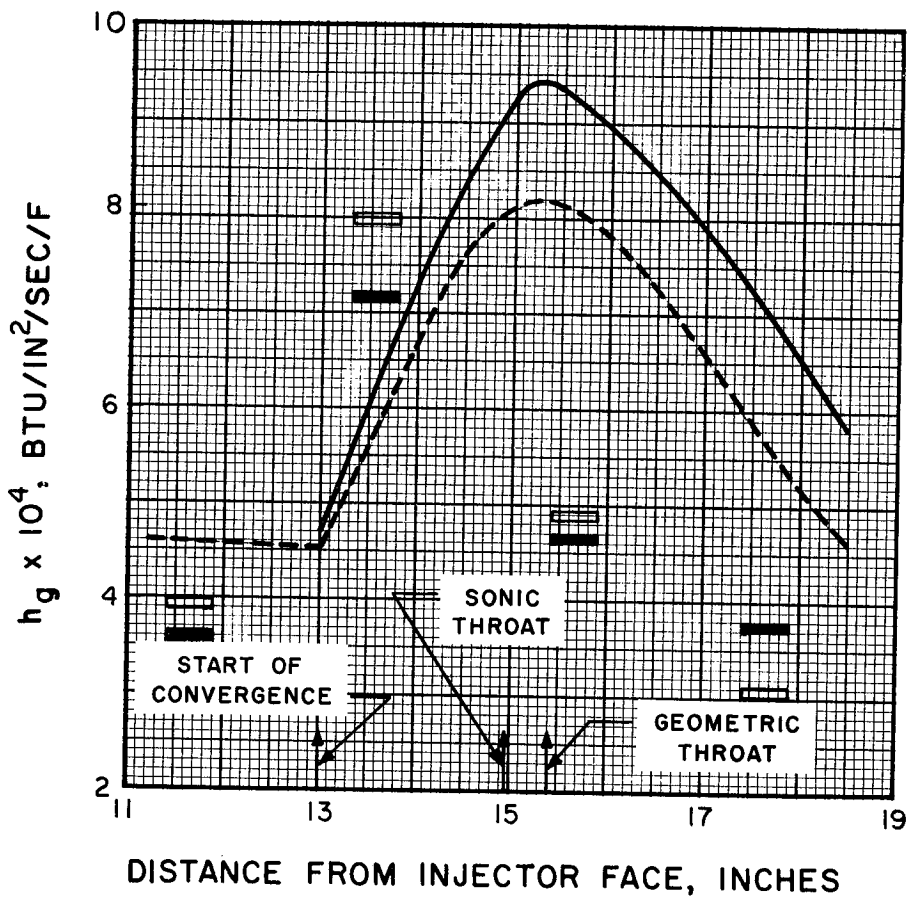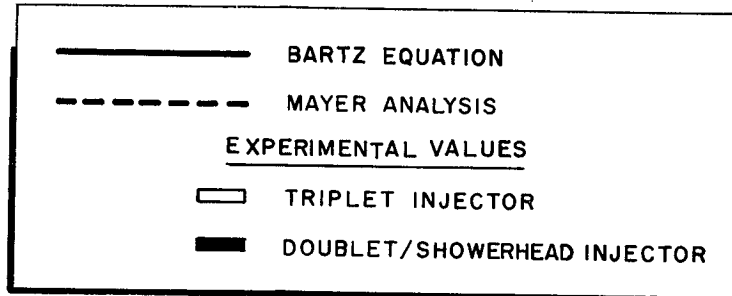
Figure 40. Comparison of Experimentally Observed Heat Transfer
Coefficients in the Nozzle Region of the 30-Inch L*
Chamber with Values Obtained from the Bartz and
Mayer Calculations. P_c = 100 psia, M.R. = 12.
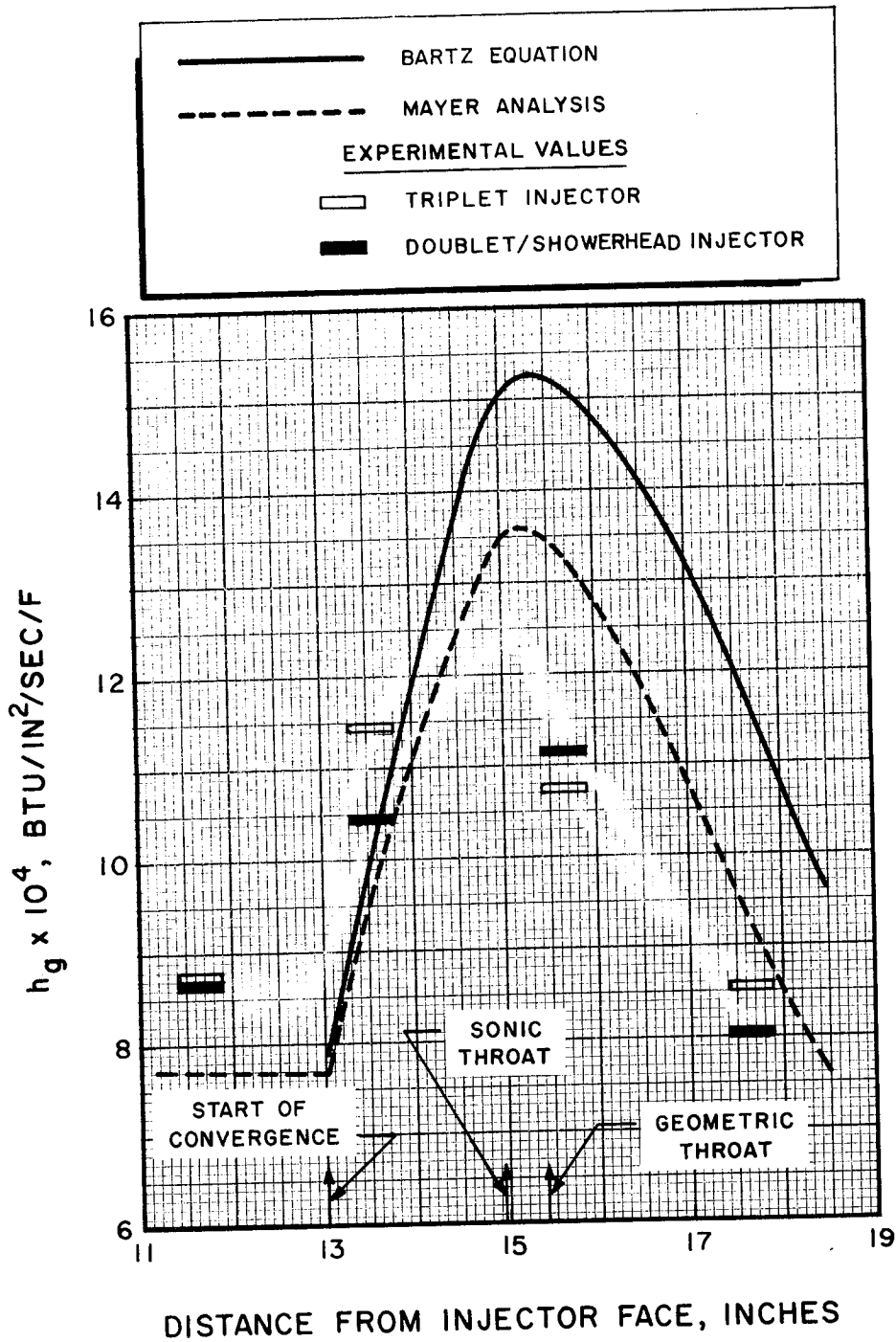
Figure 41.   Comparison of Experimentally Observed Heat Transfer
Coefficients in the Nozzle Region of the 30-Inch L*
Chamber with Values Obtained from the Bartz and
Mayer Calculations. P_c = 200 psia,   M.R. = 12.

than predicted at 50-psia chamber pressure. The difference becomes less with increasing chamber pressures: 25 percent at 100 psia and negligibly small at 200 psia. This reflects the increasing relative heat flux caused by chemical recombination with decreasing chamber pressure, as described above, and also indicates that the boundary layer is probably turbulent.

2. Immediately downstream of the throat, experimental heat transfer coefficients are 40 percent (at 50 psia) to 20 percent (at 200 psia) lower than predicted values. These results, which are similar to those obtained in other studies of rocket nozzle heat transfer, may be ascribed to factors such as the following: (a) predicted values are based on maximum heat flux at the geometric throat, instead of at the sonic throat, which has the effect of displacing the Bartz and Mayer curves towards the downstream end; and (b) substantial deviations from one-dimensional flow occur just downstream of the throat (Ref. 24) so that heat transfer predictions based on one-dimensional flow would not be expected to be valid in this region.

Combustion Chamber Heat Flux

Heat flux in the combustion chamber was highest near the injector, in the region of maximum combustion heat release. This effect was particularly evident in the firings at 200-psia chamber pressure (Fig. 21 and 22); it was more pronounced in the case of the triplet injector than for the doublet/showerhead, which is further indication that combustion takes place closer to the injector face in the former pattern. Further, heat flux at the injector end of the chamber varied substantially with mixture ratio, unlike that in the rest of the thrust chamber. This is a reflection of altered propellant distribution and atomization characteristics with changing flowrates and injector pressure drops.

No methods are available for prediction of combustion chamber heat flux on the basis of uniform-flow convective heat transfer analyses. Qualitative estimates may be made, for combustion chambers which are significantly longer than the extent of the combustion zone, by extending the Bartz or Mayer h_g predictions at the nozzle entrance upstream into the combustion chamber, until effects of the combustion zone become predominant, with a slight upward slope to account for decreasing boundary layer thickness with decreasing chamber length. This change is clearly shown in the experimental data (Fig. 21 and 22).

CONCLUDING REMARKS

The high performance efficiencies exhibited by both triplet and doublet/ showerhead injectors demonstrate the reliability of the criteria upon which their designs were based.

These designs, however, were planned for a heat-sink, comparatively long-length thrust chamber, and therefore placed no emphasis on requirements for, or optimization of, various factors which are of importance in flight-type hardware. Such factors include propellant injection velocity, which is determined by supply pressure, thrust per element, which influences injector complexity, and combustion chamber length, which relates to the choice and complexity of the chamber cooling method and to thrust chamber weight. Studies of the effects of these factors on injector performance are required to extend the establishment of propellant atomization and distribution requirements for high performance over a range of propellant injection conditions and injector complexity. These studies would also provide experimental bases for some of the trade-offs which are inevitable in engine design.

Propellant atomization and distribution characteristics influence not only performance, but thrust chamber heat transfer as well. Hence, experimental studies of the effects of injector geometry on chamber and nozzle heat flux are prerequisite to engine design. Variation of heat flux character-istics with injector geometry would also influence the choice of cooling method for a particular flightweight chamber. Evaluation of cooling methods (e.g., ablative, regenerative, or combinations of the two) should therefore be considered in parallel to an injector-chamber overall optimization program.

REFERENCES

1. Price, H. G., Jr., R. J. Lubick, and A. M. Shinn, Jr., Investigation of Injectors for a Low-Chamber Pressure Hydrogen-Fluorine Rocket Engine, NASA Technical Memorandum No. X-485, July 1962, CONFIDENTIAL.

2. Aukerman, C. A. and B. E. Church, Experimental Hydrogen-Fluorine Rocket Performance at Low Pressures and High Area Ratios, NASA Technical Memorandum No. X-724, September 1963, CONFIDENTIAL.

3. Nagai, C. and J. P. Bott, Investigation of High-Performance Upper-Stage Engines Employing Liquid Fluorine Oxidizer, Research Report No. RR 64-41, Rocketdyne, a Division of North American Aviation, Inc., Canoga Park, California, November 1964.

4. Bott, J. P. and D. A. Nelson, LF_2/GH_2 Toroidal Engine Performance and Heat Transfer Study, Research Report No. 66-2, Rocketdyne, a Division of North American Aviation, Inc., Canoga Park, California, February 1966.

5. Combs, L. P., and F. W. Hoehn, Steady-State Rocket Combustion of Gaseous Hydrogen and Liquid Oxygen. Part I: Experimental Investigation, Research Report No. RR 64-24, Rocketdyne, a Division of North American Aviation, Inc., Canoga Park, California, June 1964.

6. Priem, R. J. and M. F. Heidmann, Propellant Vaporization as a Design Criterion for Rocket Engine Combustion Chambers, NASA Technical Report No. TR-R-67, 1960.

7. Ingebo, R. D., Drop-Size Distributions for Impinging-Jet Breakup in Airstreams Simulating the Velocity Conditions in Rocket Combustors, NACA Technical Note No. TN-4222, March 1958.

8. Nurick, W. H., and S. D. Clapp, The Establishment of General Injector Design Criteria with Special Emphasis on Gas/Liquid Propellant Applications, Research Report (In Press), Rocketdyne, a Division of North American Aviation, Inc., Canoga Park, California,

9. Heckert, B. J., and S. D. Clapp, Preliminary Study of Liquid Atomization by a Gas, Research Report No. RR 65-22, Rocketdyne, a Division of North American Aviation, Inc., Canoga Park, California, April, 1965.

10. Scull, W. E., and W. R. Mickelsen, "Flow and Mixing Processes in Combustion Chambers", in Basic Considerations in the Combustion of Hydrocarbon Fuels with Air, NACA Report No. 1300, 1958.

11. Grey, J., "Calibration of Turbine Flowmeters for Cryogenic Operations", ARS Journal, Vol. 30, February 1960, pp. 192-193.

12. Bulletin for Model 10C1510 and 10C1511 Turbine Flowmeters, Division 1, Fischer & Porter Company, Warminster, Pennsylvania, Publication No. 14815, p. 13.

13. A.S.M.E. Research Committee on Fluid Meters, Fluid Meters-Their Theory and Application, American Society of Mechanical Engineers, New York, N. Y., Fifth Edition, 1959, p. 81.

14. Design Handbook for Liquid Fluorine Ground Handling Equipment, Technical Report No. AFRPL-TR-65-123, Second Edition, Air Force Rocket Propulsion Laboratory, Edwards Air Force Base, California, August 1965.

15. Shapiro, A. H., The Dynamics and Thermodynamics of Compressible Fluid Flow, Vol. II, Ronald Press Company, New York, N. Y., 1954, p. 832.

16. Ingebo, R. D., and H. H. Foster, Drop Size Distribution for Cross-Current Breakup of Liquid Jets in Airstreams, NACA Technical Note No. TN-4087, 1957.

17. Eckert, E. R. G., and R. M. Drake, Jr., Heat and Mass Transfer, McGraw-Hill Book Company, New York, N. Y., 1959, p. 176.

18. McAdams, W. H., Heat Transmission, Third Edition, McGraw-Hill Book Company, New York, N. Y., 1954, p. 219.

19. Chamber Technology for Space-Storable Propellants-Task I, Interim Report, Vol. 1, Report No. R-6028-1, Prepared for NASA by Rocketdyne, a Division of North American Aviation, Inc., Canoga Park, California, Contract No. NAS7-304, 13 October 1965.

20. Bartz, D. R., "A Simple Equation for Rapid Estimation of Rocket Nozzle Convective Heat Transfer Coefficients", Jet Propulsion, Vol. 27(1), January 1957, pp. 49-51.

21. Mayer, E., "Analysis of Convective Heat Transfer in Rocket Nozzles", ARS Journal, Vol. 31, July 1961, pp. 911-917.

22. Elliot, D. G., D. R. Bartz, and S. Silver, Calculation of Turbulent Boundary Layer Growth and Heat Transfer in Axi-Symmetric Nozzles, Report No. 32-387, Jet Propulsion Laboratory, Pasadena, California, 15 February 1963.

23. Bartz, D. R., "An Approximate Solution of Compressible Turbulent Boundary-Layer Development and Convective Heat Transfer in Convergent-Divergent Nozzles", Trans. A.S.M.E., Vol. 77, No. 8, 1955, pp. 1235-1245.

24. Back, L. H., P. F. Massier, and H. L. Gier, Convective Heat Transfer in a Convergent-Divergent Nozzle (Revision No. 1), Report No. 32-415, Jet Propulsion Laboratory, Pasadena, California, 15 February 1965.

25. Madrigal, A., Gas-Side Heat Transfer Coefficient Comparison Program, Report No. CDR 2126-2020, Rocketdyne, a Division of North American Aviation, Inc., Canoga Park, California, 21 March 1963.

APPENDIX A

DESIGN OF CHAMBER WALL HEAT FLUX ISOLATION SEGMENTS

INTRODUCTION

This appendix gives the criteria used for design of the heat flux isola-
tion segments machined into the walls of the calorimetric thrust chamber.
The method of heat flux measurement used in the present investigation was
developed in several previous Rocketdyne research programs (Ref. A-1, A-2,
A-3, A-4) and consists essentially of providing thermally isolated areas
or segments in the chamber wall which, when subjected to the hot combus-
tion gas environment, exhibit approximately one-dimensional transient
temperature response. A thermocouple peened to the cold side of the
segment provides temperature-time data from which heat fluxes and heat
transfer coefficients may be calculated. Figure A-1 shows a typical,
circular isolation segment.

Heat flux isolation segment design involves establishment of the character-
istic dimensions (a, b, L, and d) indicated in Fig. A-1 to meet certain
requirements. Thus, the slot around the segment, which isolates it from
side conduction effects, may have as small a gap width, a, as can be
practically machined, because of the low thermal conductivity of air.
Side conduction effects, however, are also influenced by the wall thick-
ness, b, and will be kept to a minimum by making this wall thickness as
small as possible; minimum values of b are determined from stress consid-
erations. Further, although minimizing the segment length, L, simplifies
data reduction, the practical minimum segment length which can be used
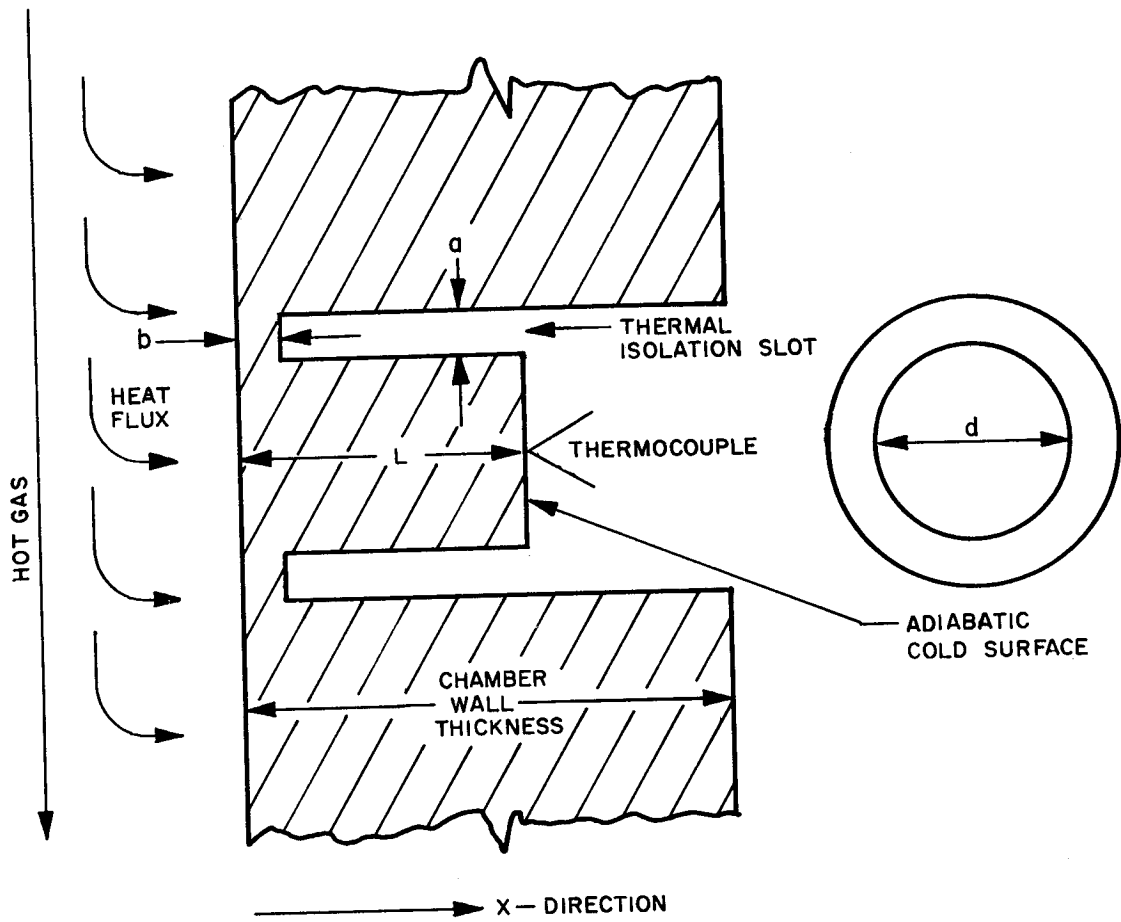
Figure A-1. Schematic Cross-Section of Heat Transfer Segment Machined into the Thrust Chamber Wall.

for a given heat transfer rate, driving temperature, and firing duration is limited by the maximum allowable inside wall temperature. In addition, to make the measured heat flux data at each isolation area approximate point values as closely as possible, the segment diameter, d, should be minimized, within the practical limitation of providing enough area for peening thermocouples to the cold side. These design considerations are summarized in Table A-1.

TABLE A-1

DESIGN CONSIDERATIONS FOR ISOLATED HEAT TRANSFER SEGMENT

Parameter	Optimum Dimension	Limitation
Length, L	Minimum (for simple data reduction)	Maximum allowable hot side wall temperature for given run duration
Diameter, d	Mimimum (for approximate "point" data)	Sufficient area for peening thermocouple
Wall Thickness, b	Mimimum (lowest side conduction when b/L is minimized)	Strength requirement to prevent segment blowout
Gap Width, a	Arbitrary (however, a/d should be kept small)	Minimum value that can be machined

DESIGN APPLICATION

Estimate of Heat Transfer Rates

An approximation of the applicable heat transfer coefficients must be made before the design criteria outlined above can be applied. Preliminary estimates of throat Reynolds number indicated turbulent boundary

layer flow in the throat section over the range of operating conditions, and, because transition point in the combustion chamber is not easily predictable, the boundary layer was assumed to be turbulent throughout the motor as well. Heat transfer coefficients and heat fluxes could therefore be approximated by use of the Bartz simplified equation for turbulent heat transfer (Ref. A-5). Maximum estimated values thus obtained (at 200 psia chamber pressure) were as follows:

Heat transfer coefficient:

$$h_g = 8.0 \times 10^{-4} \text{ Btu/in.}^2\text{-sec-F} \qquad \text{(chamber)}$$

$$h_g = 15.3 \times 10^{-4} \text{ Btu/in.}^2\text{-sec-F} \qquad \text{(throat)}$$

Heat flux (assumed: 1200 F wall temperature, $\eta_c^* = 97\%$, Bartz h_g values):

$$q/A = 3.8 \text{ Btu/in.}^2\text{-sec} \qquad \text{(chamber)}$$

$$q/A = 7.2 \text{ Btu/in.}^2\text{-sec} \qquad \text{(throat)}$$

Determination of Minimum Segment Length, L

If heat flux is considered to be one-dimensional in the isolation segment whose length is L, with insulated cold wall (at $x = L$), uniform initial temperature, T_i, and heated by convection at $x = 0$, then temperature histories may be developed from the solution of the one-dimensional Fourier equation (assuming constant properties, constant convective

heat transfer coefficient, and no internal heat generation) with appropriate boundary conditions. The solution applicable to the cold wall of the segment is given by Eq. A-1 (Ref. A-6):

$$\frac{T_{aw} - T_c}{T_{aw} - T_i} = 4 \sum_{n=1}^{\infty} \left(\frac{\sin M_n}{2M_n + \sin 2M_n} \right) \exp \left(-M_n^2 F_o \right) \qquad (A-1)$$

where

T_{aw} = adiabatic recovery temperature

T_c = cold wall temperature

n = 1, 2, 3, ...

F_o = Fourier number = $\alpha\theta/L^2$

α = thermal diffusivity (sq. in./sec) of segment material

θ = time, seconds

The parameter M_n is defined by the following equation:

$$M_n \tan M_n = Bi = \text{Biot number} \qquad (A-2)$$

$$Bi = \frac{h_g L}{k} \qquad (A-3)$$

where

h_g = convective heat transfer coefficient (at x = 0)

k = thermal conductivity of segment material

From a graphic representation of Eq. A-1 (such as Fig. H-5, Appendix H) in the applicable range of variables, the minimum value of L is determined by using a maximum operating temperature as T_{aw} (1200 F for copper), a nominal run duration (3 seconds), and the maximum heat transfer coefficients estimated from the Bartz equation. The results of such analyses are shown in Fig. A-2 (for the combustion chamber) and Fig. A-3 (for the throat section), which indicate the final (i.e., after 3 seconds) hot and cold wall temperatures under conditions of maximum heat transfer (chamber pressure = 200 psia, mixture ratio = 9) as functions of segment length, L. The minimum length necessary to maintain $T_h \leq 1200$ F under these conditions is about 0.5 inches in the chamber (Fig. A-2). In the throat (Fig. A-3), $T_h \leq 1200$ F at 3 seconds is not attained even with L as large as 2 inches. Practical limitations, however, dictate a value of L of 1 inch, indicating that somewhat shorter firing durations should be employed at 200-psia chamber pressure.

Minimum segment length estimation is dependent also upon the initial temperature. Thus, use of Fig. H-5 for a 1-inch-long segment in the throat, with maximum value of h_g, permits calculation of hot wall temperature as a function of run duration. Figure A-4 shows curves for two initial temperatures: 70 F and -320 F. For the former, hot wall temperature of 1200 F is reached in about 2.2 seconds. In the actual firing procedure, however, normal chilldown with liquid nitrogen brings initial segment temperature considerably below ambient. Thus, with allowance for low T_i, run durations of 3 seconds would very probably be feasible at 200-psia chamber pressure, and 2.5-second durations would certainly not be excessive.
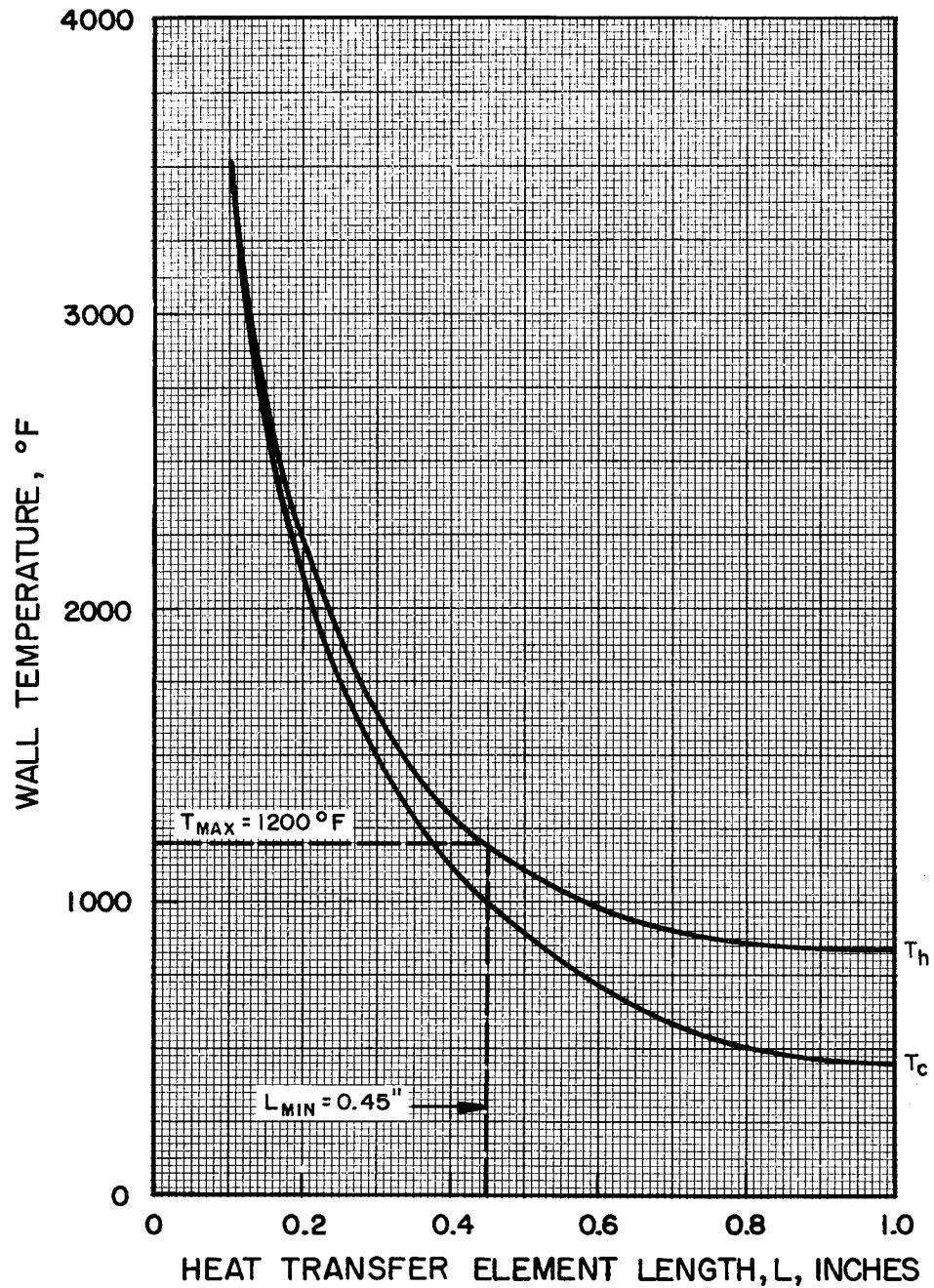
Figure A-2. Effect of Element Length on Hot (T_h) and Cold (T_c) Wall Temperatures at the End of Three-Second Firing. Element Located in Chamber Section. $(h_g = 8.0 \times 10^{-4}$ Btu/sec/in^2/F, $P_c = 200$ psia, M.R. = 9, $T_{initial} = 70F)$.
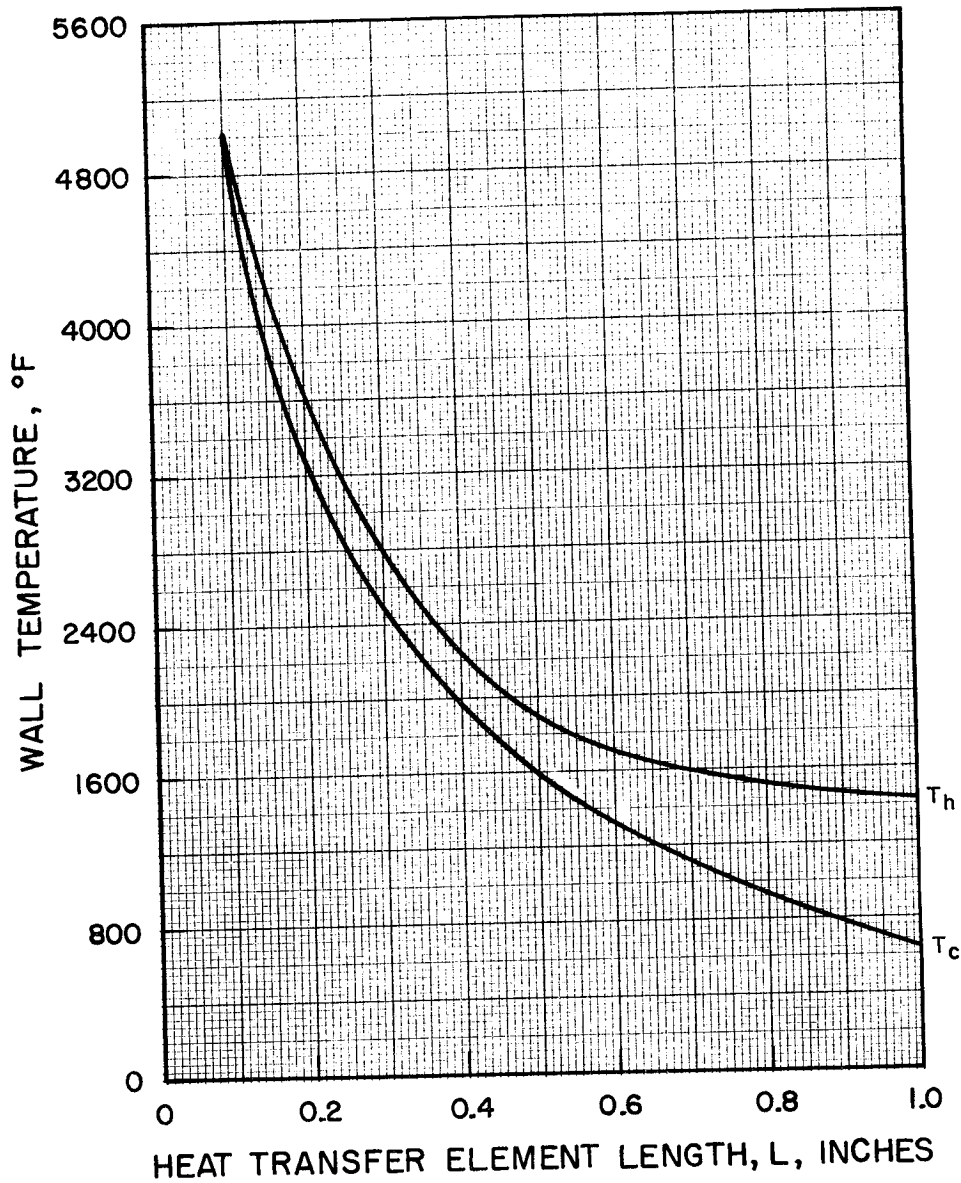
Figure A-3. Effect of Element Length on Hot (T_h) and Cold (T_c) Wall Temperatures at the End of Three-Second Firing. Element Located in Throat Section. (h_g = 15.3 x 10^{-4} Btu/sec/in^2/F, P_c = 200 psia, M.R. = 9, $T_{initial}$ = 70F).
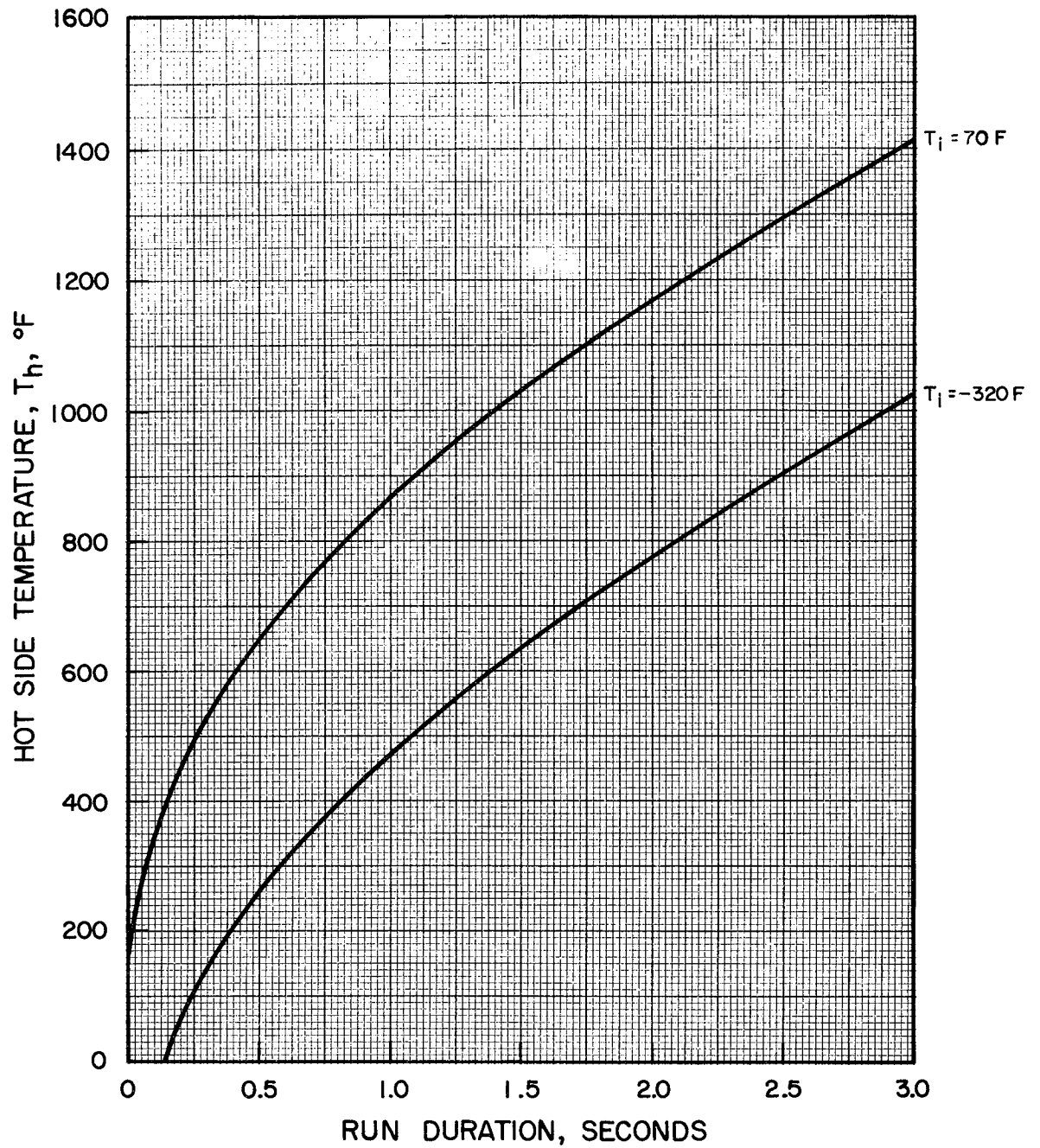
Figure A-4. Hot Side Temperature Histories for a One-Inch-Long Copper Heat Transfer Element Located at the Throat, with Initial Temperature (T_i) of 70F and -320F.

Determination of Segment Diameter, d, and Slot Gap, a

These dimensions are established at the minimum values dictated by practical limitations. Thus, the value of d was set at 0.5 inch, because smaller values would make it difficult to apply thermocouple wires to the cold side of the segment. The value of a was set at 0.032 inches as the minimum value permitting relative ease of fabrication.

Determination of Minimum Wall Thickness, b

For a circular segment of diameter d and wall thickness b (Fig. A-1), the stress over the area between the element and the chamber wall is given by

$$\sigma = \frac{(P_c)\ (\pi\ d^2/4)}{b(\pi\ d)} = \frac{P_c d}{4b} \tag{A-4}$$

Taking the maximum allowable stress of copper at 1200 F as 1500 psi, and substituting numerical values of chamber pressure (200 psi) and d (0.5 inch) into Eq. A-4, gives minimum value of wall thickness:

$$b = \frac{P_c d}{4\sigma} = \frac{(200)\ (0.5)}{(4)\ (1500)} = 0.017 \text{ inches}$$

Wall thickness provided in the chamber design was 0.1 inch, to allow ample margin for fabrication variations and loading safety factor.

REFERENCES

A-1. Kusak, L., Experimental Determination of the Heat Transfer Coeffi-
      cients for an Aerodynamic Strut Located in the Convergent Section
      of the Exhaust Nozzle of an Annular Thrust Chamber, Research Report
      No. RR 60-10, Rocketdyne, a Division of North American Aviation,
      Inc., Canoga Park, California, June 1960.

A-2. Kusak, L., Gemini Injector (25-Pound Thrust Level) Research Program
      Summary Report, Research Report No. 63-14, Rocketdyne, a Division of
      North American Aviation, Inc., Canoga Park, California, April 1963.

A-3. Burge, H. L. and R. Ayvazian, Experimental Rocket Engine Testing
      for Heat Shield Materials Study, Research Report No. 63-21,
      Rocketdyne, a Division of North American Aviation, Inc., Canoga
      Park, California, July 1963.

A-4. Chamber Technology for Space-Storable Propellants – Task II,
      Prepared for National Aeronautics and Space Administration,
      Contract NAS7-304; Rocketdyne, a Division of North American
      Aviation, Inc., Canoga Park, California, 13 October 1965.

A-5. Bartz, D. R., A Simple Equation for Rapid Estimation of Rocket
      Nozzle Convective Heat Transfer Coefficients, Jet Propulsion,
      Vol. 27, January 1957, p. 49.

A-6. Schneider, P. J., Conduction Heat Transfer, Addison-Wesley
      Publishing Company, Inc., Reading, Massachusetts, 1955, p. 235.

APPENDIX B

INJECTOR PRESSURE DROPS AND PROPELLANT INJECTION VELOCITIES

This appendix summarizes nominal and experimental injector pressure drops and injection velocities of both propellants for the triplet and doublet/showerhead designs.

Fluorine

Oxidizer orifice characteristics of the injectors are given in Table B-1.

TABLE B-1

FLUORINE ORIFICE CHARACTERISTICS

Injector	Number of Fluorine Orifices	Diameter, inches	Total Injection Area, sq in.
Triplet	128	0.039	0.1529
Doublet/Showerhead	98	0.043	0.1423

Nominal fluorine flowrates, injector pressure drops, and injection velocities were calculated on the basis of the following assumptions and are listed in Table B-2.

$$\eta_{c*} = 97 \text{ percent}$$

$$A_t = 13.8 \text{ sq in.} \qquad (D_t = 4.20 \text{ inches})$$

$$C_D = 0.80$$

$$\rho_{LF_2} = 97 \text{ lb/ft}^3$$

TABLE B-2

NOMINAL FLUORINE FLOWRATES, INJECTOR PRESSURE DROPS,
AND INJECTION VELOCITIES

P_c, psia	M.R.	$\dot{w}$, lb/sec	Triplet		Doublet/Showerhead	
			ΔP, psi	V, ft/sec	ΔP, psi	V, ft/sec
50	9	2.55	11	25	12	27
	12	2.67	12	26	13	28
	15	2.77	13	27	14	29
100	9	5.06	42	49	46	53
	12	5.30	46	51	51	55
	15	5.49	49	53	54	57
200	9	10.03	163	97	179	104
	12	10.49	177	102	196	109
	15	10.86	191	106	210	113

The experimentally observed fluorine pressure drops are plotted in
Fig. B-1 (triplet) and Fig. B-2 (doublet/showerhead). Excluding the val-
ues at the lowest flowrates, the former correspond to C_D = 0.74 and the
latter to C_D = 0.75. The pressure drops observed at 50-psia chamber
pressures, i.e., at the lowest flowrates, are anomalously high for both
injectors. This is most likely caused by partial fluorine gasification
within the oxidizer orifices, although a small portion of the ΔP increase
may arise from lower C_D values at 50-psia chamber pressure than those at
100 and 200 psia.
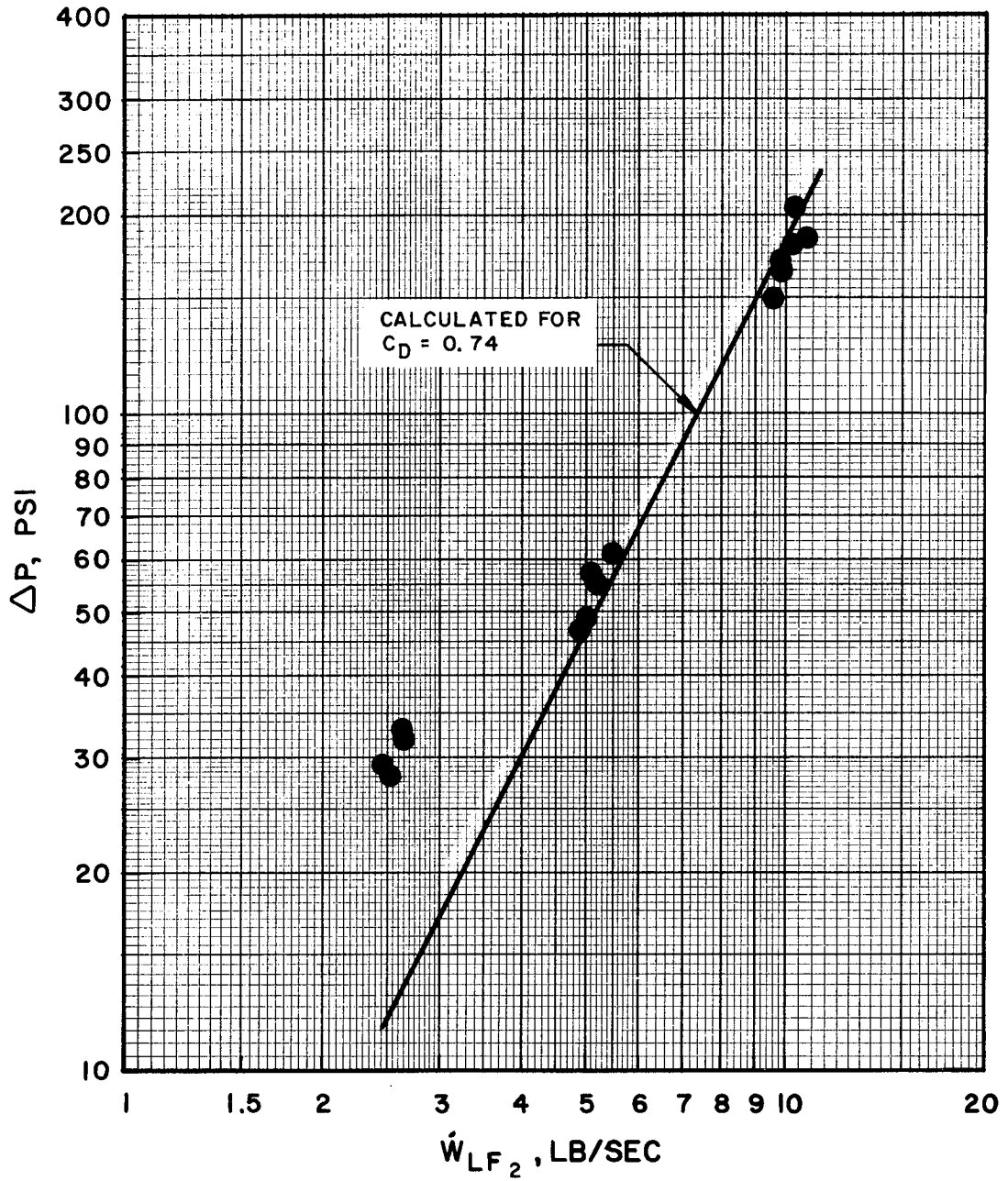
Figure B-1. Experimental Fluorine-Side Pressure Drops, Triplet Injector.
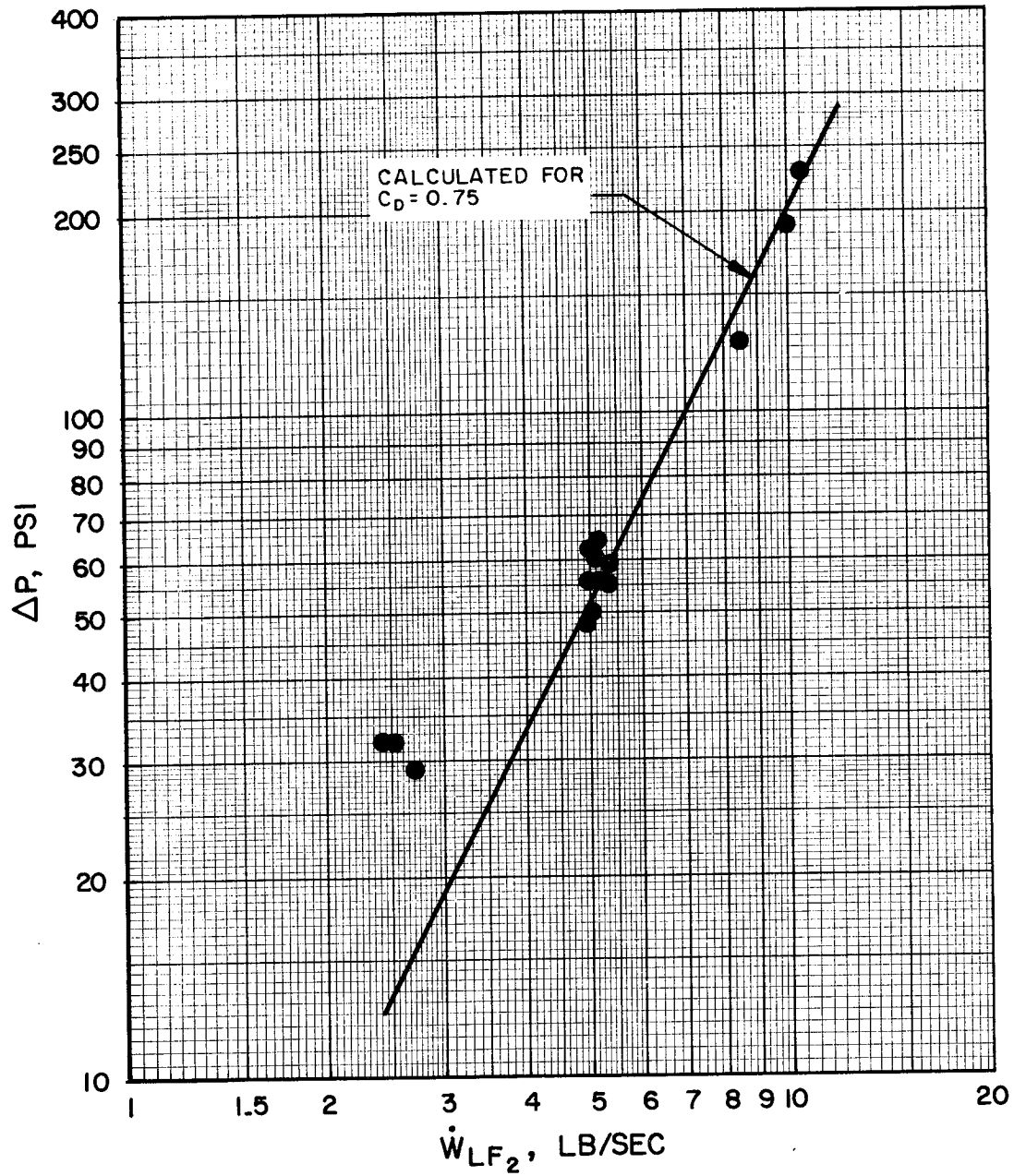
Figure B-2. Experimental Fluorine-Side Pressure Drops, Doublet/Showerhead Injector.

Hydrogen

Fuel orifice characteristics of both injectors are given in Table B-3.

TABLE B-3

HYDROGEN ORIFICE CHARACTERISTICS

Injector	Number of Hydrogen Orifices	Diameter, inches	Total Injection Area, sq in.
Triplet	64	0.1093	0.6013
Doublet/Showerhead	99	0.089	0.6159

Hydrogen flowrate is given by:

$$\dot{w} = \rho A V = \frac{PAV}{RT}$$

$$= \frac{PAV}{\sqrt{\gamma g_c RT}} \sqrt{\frac{\gamma g_c}{R}} \sqrt{\frac{T_o}{T}} \frac{1}{T_o}$$

$$= \frac{PAM}{\sqrt{T_o}} \sqrt{\frac{\gamma g_c}{R}} \sqrt{1 + \frac{\gamma - 1}{2} M^2} \qquad (B-1)$$

where

$\dot{w}$ = hydrogen flowrate, lbm/sec

ρ = hydrogen density at orifice exit, lbm/ft^3

A = orifice exit area, ft^2

V = hydrogen velocity at orifice exit, ft/sec

P = hydrogen static pressure at orifice exit (assumed equal to stagnation chamber pressure), lbf/ft^2

R = hydrogen gas constant = 766.5 ft-lbf/lbm-R

γ = hydrogen specific heat ratio = 1.40

g_c = conversion factor = 32.174 lbm-ft/lbf-sec^2

T = hydrogen static temperature at orifice exit, R

T_0 = hydrogen stagnation temperature, R

M = hydrogen Mach number at orifice exit

Equation B-1 may be written in the form:

$$\dot{w} = \frac{PA}{\sqrt{T_0}} \left[g(M) \right] \qquad (B-2)$$

where

$$g(M) = M \sqrt{\frac{\gamma g_c}{R}} \sqrt{1 + \frac{\gamma - 1}{2} M^2} \qquad (B-3)$$

Hydrogen injection Mach number for specified flowrate, stagnation temperature, injection area, and chamber pressure may be determined by use of the curve of g (M) against M (Fig. B-3).

Nominal hydrogen flowrates, injection Mach numbers, and injector pressure drops are listed in Table B-4. Experimentally observed pressure drops (hydrogen manifold to combustion chamber) are plotted in Fig. B-4 (triplet injector) and B-5 (doublet/showerhead injector).
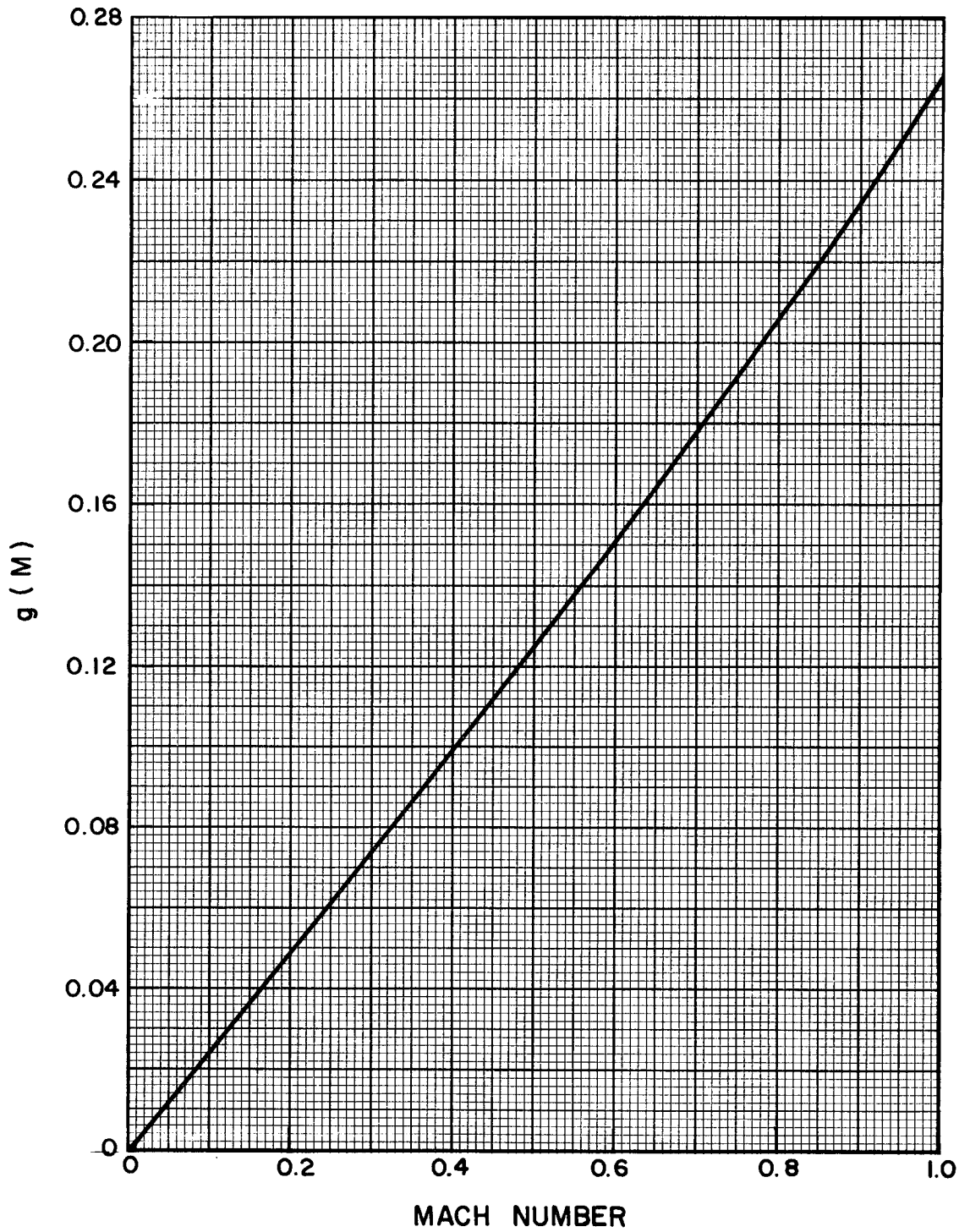
Figure B-3. Variation of the Function g(M), Equation B-3, with Mach Number, for Hydrogen.

TABLE B-4

NOMINAL HYDROGEN FLOWRATES, INJECTION MACH NUMBERS

AND INJECTOR PRESSURE DROPS

Pc, psia	M.R.	$\dot{w}$, lb/sec	Triplet		Doublet/Showerhead	
			M	ΔP, psi	M	ΔP, psi
50	9	0.283	0.85	30	0.83	29
	12	0.222	0.68	18	0.66	17
	15	0.185	0.57	12	0.56	12
100	9	0.563	0.84	59	0.82	57
	12	0.441	0.67	35	0.66	34
	15	0.366	0.56	24	0.56	24
200	9	1.115	0.83	114	0.82	112
	12	0.874	0.67	68	0.65	66
	15	0.724	0.56	47	0.55	46
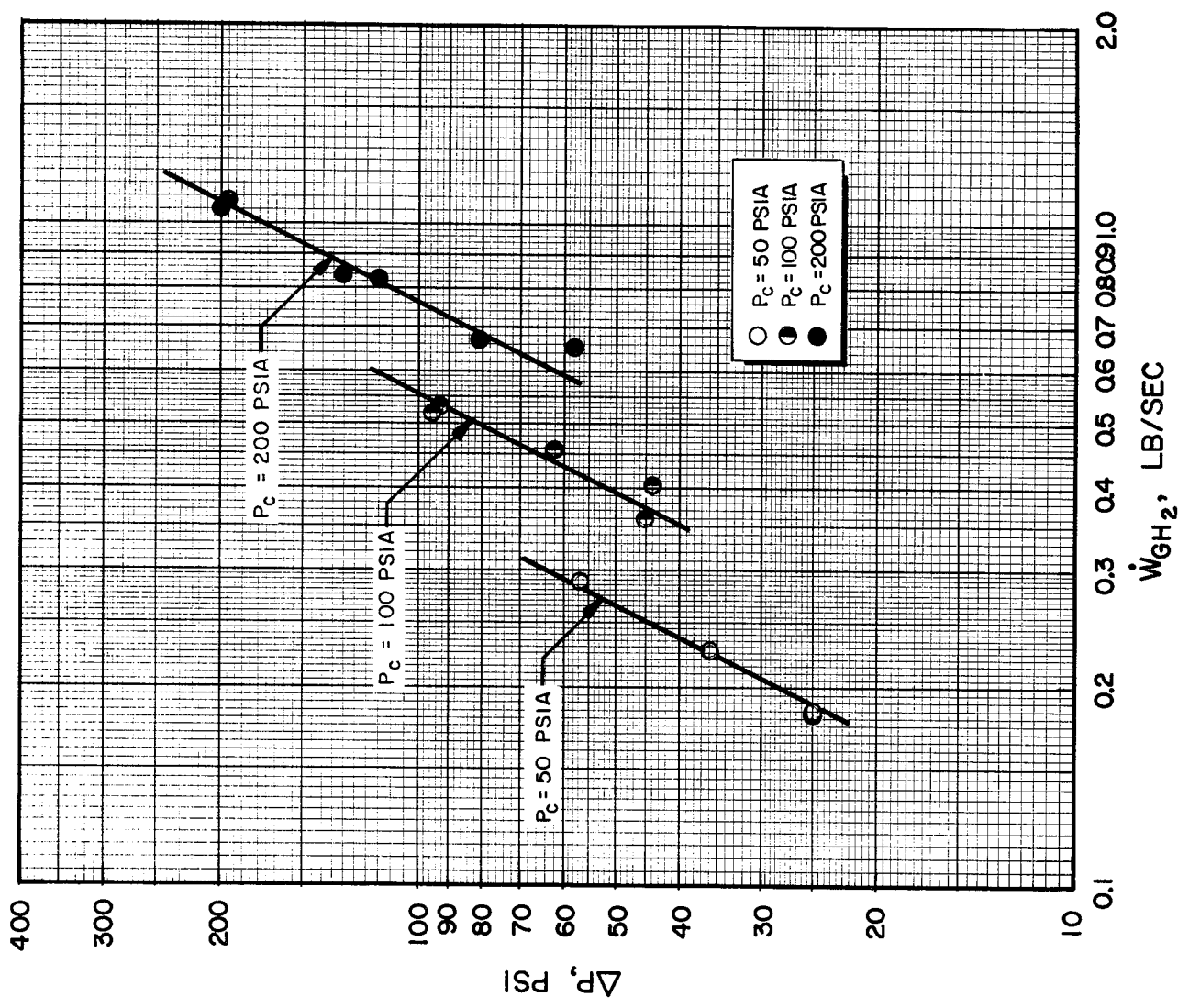
Figure B-4. Experimental Hydrogen-Side Pressure Drops, Triplet Injector.

125
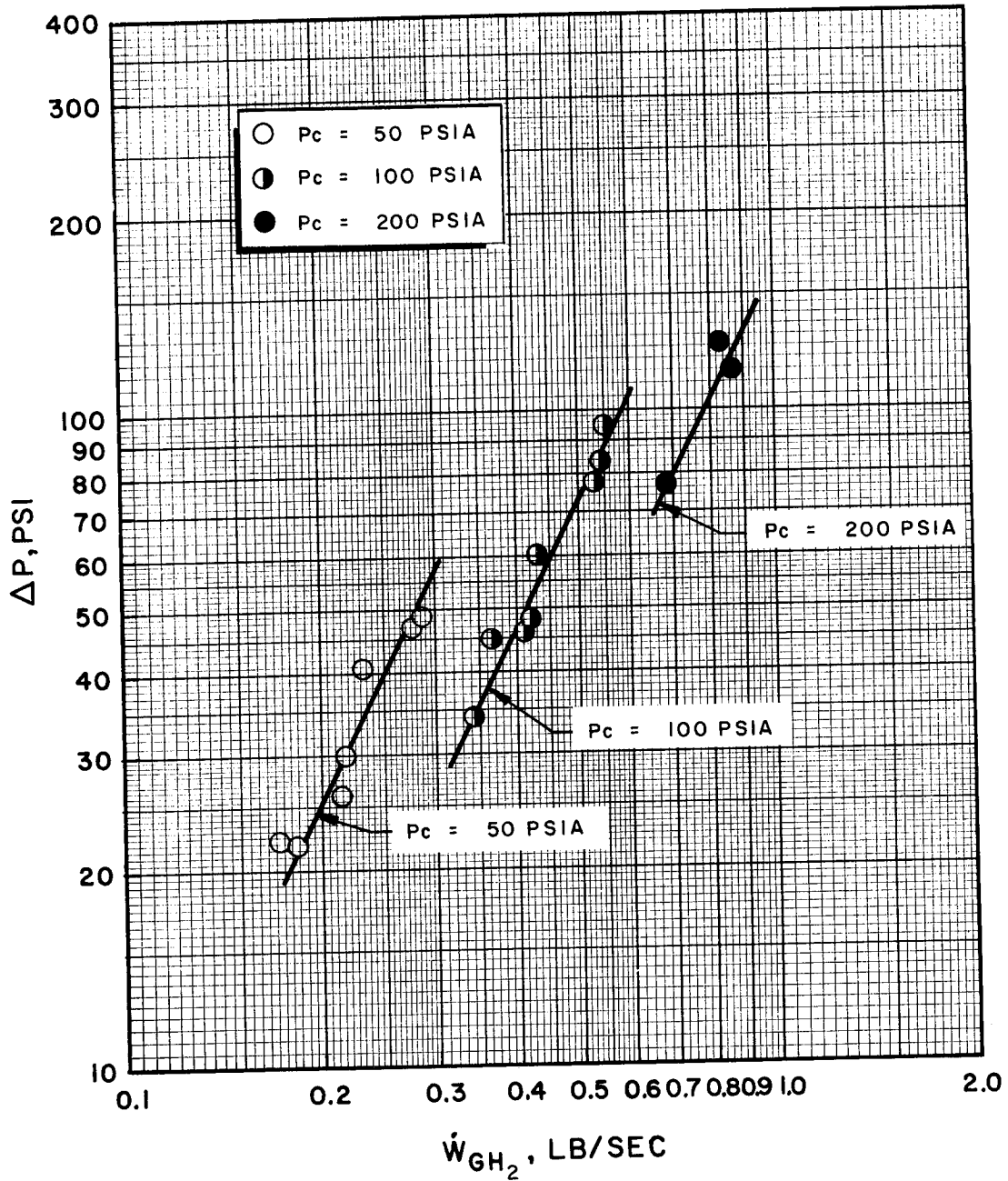
Figure B-5. Experimental Hydrogen-Side Pressure Drops, Doublet/
Showerhead Injector.

APPENDIX C

MEASUREMENT ANALYSIS PROGRAM

INTRODUCTION

The primary purpose of a measurement analysis program is to provide a
function which relates observed sensor outputs to estimates of corre-
sponding system inputs, together with quantitative indications of the
precision of this conversion. The function and the precision estimates
are established on the basis of sensor calibration history, that is, upon
a sequence of periodic calibrations of the sensor and its associated meas-
uring and recording system against known inputs.

Because calibrations must of necessity be made at a time differing from
the actual firing time by several hours to several days, the changes in
random sensor error with time must be established. In the Random Walk
measurement analysis program (Ref. C-1) this is accomplished by assuming
that the input-output ratio at a particular input level performs a random
walk in time which has normal distribution and variance. It assumes also
that there is a random measurement error in the observed datum which is
independent of the random walk and which is also normally distributed.
Mathematical foundations and development of the program are given in
Ref. C-2 and C-3.

On the basis of the sequence of periodic calibrations, the Random Walk
program provides the following:

1. A function, either linear or cubic, which converts observed
   system outputs into estimates of true system inputs;

2. Coefficients of short-term and random walk variations, as well
   as a combined value valid at specified times; and

3. A decision, based upon the calculated coefficient of variation
   and a prespecified imprecision limit, as to whether the sensor
   should be used as is, recalibrated immediately, or discarded,
   and the maximum allowable interval to next calibration.

MEASUREMENT PROGRAM OUTPUT

A typical Random Walk computer program output is shown in Table C-1. The
first line of output gives the test stand name and number (Yoke, 0018),
recording system (Beckman), transducer serial number (1641002), range
(200 psi), ID number for data cards (018049), and the physical parameter
being calibrated $(P_c - 1A)$.

The next set of numbers ("Latest Output") is the most recent raw calibra-
tion data. On the left are the readings (in Beckman counts) for the
listed calibration input steps ("Input"); on the right are the precalibrate
throw zero (Z1), the calibrate throw reading (CT), the postthrow zero (Z2),
the precalibration zero (Z3), the postcalibration zero (Z4), and the date
of calibration ("Time").

The first two zeros (Z1 and Z2) are averaged and subtracted from the throw
to get a reduced throw. For each calibration step, a linear interpolation
is made between the last two zeros (Z3 and Z4) and the interpolated result
is subtracted from the reading to get a reduced reading. Each reduced
reading is then divided by the reduced throw to get a scaled output. All
scaled output values from all calibrations in the system history are then
listed ("Scaled Output") under the appropriate input pressures, with one
calibration per line and its date ("Time") at the right of each line.

```
*          YOKE  0018           BKM    1641002

*  LATEST OUTPUT
*
*     364      789     1103     1633     2162

*  INPUT

*      30       7C      100      150      200

*  SCALED OUTPUT
*
*  0.1577   C.3706   0.5278   0.7932   1.0581
*  C.1577   0.3689   0.5265   0.7929   1.0572
*  0.1567   0.3704   0.5280   0.7923   1.0566
*  0.1556   0.3682   0.5283   0.7919   1.0565
*  0.1551   0.3692   0.5283   0.7924   1.0580
*  0.1570   C.3701   0.5276   0.7927   1.0578

*  MEASUREMENT VARIANCE IN INPUT-TO-SCALED C
*  RANDOM WALK VARIANCE IN INPUT-TO-SCALED 0
*  RATIC OF SHORT-TERM VARIANCE TO RANDOM WA
*  COEFFICIENT OF SHORT-TERM VARIATION
*  COEFFICIENT OF RANDOM WALK VARIATION
*  REQUIREMENT FOR COEFFICIENT OF VARIATION

*  SYSTEM NOW PASSES TEST FOR LINEARITY (TYP
*  DATA REDUCTION FORMULA IS

*                  (INPUT) = (1.8920E 02)*(

*  ABCVE OUTPUT-INPUT MODEL IS SATISFACTORY

*  SYSTEM SHOULD BE CALIBRATED CN OR BEFORE
*                               COEF
*                               COEF

*  DATA REDUCTION MATRIX          ( 2.40921E
*                                 (
*                                 ( 0.
```

The first three lines following the scaled output table are estimates of the measurement variance $(\sigma_m^{\,2})$ in the input/scaled output ratio, the random walk variance (σ^2) in the input/scaled output ratio, and the ratio (k) of the former (short-term) variance to the latter (long-term) variance. The variances $(\sigma_m^{\,2}$ and $\sigma^2)$ are used in computing the data reduction imprecision, which is defined as the standard deviation of an estimated input about the true input.

The next line of output gives the coefficient of short-term variation, which is the standard deviation (σ_m) expressed as a percentage of the average input/scaled output ratio. This quantity is generally the largest component of data reduction imprecision. The following entry gives the coefficient of random walk (long-term) variation, which is the standard deviation (σ) also expressed as a percentage of the average input/scaled output ratio. This item is meaningful only after calibrations are obtained over a period of time. The final listing in this block is the prespecified maximum limit of data reduction imprecision expressed as coefficient of variation.

The program now calculates revised scaled output values corresponding to the state of the system at the time of the most recent calibration. These values are then fit by least squares with either a linear or cubic function by the following procedure. The null hypothesis is that the function is linear, and the specified error (the probability that a truly linear function is mistakenly concluded to be nonlinear) is printed out. If the linearity hypothesis is rejected, a cubic fit is made. In either case, the formula for converting scaled outputs to estimated inputs is then given, and, if the relationship is cubic, an input-output table is printed out for convenience in data reduction.

UCER CALIBRATIONS USING RANDOM WALK

LYSIS PROGRAM

	018049			PC1A			
		$Z1$	CT	$Z2$	$Z3$	$Z4$	TIME
		49	2046	49	49	49	8-20-65

TIME

8-20-65
8-13-65
7-27-65
7-27-65
7-27-65
7-27-65

PUT RATIO	=	0.28773E-00	
PUT RATIO	=	0.23358E-01	
VARIANCE	=	0.12318E 02	(DAYS)
	=	0.283	(PERCENT)
	=	0.0806	(PERCENT/DAY**.5)
REDUCED DATA	=	1.500	(PERCENT)

I ERROR=.05).

ALED OUTPUT)

YPE I ERROR=.05).

-19-65
CIENT OF VARIATION OF REDUCED DATA ON 9-19-65 = 0.53 PERCENT
CIENT OF VARIATION OF REDUCED DATA ON 8-22-65 = 0.32 PERCENT

2   0.   )
)
       0.   )

129-2

The next line gives the result of the second test, which checks whether or not the input-output model is consistent with the estimate of σ_m (the root-mean-square estimate for the calibration curve fit and σ_m should be approximately equal). If it is, then the model is labeled "SATISFACTORY"; if not, the model is labeled "UNSATISFACTORY," indicating a significant intercept or an error in the input data, for $k \neq 0$ (when $k = 0$, this test is not applicable).

The following item indicates the ability of the system to meet the specified imprecision requirement. On the basis of the calibration data, three situations are recognized:

1. The system can never meet required precision, and should be replaced;

2. The system will fail the requirement within the next two days and should be recalibrated immediately; or

3. The system will meet the requirement up to a certain date (30 days maximum), on or before which it should be recalibrated. In this case, the estimated data reduction imprecision is given for test data taken two days after the most recent calibration and on the specified recalibration date.

In the present program, the system transducers were calibrated within one or two days prior to each series of firings, regardless of the leeway allowed by reason of little or no random walk variation and consequent minimum degradation in precision.

The final item is a 2 by 2 matrix, denoted by R, which is used to estimate data reduction imprecision at any other time of interest and for any scaled output by the following expression:

$$P = \left[V + s^2 (h\,\sigma^2 + \sigma_m^2) \right]^{1/2}$$

where

P = estimated standard deviation for a reduced datum

s = scaled output

h = number of days after most recent calibration

V = matrix product: $(s, s^3)\, R \begin{pmatrix} s \\ s^3 \end{pmatrix}$

Application of the results of the measurement analysis program to estimation of random experimental errors and to measurement reliability is given in Appendix E.

REFERENCES

C-1. Rothman, D.: <u>Random Walk Program for Measurements Analysis of Static Systems</u>, RM-1119-351, Rocketdyne, a Division of North American Aviation, Inc., Canoga Park, California, 25 January 1965.

C-2. Rothman, D.: <u>A Random Walk Model for Non-Uniform, One-Parameter, Static, Linear Measurement Systems</u>, RR-59-47, Rocketdyne, a Division of North American Aviation, Inc., Canoga Park, California, 15 December 1959.

C-3. Rothman, D.: <u>Gaussian Random Walk with Gaussian Measurement Errors</u>, SORUM-63-9, Rocketdyne, a Division of North American Aviation, Inc., Canoga Park, California, 24 September 1963.

APPENDIX D

CALCULATION OF CORRECTED c* EFFICIENCY

INTRODUCTION

The index of injector performance used in the present experimental program was corrected c* efficiency. This parameter was calculated by two independent methods, one based on measurement of chamber pressure and the other on measurement of thrust. Details of the computational procedures and of the corrections applied are given in this appendix.

CALCULATIONS BASED ON CHAMBER PRESSURE

Characteristic velocity efficiency based on chamber pressure is defined by the following equation:

$$\eta_{c*} = \frac{(P_c)_0 \, (A_t)_{eff} \, g_c}{(\dot{w}_T) \, (c^*)_{theo}} \qquad (D-1)$$

where

$(P_c)_0$ = stagnation pressure at the throat

$(A_t)_{eff}$ = effective thermodynamic throat area

g_c = conversion factor ($32.174 \; lbm\text{-}ft/lbf\text{-}sec^2$)

$\dot{w}_T$ = total propellant weight flowrate

$(c^*)_{theo}$ = theoretical characteristic velocity based on shifting equilibrium

Values calculated from Eq. D-1 are referred to as "corrected" c* effici-
encies, because the factors involved are not measured directly, but are
obtained by application of suitable corrections to measured parameters.
Thus, stagnation pressure at the throat is obtained from measured static
pressure at start of nozzle convergence by assumption of isentropic expan-
sion, effective throat area is estimated from measured geometric area by
allowing for radius changes during firing and for nonunity discharge
coefficient, and chamber pressure is corrected to allow for energy losses
from combustion gases to the chamber wall by heat transfer and friction.
Equation D-1 may therefore be written as follows:

$$\eta_{c*} = \frac{P_c \, A_t \, g_c \, f_P \, f_{TR} \, f_{DIS} \, f_{FR} \, f_{HL}}{(\dot{w}_0 + \dot{w}_f) \, (c*)_{theo}} \qquad (D-2)$$

where

P_c = measured static pressure at start of nozzle convergence, psia

A_t = measured geometric throat area, in.^{2}

g_c = conversion factor $(32.174 \text{ lbm-ft/lbf-sec}^2)$

$\dot{w}_0$ = oxidizer weight flowrate, lb/sec

$\dot{w}_f$ = fuel weight flowrate, lb/sec

$(c*)_{theo}$ = theoretical c* based on shifting equilibrium calculations, ft/sec

f_P = factor correcting observed static pressure to throat stagnation pressure

f_{TR} = factor correcting for change in throat radius during firing

f_{DIS} = factor correcting throat area for effective discharge coefficient

f_{FR} = factor correcting measured chamber pressure for frictional drag of combustion gases at chamber wall

f_{HL} = factor correcting measured chamber pressure for heat losses from combustion gases to chamber wall.

Methods of estimation of the various correction factors are described in the following paragraphs.

Pressure Correction $\left(f_{P}\right)$

Measured static pressure at start of nozzle convergence was converted to stagnation pressure at the throat by assumption of no combustion in the nozzle and application of the isentropic flow equations, with contraction ratio $\left(A_{c}/A_{t}\right)$ of 2.05. Shifting-equilibrium specific heat ratio $\left(\gamma\right)$ ranged from 1.15 (at chamber pressure = 50 psia, mixture ratio = 15) to 1.18 (at chamber pressure = 200 psia, mixture ratio = 9). The corresponding stagnation/static pressure ratios were not significantly different: 1.055 and 1.056, respectively. The same correction factor was therefore applicable over the entire experimental chamber pressure/mixture ratio matrix, i.e., f_{P} = 1.055. Had frozen-equilibrium specific heat ratios been used, the correction factor would have been about 1/2 percent larger. Hence the value employed was the more conservative.

Throat Radius Correction $\left(f_{TR}\right)$

Temperature gradients produced in an uncooled nozzle wall by flow of hot combustion gases result in thermal stresses which affect throat radius. Consequently, the geometric throat diameter measured in an ambient-temperature nozzle is not the same as that which exists during firing.

When firing begins, thermal penetration of the nozzle wall is small with respect to the wall thickness, hence the outer wall diameter is unchanged. The inner wall material will therefore expand toward the center, resulting in a decrease in throat diameter. As heat penetrates throughout the nozzle wall, the outer diameter will also increase, allowing outward expansion of the inner portion and consequent increase in throat diameter. Manifestly, throat diameter during firing is a function of time, as well as of the physical properties of the throat material and the temperature and pressure of the combustion gases.

A Rocketdyne computer program is available which estimates the change in throat radius as a function of time (Ref. D-1). The computation is based on numerical integration of the transient thermal stress equations for a hollow cylinder (Ref. D-2). A cubic temperature distribution is assumed in the wall, plastic as well as elastic strain in the wall material is considered, and allowance is made for stress caused by gas pressure. Average values of measured convective film coefficients at the throat and gas temperatures based on 98-percent combustion efficiency were used for program input.

Results of the calculations are presented in Fig. D-1, which indicates the change in geometric throat radius as a function of firing time. The differences in the values at each of the three nominal chamber pressures are not primarily due to pressure effects as such, which are minor, but rather to the corresponding variations in convective film coefficients.

Throat Discharge Coefficient Correction (f_{DIS})

The discharge coefficient is defined as the ratio of actual flowrate through the throat to the theoretical maximum based on geometric throat area and ideal, uniform, one-dimensional flow with no boundary layer.
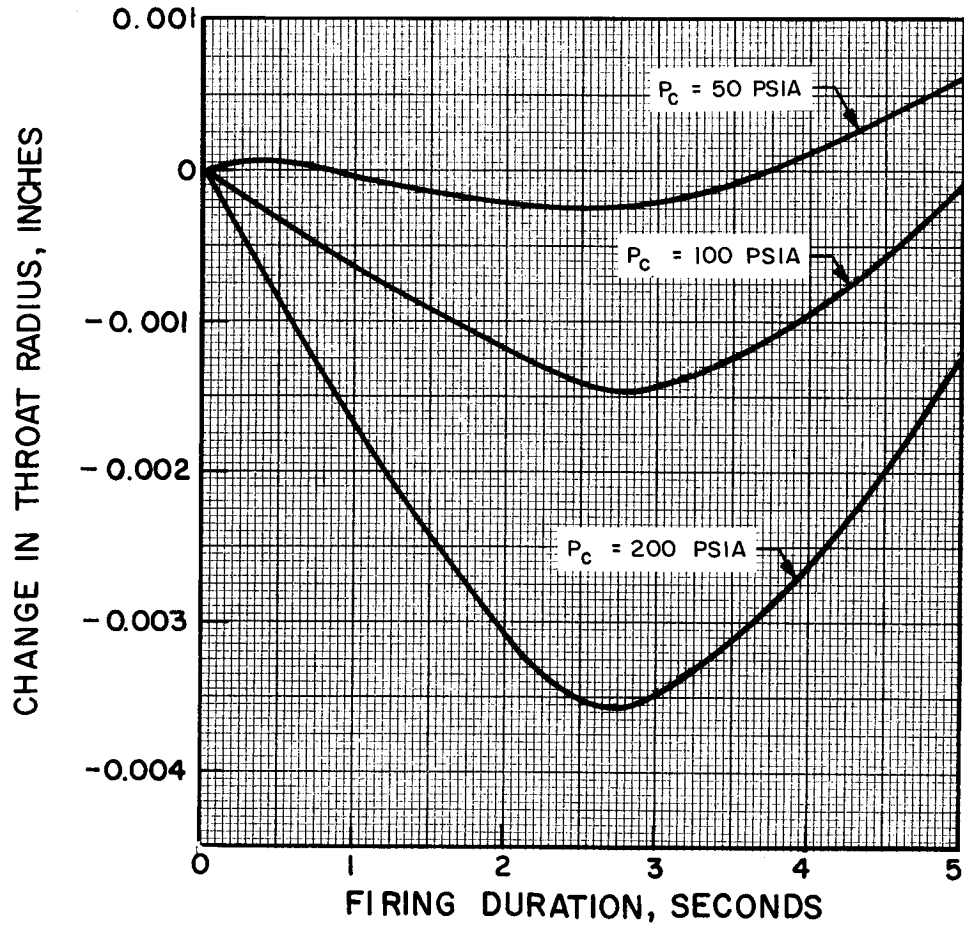
Figure D-1. Change in Throat Radius as Function of Firing
Duration, for LF_2/GH_2 in Thrust Chamber Shown
in Figure 7, at Indicated Chamber Pressures
and Mixture Ratio of 12.

Values of the discharge coefficient were estimated in two ways: one based on calculations made from a theoretical, inviscid flow model of F_2/H_2 combustion products, and the other based on a correlation of results obtained in various experimental studies of air flow through nozzles.

Theoretical Model. Total mass flowrate is given by

$$\dot{m} = \int_0^A \rho\, V\, dA \tag{D-3}$$

where

ρ = gas density

V = gas velocity

A = cross-sectional area

Theoretical maximum flowrate at the throat is

$$\dot{m}_{max} = \int_0^{A_t} \rho^*\, V^*\, dA \tag{D-4}$$

where

A_t = geometric area of the throat

ρ^* = sonic gas density

V^* = sonic gas velocity

For ideal, uniform, parallel flow, Eq. D-4 becomes

$$\dot{m}_{max} = \rho^*\, V^*\, A_t \tag{D-5}$$

The discharge coefficient is then

$$C_D = \frac{\dot{m}}{\dot{m}_{max}} = \int_0^A \left(\frac{\rho}{\rho^*}\right)\left(\frac{V}{V^*}\right)\left(\frac{dA}{A_t}\right) \qquad (D-6)$$

The numerical value obtained from Eq. D-6 by use of the results of transonic flow analyses made for F_2/H_2 in the experimental chamber is

$$C_D = f_{DIS} = 0.994$$

Empirical Value. Experimental conical nozzle discharge coefficients obtained with air by various investigators are plotted in Fig. D-2 against the indicated geometric parameter. Data sources also are listed in Fig. D-2.

Based upon the correlating curve shown and the nozzle geometry of the thrust chamber used in the present studies, the throat discharge coefficient correction factor is: $f_{DIS} = 0.992.$

The values obtained by both methods are in excellent agreement; an average of the two was used in the c* calculations: $f_{DIS} = 0.993.$

Frictional Drag Correction $\left(f_{FR}\right)$

Calculations of c* based on chamber pressure are concerned with chamber phenomena up to the nozzle throat. Drag forces to this point are small enough to be considered negligible, so that the factor f_{FR} was taken to be unity.
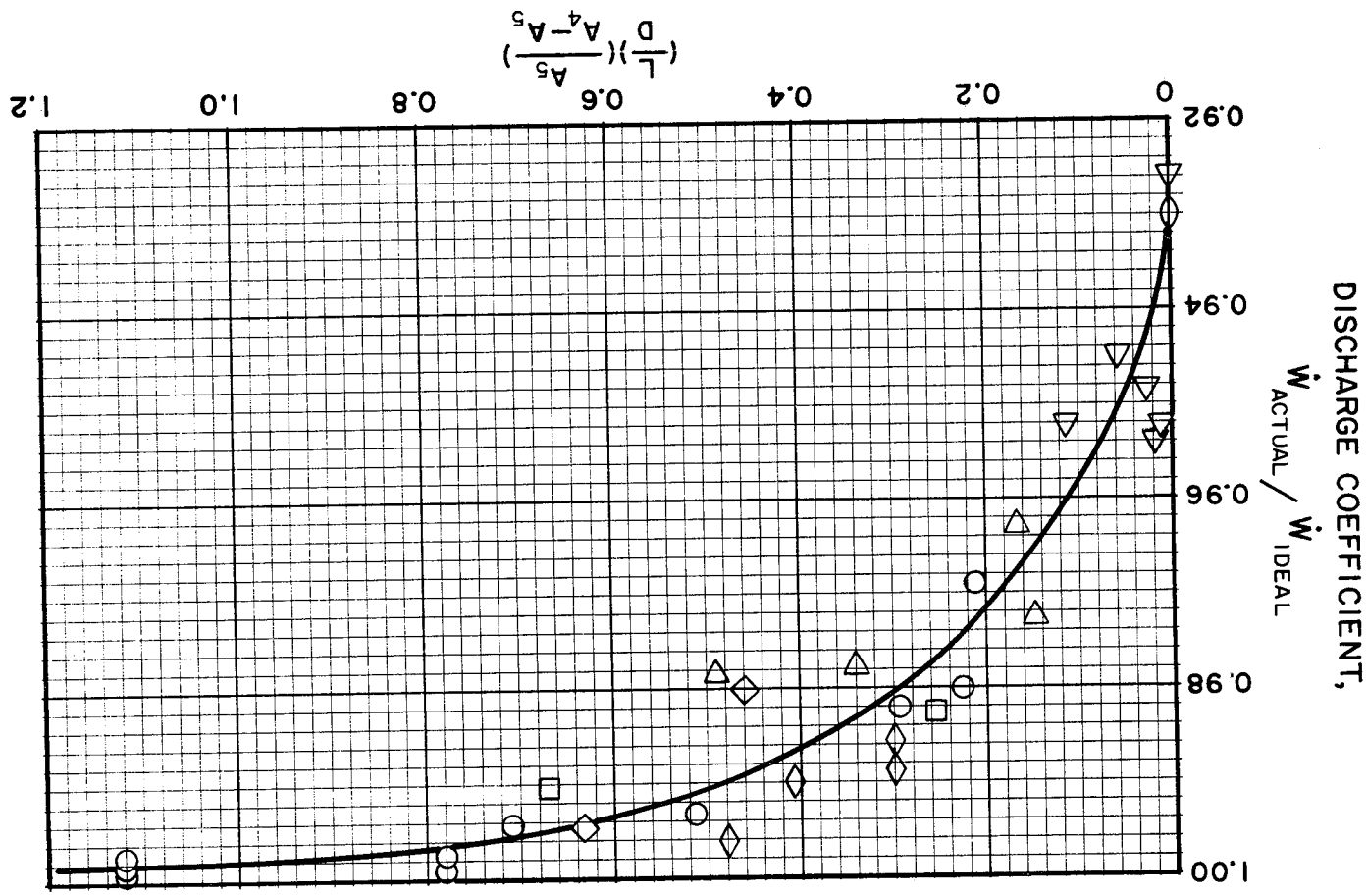
Figure D-2. Discharge Coefficient as Function of Nozzle Dimensions (A_4 = Cross-Sectional Area of Chamber, A_5 = Cross-Sectional Area of Throat).
Data Taken from Indicated References, for Cold Flows with Air.

DISCHARGE COEFFICIENT, $\dot{W}_{ACTUAL} / \dot{W}_{IDEAL}$

$(\frac{L}{D})(\frac{A_5}{A_4 - A_5})$
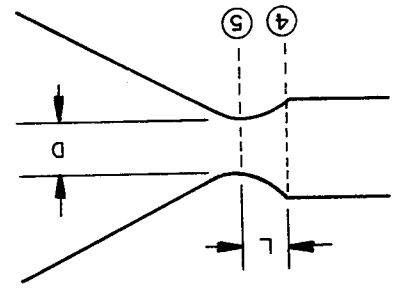
Legend:
- ◻ CONVAIR REPORT TB-62
- ◇ CONVAIR REPORT TB-71
- ▽ A.S.M.E. PAPER 50-A-64
- ○ MARQUARDT REPORT 5162
- ◊ N.A.C.A REPORT TR-933
- △ U.S.C. REPORT PR-9961-3
- ◇ A.S.M.E. CALIB. NOZZLE

ROCKETDYNE • A DIVISION OF NORTH AMERICAN AVIATION, INC.

Heat Loss Correction (f_{HL})

Heat transfer from the combustion gases to the walls of an uncooled thrust chamber results in loss of enthalpy and thus decreases chamber pressure and thrust. This enthalpy loss is substantially reduced in an ablative chamber and is effectively recovered in a chamber cooled regeneratively by one of the propellants, whose initial enthalpy is raised by the heat absorbed. To obtain a true indication of performance efficiency in an uncooled chamber, measured chamber pressure must be corrected by a factor which accounts for heat loss to the walls. Heat transfer to the injector was neglected in this correction because the injector surface area was small relative to that of the chamber and because a portion of injector heat flux was absorbed by the injected propellants.

The effect on c* of enthalpy loss by heat transfer was estimated by assuming that heat loss in the converging portion of the nozzle was negligible compared to that in the combustion chamber. Experimental data indicate this to be a reasonably valid assumption. Loss of chamber enthalpy is reflected in decreased chamber temperature, and may be estimated from an energy balance between two stations, one at the start of nozzle convergence and the other at the throat:

$$1/2 \ V_c^{\ 2} + H_c = 1/2 \ V_t^{\ 2} + H_t \tag{D-7}$$

where

V_c = gas velocity at chamber exit

V_t = gas velocity at nozzle throat

H_c = gas enthalpy at chamber exit

H_t = gas enthalpy at nozzle throat

Velocity at the throat is given by

$$V_t = \left[V_c^2 + 2\left(H_c - H_t\right) \right]^{1/2} \tag{D-8}$$

By conservation of mass,

$$V_c = V_t \left(\frac{\rho_t A_t}{\rho_c A_c} \right) \tag{D-9}$$

whence

$$V_t = \left[\frac{2\left(H_c - H_t\right)}{1 - \left(\rho_t A_t / \rho_c A_c\right)^2} \right]^{1/2} \tag{D-10}$$

If the velocity at the nozzle inlet were low enough to be neglected, Eq. D-8 would reduce to

$$V_t = \left[2\left(H_c - H_t\right) \right]^{1/2} \tag{D-11}$$

Comparison of Eq. D-10 and D-11 indicates that the factor, Z, accounting for the effect of initial velocity, V_c, is

$$Z = \left[\frac{1}{1 - \left(\rho_t A_t / \rho_c A_c\right)^2} \right]^{1/2} \tag{D-12}$$

Enthalpy loss in the chamber has a negligible effect upon the magnitude of this factor, so Z is constant. Logarithmic differentiation of Eq. D-10 after substitution of Eq. D-12 gives:

$$\frac{dV_t}{V_t} = 1/2 \frac{d\left(H_c - H_t\right)}{\left(H_c - H_t\right)} = 1/2 \left(\frac{d\,H_c - dH_t}{H_c - H_t} \right) \tag{D-13}$$

142

Substitution of $dH = c_p \, dT$ into Eq. D-13 gives:

$$\frac{dV_t}{V_t} = 1/2 \left(\frac{c_{pc} \, dT_c - c_{pt} \, dT_t}{H_c - H_t} \right) \tag{D-14}$$

If c_p is constant between the two stations, this may be written:

$$\frac{dV_t}{V_t} = 1/2 \left(\frac{c_p \, dT_c}{H_c - H_t} \right) \left(\frac{1 - dT_t}{dT_c} \right) \tag{D-15}$$

If the specific heat ratio, γ, is assumed constant,

$$\frac{dT_t}{dT_c} = \frac{T_t}{T_c} \tag{D-16}$$

Substituting Eq. D-16 into Eq. D-15, replacing differentials by incrementals, and noting that c* is proportional to gas velocity at the throat gives:

$$\frac{\Delta V_t}{V_t} = \frac{\Delta c^*}{c^*} = 1/2 \left(\frac{c_p \, \Delta T_c}{H_c - H_t} \right) \left(1 - \frac{T_t}{T_c} \right) \tag{D-17}$$

Total heat loss to the chamber walls, in Btu per pound of propellant, is obtained by summation of observed heat fluxes over the appropriate areas:

$$\text{Heat loss} = \frac{\Sigma \, (q/A)A}{\dot{w}_T} \tag{D-18}$$

where

q/A = experimentally observed heat flux

A = area applicable to each q/A value

$\dot{w}_T$ = total propellant flowrate

If this heat loss is equated to the change in enthalpy of the gas in the combustion chamber, $c_p \Delta T_c$, then substitution into Eq. D-17 gives:

$$\frac{\Delta c^*}{c^*} = 1/2 \left[\frac{\Sigma (q/A)A}{\dot{w}_t} \right] \left[\frac{1 - (T_t/T_c)}{H_c - H_t} \right] \qquad (D-19)$$

Throat stagnation pressures, used in computing experimental c^* values, were obtained from static pressures measured at the start of nozzle convergence by assumption of isentropic flow in the convergent section. Hence, only heat losses to the chamber wall between the injector and the start of nozzle convergence were included in Eq. D-19. The applicable correction factor is:

$$f_{HL} = 1 + \frac{\Delta c^*}{c^*} = 1 + 1/2 \left[\frac{\Sigma (q/A)A}{\dot{w}_T} \right] \left[\frac{1 - (T_t/T_c)}{H_c - H_t} \right] \qquad (D-20)$$

An alternate expression for the heat loss correction factor is the following (Ref. D-3):

$$f_{HL} = \left\{ 1 + \left[\frac{c^*_{theo}}{c^*_{meas}} \right]^2 \left[\frac{\Sigma (q/A)A}{\dot{w}_T c_{p_m} T_c} \right] \right\}^{1/2} \qquad (D-21)$$

where

c^*_{theo}	=	theoretical characteristic velocity at test conditions, based on full shifting equilibrium
c^*_{meas}	=	measured characteristic velocity
$\Sigma(q/A)A$	=	observed heat flux to chamber walls
$\dot{w}_t$	=	total propellant flowrate
c_{p_m}	=	mean specific heat of combustion chamber gases
T_c	=	theoretical chamber temperature at test conditions

Equations D-20 and D-21 can be shown to be equivalent by introduction of the following relationship, which is valid for frozen flow:

$$H_m = c_{p_m} T_c \tag{D-22}$$

where H_m is the mean enthalpy of chamber combustion gases. Substitution of Eq. D-22 into Eq. D-20 gives:

$$f_{HL} = 1 + 1/2 \left[\frac{\Sigma (q/A)A}{\dot{w}_T} \right] \left[\frac{T_c - T_t}{T_c (c_{p_m} T_c - c_{p_m} T_t)} \right]$$

or

$$f_{HL} = 1 + 1/2 \left[\frac{\Sigma (q/A)A}{\dot{w}_T \, c_{p_m} T_c} \right] \tag{D-23}$$

Equation D-21 may be reduced to Eq. D-23 by making a series expansion of the former and neglecting all terms higher than the second as well as the second-order effect of performance efficiency $\left(c^*_{theo} / c^*_{meas} \right)$.

Equations D-20 and D-21 provide essentially identical values of the heat loss correction factor if the difference between frozen and shifting performance is small, as is the case for such propellant combinations as N_2O_4/N_2H_4 and IRFNA/UDMH. For F_2/H_2, however, the difference is large, and values of f_{HL} computed from Eq. D-20 are significantly smaller at $L^* = 30$ inches, than those obtained from Eq. D-21. Which of the two should be used depends upon whether frozen or shifting combustion gas specific heat values are employed; the former apply to Eq. D-21, and the latter to Eq. D-20.

The principal differences between the heat loss correction methods represented by Eq. D-20 and D-21 may be stated as follows:

1. Application of Eq. D-20 implicitly assumes that heat transferred to the wall instantaneously affects the bulk gas stream, whose temperature is thus reduced. This temperature reduction, in turn, produces some recombination, which adds heat to the bulk stream, thus lessening the effect of heat loss to the chamber walls on performance.

2. Application of Eq. D-21 assumes that the bulk gas is not affected by heat loss to the walls and so no heat of recombination is added to the bulk stream. Hence, the total heat loss, instead of only part of it, reduces performance efficiency.

Because no realistic choice can be made between the two equations as applied to F_2/H_2 combustion, the values of f_{HL} actually used were obtained by taking an average of the estimates made on the basis of the two assumptions: (1) heat loss comes from the bulk of the gas which remains in equilibrium, and (2) heat loss comes from a stratified layer at the chamber wall. The latter was calculated by Eq. D-21. For the former, the factor was calculated in the form of modified values of theoretical c*, obtained with computer programs which corrected initial combustion chamber enthalpy for observed heat fluxes to the walls in making performance calculations (Ref. D-4). This gives essentially the same values as Eq. D-20, in which the enthalpy differences and the temperature ratios between chamber and throat refer to theoretical performance without heat loss.

Values of the heat loss correction factor calculated by each procedure are listed in Table D-1.

TABLE D-1

TYPICAL HEAT LOSS CORRECTION FACTORS $\left(f_{HL}\right)$

P_c, psia	L*, inches	Heat Loss Correction Factor, f_{HL}	
		By Eq. D-20	By Eq. D-21
50	30	1.008	1.017
100	10	1.002	1.003
	30	1.007	1.013
200	30	1.007	1.012

CALCULATIONS BASED ON THRUST

An alternate determination of corrected c* efficiency is based on the following defining equation:

$$\eta_{c*} = \frac{F_{vac}\, g_c}{\left(C_F\right)_{vac}\, \dot{w}_T\, c^*_{theo}} \tag{D-24}$$

where

F_{vac} = measured thrust corrected to vacuum conditions by the equation: $F_{vac} = F + P_a A_e$

F = measured thrust, lbf

P_a = ambient pressure, psia

A_e = area of nozzle exit, in.^{2}

g_c = conversion factor $(32.174\ \text{lbm-ft/lbf-sec}^2)$

$\left(C_F\right)_{vac}$ = theoretical shifting thrust coefficient (vacuum)

$\dot{w}_T$ = total propellant flowrate, lbm/sec

c^*_{theo} = theoretical shifting-equilibrium characteristic velocity, ft/sec

By application of suitable corrections to measurements of thrust made at sea level, corrected values of vacuum thrust may be obtained. With these values, which include allowances for all important departures from ideality, theoretical thrust coefficients may be used for calculation of c*. That is, C_F efficiency is 100 percent if there is no combustion in the nozzle, if chemical equilibrium is maintained in the nozzle expansion process, and if energy losses from the combustion gases are accounted for.

Applicable corrections to measured thrust are specified in the following equation:

$$\eta_{c*} = \frac{(F + P_a A_e)\, g_c\ \varphi_{FR}\ \varphi_{DIV}\ \varphi_{HL}}{(C_F)_{theo}\, (\dot{w}_o + \dot{w}_f)\, (c*)_{theo}} \tag{D-25}$$

where

F	=	measured thrust, lbf
P_a	=	ambient pressure, psia
A_e	=	area of nozzle exit, in.^{2}
g_c	=	conversion factor $(32.174\ \text{lbm-ft/lbf-sec}^2)$
$(C_F)_{theo}$	=	theoretical shifting thrust coefficient (vacuum)
$\dot{w}_o$	=	oxidizer weight flowrate, lbm/sec
$\dot{w}_f$	=	fuel weight flowrate, lbm/sec
$(c*)_{theo}$	=	theoretical shifting equilibrium characteristic velocity, ft/sec
φ_{FR}	=	correction for frictional losses
φ_{DIV}	=	correction for nozzle divergence
φ_{HL}	=	correction for heat losses to chamber and nozzle walls

The correction factors in Eq. D-25 were applied to vacuum thrust $\left(F + P_a A_e\right)$ instead of to measured site thrust (F) because, for convenience, the correction factors were calculated as changes in efficiency based on theoretical vacuum parameters, so that the total correction was of the form $\Delta F/F_{vac}$.

Although they do not appear explicitly in Eq. D-25, corrections to geometric throat area and to measured static chamber pressure at start of nozzle convergence are implicit in the use of theoretical C_F values. Thus, calculation of corrected c* efficiency from thrust measurement includes all the corrections described above for calculations from chamber pressure measurement plus an additional one to account for nonparallel nozzle exit flow. However, because $\left(C_F\right)_{theo}$ is essentially independent of the very small changes in chamber pressure and contraction ratio which are involved in corrections to P_c and A_t, these corrections are of no practical significance in calculation of c* from thrust measurements.

Correction for Frictional Drag $\left(\varphi_{FR}\right)$

This factor corrects for the energy losses caused by drag forces resulting from the viscous action of the combustion gases on the thrust chamber walls. Its magnitude, which is the integral of the local friction forces over the chamber inside wall, was estimated by a boundary layer analysis utilizing the integral momentum equation for turbulent flow. This analysis accounts for boundary layer effects from the injector to the nozzle exit by suitable description of the boundary layer profile and local skin friction coefficient. A computer program was used to carry out a numerical integration of the equation, including effects of pressure gradient, heat transfer, and surface roughness. The program required a potential

core solution of the nozzle flow which was obtained from the variable-property, axisymmetric method of characteristics calculation of the flow field outside the boundary layer; corresponding properties for the sub-sonic combustion chamber flow field were also calculated.

Computed values of φ_{FR} in the 30-inch L* chamber were 1.013, 1.012, and 1.011 at chamber pressures of 50, 100, and 200 psia, respectively, with negligible mixture ratio variation in the range of 9 to 15. Correspond-ing calculations for the shorter chambers indicated uniform decreases in φ_{FR} of about 0.002 for both the 10- and 3.4-inch L* chambers. Shorter chamber lengths may exhibit two effects: decrease in drag loss because of lessened wall areas, and increase in loss because of shorter distances available for boundary layer growth, with consequent thinner boundary layers and higher drag losses in the nozzle.

Correction for Nozzle Divergence (φ_{DIV})

The one-dimensional theoretical performance calculations assume that flow at the nozzle exit is uniform and parallel to the nozzle axis. The cor-rection factor, φ_{DIV}, allows for nozzle divergence (i.e., for nonaxial flow) and for nonuniformity across the nozzle exit plane. It was calcu-lated by a computer program which utilized the axisymmetric method of characteristics for a variable-property gas. Computation began with a transonic analysis using series expansions of the differential equations of motion near Mach 1 to calculate the irrotational flow field. This provided a characteristic line for use in the analysis of the supersonic portion of the nozzle. The resulting pressures were integrated over the given geometry to give the geometric efficiency. Computations at each of the nine points of the experimental chamber pressure/mixture ratio matrix

showed the geometric efficiency to be essentially independent of both those parameters and to have the following value: $\omega_{DIV} = 1.022$. This value was based on an aerodynamic rather than a geometric throat radius, and was therefore reduced by the factors accounting for throat discharge coefficient (f_{DIS}) and throat radius change (f_{TR}).

Correction for Heat Losses (φ_{HL})

Heat loss correction factors for performance calculated from measured thrust are similar to those for performance calculated from chamber pressure, except that heat fluxes in the nozzle are included in the calculations. Thus, with the assumptions of constant specific heat and specific heat ratio in the nozzle (from start of convergence to exit), Eq. D-20 applies in the following modified form:

$$\varphi_{HL} = 1 + 1/2 \left[\frac{\Sigma (q/A)A}{\dot{w}_T} \right] \left[\frac{1 - (T_e/T_c)}{H_c - H_e} \right] \tag{D-26}$$

where T_e is the gas temperature at the nozzle exit and the summation of observed heat fluxes extends over the nozzle as well as the combustion chamber. With this same proviso, the alternate expression, Eq. D-21, is also applicable to estimation of φ_{HL}. Values obtained by both calculations are listed in Table D-2; averages of the two were used in reduction of test data.

TABLE D-2

TYPICAL HEAT LOSS CORRECTION FACTORS (φ_{HL})

P_c, psia	L*, inches	Heat Loss Correction Factor, φ_{HL}	
		By Eq. D-26	By Eq. D-21
50	30	1.009	1.019
100	3.4	1.002	1.004
	10	1.003	1.005
	30	1.009	1.015
200	30	1.009	1.015

REFERENCES

D-1. Havenstein, C. A.: <u>Alternate Throat Development Program for the</u>
<u>Apollo Command Module Reaction Control Engines</u>, Report No. R-5941,
Rocketdyne, a Division of North American Aviation, Inc., Canoga
Park, California, 16 November 1964.

D-2. Timoshenko, S. and J. N. Goodier: <u>Theory of Elasticity</u>, McGraw-
Hill Book Company, New York, N. Y., 1951.

D-3. <u>Chamber Technology for Space Storable Propellants</u> - Task II, Pre-
pared for National Aeronautics and Space Administration, Contract
NAS7-304, Report No. R-6028-2, Rocketdyne, a Division of North
American Aviation, Inc., Canoga Park, California, 13 October 1965.

D-4. Gerhauser, J. M. and R. J. Thompson, Jr.: <u>Theoretical Performance</u>
<u>Evaluation of Rocket Propellants</u>, Report No. R-5802, Rocketdyne, a
Division of North American Aviation, Inc., Canoga Park, California,
3 August 1964.

APPENDIX E

MEASUREMENT ERROR ANALYSIS

INTRODUCTION

Because it is not possible to measure the true value of any physical
property or parameter, the error limits, or uncertainty interval, associated
with any experimental measurement must be specified. It is the purpose of
this appendix to indicate the reliability of the experimental results of
this program by estimation of the errors inherent in the data acquisition
processes and in the calculation procedures. This will permit determina-
tion of the range within which, at a given confidence level, the true values
of the measured or calculated parameters may be expected to fall.

If error be identified with departure of an experimental measurement from
the "true" value, its magnitude can never be completely known; if it were
known, it would become a correction which could be systematically applied.
Hence, error limits can only be stated within probability limits. The
estimation is made by an error analysis procedure which, in the present
application, consists of the following steps:

1. Estimation of the uncertainty intervals in the individual trans-
    ducers, including the measuring systems in which they are used

2. Combination of the uncertainty intervals of duplicate or redundnat
    sensors into an uncertainty interval for the measurement

3. Combination of the uncertainty intervals of several measurements
    (e.g., pressure, temperature, and flowmeter frequency) into an
    uncertainty interval for the parameter they determine (e.g.,
    flowrate)

4. Combination of the uncertainty intervals of the measurements entering into calculation of the value of the desired variable (e.g., characteristic velocity) to estimate the uncertainty interval of the calculated result.

Two type of error are possible for any measurement:

1. Systematic errors. These are associated with the particular system, with the experimental techniques employed, or with the calibration procedures. They cannot be estimated by statistical methods, and are minimized primarily by careful calibration with the best available standards, by requirements for consistency and traceability of the experimental and calibration techniques, and by critical examination of experimental data.

2. Random errors. These arise from unpredictable and unknown variations in the experimental situation and are generally assumed to follow a normal distribution to permit simple statistical analysis. Error analysis is concerned only with random errors and implicitly assumes that systematic errors can be eliminated in a carefully conducted experimental program. From the properties of the normal, or Gaussian, distribution function, the probability of a system error exceeding ±1 times the standard deviation (σ) is about 32 percent, the probability of exceeding ±2 times the standard deviation is about 4.6 percent, and the probability of exceeding ±3 times the standard deviation is about 0.3 percent. The value of y in a result expressed as $(x \pm y)$ is generally taken as 2σ, thus setting the confidence level at 95 percent, so that the estimated odds of the true value of the result falling within the range $(x - y)$ to $(x + y)$ are 20:1.

SENSOR PRECISION

The precision of a measurement obtained as the output of a physical instrument or sensor is a quantitative estimate of the uncertainty associated with that measurement. This estimate is made by statistical analysis of the outputs of the sensor when repeatedly acted upon by known inputs. By sensor is meant not only the transducer itself but the complete system which converts the transducer signal to a numerical value of its physical parameter analog. The known inputs, of course, have uncertainty limits of their own, but for practical purposes it is assumed that they are accurate (i.e., identical to true values) within the limits required by the experimental situation. Ultimately, these inputs must be directly traceable to established standards, such as those of the National Bureau of Standards.

When a sensor is calibrated against known inputs, precision may be considered as the certification of an error band within the calibrated interval and within a given confidence level. Thus, it provides a measure of "closeness to truth" of the reduced data. Precision may be numerically expressed as the standard deviation of a measurement, which has the same units as the measurement itself, or as the coefficient of variation, which permits valid comparisons between measurements in different units. Coefficient of variation $\left(C_v\right)$ is the standard deviation expressed as a percentage of the mean, thus making it dimensionless:

$$C_v = 100 \frac{\sigma}{\mu} \qquad \text{(E-1)}$$

where

σ = standard deviation

μ = sample mean value

155

Pressure

The coefficients of variation of the pressure transducers were obtained by application of the Random Walk measurements analysis program to the calibration data, as discussed in Appendix C. The values obtained ranged from 0.23 to 0.92 percent, for static calibration made on a pressure manifold mounted on the thrust stand.

Other errors in pressure measurements may arise, in addition to the random, statistical uncertainty limits. Thus, in the measurement of chamber pressures through a drilled wall tap, erroneous values of stream pressure may be indicated because of the effect of the hole itself upon the flow. The following estimated magnitudes of this tap error, which is a function of stream velocity, are based on experimental data obtained with water and gas (Ref. E-1):

$$P_c-1 \quad (\text{Mach No.} \simeq 0): \quad 0.00\%$$

$$P_c-2 \quad (\text{Mach No.} \simeq 0.3): \quad 0.05$$

$$P_c-3 \quad (\text{Mach No.} \simeq 1.5): \quad 1.30$$

Coupling errors, arising from effects of the tubing joining the pressure taps to the transducers are not significant in the present series of experiments, since precise dynamic or transient response pressure measurements were not required (Ref. E-2) and tubing lengths were not greater than 3 feet.

Thrust

Values of coefficient of variation obtained by application of the Random Walk measurement analysis program to thrust calibrations were in the range

0.28 to 0.45 percent. Another possible source of error in thrust measurements arose from the necessity of taking system prerun zeros with the same degree of LF_2 inlet line chill as existed during the firings. On the basis of thrust calibrations made with chilled and unchilled LF_2 inlet lines, the estimated C_v value caused by maximum variation in zero readings varied from 0.05 percent (at 500 pound thrust level) to 0.15 percent (at 3400 pound thrust level).

Throat Area

Geometric throat diameter was measured with an expansion micrometer by two observers prior to, and following, every series of firings. Maximum coefficient of variation of the calculated areas was 0.48 percent. As the firing program progressed, the throat area became increasingly ellipsoidal, so that for the last four firings measurements of throat diameter at the minimum point were 4.175 ±0.003 inches and at the maximum point, 4.185 ±0.004 inches. These readings were averaged for calculation of equivalent circular area.

Volumetric Flowrate

The coefficients of variation of the turbine flowmeters used to measure LF_2 flowrate were determined from calibration data. Observed C_v values, which refer only to flow-bench water calibrations, were 0.02 percent for the Flo-Con meter and 0.06 percent for the Fischer-Porter meter. Corrections for thermal and viscosity effects in converting these calibrations to cryogenic LF_2 factors are discussed in another section of this report. In addition, however, there are unpredictable water-to-cryogenic calibration shifts (Ref. E-3) which introduce additional sources of error. The coefficient of variation arising from this source is approximately 0.5 percent (Ref. E-4).

Temperature

Resistance Temperature Sensors. The platinum resistance thermometers
were precision calibrated by the manufacturer. These calibrations were
checked by taking several emf readings with the sensors immersed in LN_2
and in LO_2 at atmospheric pressure; these were correct within the limits
of readability, with coefficient of variation less than 0.02 percent in
a series of four measurements. RSS error limits of these sensors based
on specifications for repeatability, insulation, time lag, friction heating,
and interchangeability were 0.1 percent. Voltage readout of the transducers
was adjusted to calibration values by means of a standard decade resistance
box with error limits of 0.2 percent.

Thermocouples. Iron-constantan thermocouples were used to measure temper-
atures of GH_2 in the venturi plenum, and chromel-alumel thermocouples were
used to measure chamber wall temperatures. Because the latter were not
involved in performance measurements and were used only to obtain heat flux
data, for which thermocouple uncertainty limits are negligible, they will
not be considered in this section. Estimated error to be expected with new
iron-constantan thermocouple wire at ambient temperatures is 0.7 percent
(Ref. E-1). Thermocouple calibrations were electrical only; i.e., the emf
readout was adjusted on the assumption that thermocouple-generated electro-
motive forces correspond to standard values. Total estimated C_v is 1.0
percent.

COMBINED ERROR ESTIMATION

Redundant Measurements

Two independent transducers were used to measure each of the important
parameters (except thrust) in order to increase measurement reliability.

The most probable value of a redundant measurement is a weighted average in which the weight (W_i) assigned to an individual determination is given by

$$W_i = \frac{1}{\sigma_i^2} \qquad (E-2)$$

where σ_i is the standard deviation associated with the ith measurement and σ_i^2 is the variance. The variance of the weighted mean, σ_m^2, is given by

$$\frac{1}{\sigma_m^2} = \sum_i \frac{1}{\sigma_i^2} \qquad (E-3)$$

Clearly, the variance of the weighted mean is less than any of the individual variances; for example, in the particular case of two measurements with equal variances, the variance of the mean is half the individual variances.

Combined Measurements

The standard deviation of a parameter which is a function of two or more independent measurements is taken as the root-sum-square (RSS) of the standard deviations of the independent measurements. Thus, LF_2 flowrate is a function of flowmeter frequency and fluorine temperature (assuming no significant error in conversion of fluorine temperature to equivalent density):

$$\dot{w}_o = \varphi\,(f,\,T_o) \qquad (E-4)$$

where

f = flowmeter frequency

T_o = oxidizer temperature

The standard deviation of the oxidizer flowrate is then:

$$\sigma_{\dot{W}_o} = \left[\sigma_f^2 + \sigma_{T_o}^2 \right]^{1/2} \tag{E-5}$$

In the same way, the standard deviation of the fuel flowrate, which is a function of measured pressure and temperature in the venturi plenum, is given by

$$\sigma_{\dot{W}_f} = \left[\sigma_{P_f}^2 + \sigma_{T_f}^2 \right]^{1/2} \tag{E-6}$$

where

σ_{P_f} = standard deviation of GH_2 pressure measurement

σ_{T_f} = standard deviation of GH_2 temperature measurement

Standard deviation is converted to coefficient of variation by Eq. E-1.

When several measured variables are combined algebraically to yield an experimental result, the standard deviation of the result, which takes into account the propagation of the individual errors, is given by

$$\sigma_R^2 = \left(\frac{\partial R}{\partial x_1} \sigma_1 \right)^2 + \left(\frac{\partial R}{\partial x_2} \sigma_2 \right)^2 + \ldots + \left(\frac{\partial R}{\partial x_n} \sigma_n \right)^2 \tag{E-7}$$

160

where

σ_R = standard deviation of calculated result

$x_1, x_2, \ldots, x_n$ = measured variables

$R = \phi(x_1, x_2, \ldots, x_n)$

$\sigma_1, \sigma_2, \ldots, \sigma_n$ = standard deviations of $x_1, x_2, \ldots, x_n$, respectively

The following example illustrates the application of this type of error analysis:

Run No. 178

Chamber pressure: σ_{P_c} = 0.25 psia

Calculated by Equations E-1 and E-3 from calibration C_v values (0.39 percent and 0.54 percent) of the redundant sensors.

Throat area: σ_{A_t} = 0.02 in.^{2}

Calculated from 12 measurements of throat diameter.

Thrust: σ_F = 7.2 lbf

Calculated from RSS of calibration C_v (0.37 percent) and zero point variation C_v (0.10 percent).

<u>Propellant flowrate</u>: $\qquad$ $\sigma_{\dot{w}_T} = 0.02$ lb/sec

a. Fluorine flowrate C_V (0.38 percent) calculated as RSS of flowmeter C_V (0.35 percent) and temperature C_V (0.15 percent), each obtained from C_V values of redundant measurements.

b. Hydrogen flowrate C_V (0.49 percent) calculated from venturi pressure C_V (0.38 percent) and temperature C_V (0.71 percent), each obtained from C_V values of redundant measurements, by application of Eq. E-7 to the expression $\dot{w}_{GH_2} = K\,P/\sqrt{T}$ $\qquad$ (K = constant).

c. Total flowrate C_V (0.41 percent) calculated from the following equation (Ref. E-5):

$$(C_V)^2_{\dot{w}_T} = \frac{r\,(C_V)^2_{\dot{w}_0} + (C_V)^2_{\dot{w}_f}}{r + 1} \qquad (E\text{-}8)$$

where

$$r = \text{mixture ratio } (\dot{w}_0/\dot{w}_f)$$

<u>Correction Factors</u>: $\qquad$ $\sigma_{C.F.} = 0.003$

Obtained from RSS of estimated variances of the individual corrections.

<u>c*, Based on P_c</u>: $\qquad$ $\sigma_{c*_{P_c}} = 39$ ft/sec

Obtained by application of Eq. E-7 to the expression

$$c* = \frac{P_c\,A_t\,g_c\,(C.F.)}{\dot{w}_T} \qquad (E\text{-}8)$$

where (C.F.) is the net correction factor.

162

The resulting expression is:

$$
\sigma_{c^*{}_{P_c}}^2 = \left[\frac{A_t\, g_c\, (C.F.)}{\dot{w}_T}\, \sigma_{P_c} \right]^2 + \left[\frac{P_c\, g_c\, (C.F.)}{\dot{w}_T}\, \sigma_{A_t} \right]^2 +
$$

$$
\left[-\frac{P_c\, A_t\, g_c\, (C.F\,)}{\dot{w}_T^2}\, \sigma_{\dot{w}_T} \right]^2 + \left[\frac{P_c\, A_t\, g_c}{\dot{w}_T}\, \sigma_{C.F.} \right]^2
$$

Substitution of numerical values gives $\sigma_{c^*{}_{P_c}}$.

<u>c*, Based on F:</u> $\qquad\qquad \sigma_{c^*{}_F} = 40$ ft/sec

Obtained by application of Eq. E-7 to the expression

$$
c^* = \frac{F\, g_c\, (C.F)}{C_F\, \dot{w}_T} \tag{E-9}
$$

where, again, $(C.F.)$ is the net correction factor.

The resulting expression is:

$$
\sigma_{c^*{}_F}^2 = \left[\frac{g_c\, (C.F.)}{C_F\, \dot{w}_T}\, \sigma_F \right]^2 + \left[-\frac{F\, g_c\, (C.F.)}{C_F\, \dot{w}_T^2}\, \sigma_{\dot{w}_T} \right]^2 +
$$

$$
\left[\frac{F\, g_c}{C_F\, \dot{w}_T}\, \sigma_{C.F.} \right]^2
$$

Substitution of numerical values gives $\sigma_{c^*{}_F}$.

As far as random errors only are concerned, there is no significant difference in estimated c* standard deviations based on chamber pressure and on thrust. Calculations similar to these for several other firings indicated only minor changes in σ_{c*} over the chamber pressure/mixture ratio matrix, as would be expected, since all calibrations (and hence the resulting C_v values) covered the entire range required of the sensors. The range of standard deviation was 31 ft/sec to 49 ft/sec, with an average value of 37 ft/sec.

DYNAMIC PRECISION

The estimates of expected standard deviations in characteristic velocity calculated above are based on static calibrations of pressure and thrust sensors, and hence may not be strictly applicable to the dynamic system represented by a firing thrust motor. It is generally assumed, however, that such calibration data may be extended without significant change to dynamic systems oscillating at very low frequencies and amplitudes, and that steady-state stable combustion is such a system.

An indication of the possible magnitude of the uncertainty interval associated with the experimental determination of characteristic velocity may be obtained by repeated firings of a motor with the same set of transducers. If systematic errors are assumed to be insignificant, variations from indicated "correct" values (i.e. those which are on the best curve through the experimental points) may be ascribed to random errors and hence are subject to statistical analysis. The usefulness of such an analysis is a direct function of the number of data points used to obtain the correct or average values. With only three or four data points available for determination of efficiency at a given pressure level, as in the present program, statistical calculations of measurement

reliability have no great absolute value but may be used for comparisons with those estimated from transducer calibrations. Such a comparison is shown in Table E-1, in terms of c* efficiency. The calibration-based estimates were derived from the average c* standard deviation of 37 ft/sec obtained above.

The experimental estimates were obtained from a confidence-limit analysis based on "Student's t", which is defined as

$$ t = \frac{\overline{x}_i - \overline{x}}{s_m} \tag{E-9} $$

where

$\overline{x}_i$ = sample mean calculated for an ith set of data

$\overline{x}$ = population mean of the population sampled by the ith set

s_m = square root of the variance of the mean of the ith set

Because $\overline{x}$ is unknown, t cannot be calculated explicity. However, the distribution function of t is known and this permits probability limits to be assigned to t intervals. Standard tables are availabel for facilitating these calculations.

On the basis of the data given in Table E-1, the experimental values of c* efficiency determined in the present program are estimated to have an error band of approximately ±1.0 percent at the 95 percent (2σ) confidence level and approximately ±0.5 percent at the 68 percent (1σ) confidence level.

TABLE E-1

ERROR BAND IN EXPERIMENTAL DETERMINATIONS

OF c* EFFICIENCIES

Confidence Level		Estimates Based on Static Calibrations		Estimates Based on Experimental Firings	
		95% (2σ)	68% (1σ)	95% (2σ)	68% (1σ)
Triplet Injector					
50 psia	Based on P_c	0.9%	0.5%	1.2%	0.7%
	Based on F	0.9	0.5	0.5	0.2
100 psia	Based on P_c	0.9	0.4	1.0	0.3
	Based on F	0.9	0.4	0.7	0.2
200 psia	Based on P_c	0.9	0.4	1.5	0.5
	Based on F	0.9	0.4	1.3	0.5
Doublet/Showerhead Injector					
50 psia	Based on P_c	0.9%	0.5%	2.0%	0.5%
	Based on F	0.9	0.5	1.0	0.2
100 psia	Based on P_c	0.9	0.4	1.5	0.4
	Based on F	0.9	0.4	2.7	0.6
200 psia	Based on P_c	0.9	0.4	3.0	0.7
	Based on F	0.9	0.4	2.5	0.6

REFERENCES

E-1. Dean, R.C., Jr., <u>Aerodynamic Measurements</u>, Gas Turbine Laboratory, Massachusetts Institute of Technology, Cambridge, Massachusetts, 1953.

E-2. Thomson, D.B., <u>The Effect of Tubing on Dynamic Pressure Recording</u>, TN-61-3, Rocketdyne, a Division of North American Aviation, Inc., Canoga Park, California, 28 February 1961.

E-3. Bucknell, R.L., "Calibration Systems and Turbine-Type Flow Transducers for Cryogenic Flow Measurements", <u>Advances in Cryogenic Engineering</u>, Vol. 8, Plenum Press, New York, 1963, pp. 360-369.

E-4. Alspach, W.J. and T. M. Flynn, "Considerations when Using Turbine-Type Flowmeters in Cryogenic Service", <u>Advances in Cryogenic Engineering</u>, Vol. 10, Plenum Press, New York, 1965, pp. 246-252.

E-5. Zimmerman, J.M., <u>Calibration Motor Program</u>, R. R. 56-30, Rocketdyne, a Division of North American Aviation, Inc., Canoga Park, California, 9 May 1956.

APPENDIX F

OSCILLATORY COMBUSTION IN LOW-L* CHAMBERS

The combustion instability observed in some of the experimental firings
in the 3.4-inch and 10-inch L* chambers is discussed briefly in this
appendix.

Twelve short-chamber runs were made at 100-psia nominal chamber pressure
(see Table 5), six each with the triplet and doublet/showerhead injectors,
of which three were at L* = 3.4 inches and three at L* = 10 inches;
respective injector face-to-throat chamber lengths were 2.4 inches
(injector joined directly to nozzle) and 5.6 inches. Chugging mode
combustion instability occurred in seven of these firings, as shown in
the oscillograms of the thrust measurement and in Fastax motion pictures
of the chamber exhaust and, in two cases, of the combustion chamber
(looking directly into the nozzle). Amplitudes and frequencies of the
combustion oscillations are given in Table F-1. Amplitudes represent
oscillatory variations of thrust (minimum to maximum points) expressed
as percentages of the mean values.

For both injectors, oscillation amplitude varied inversely with chamber
length. Thus, all of the firings in the 30-inch L* chamber were stable,
as were three of the six runs in the 10-inch L* chamber; in the other
three, oscillation amplitudes were less than 10 percent of the mean. Of
the six 3.4-inch L* firings, however, four were unstable, with amplitudes
ranging up to 36 percent of the mean.

Amplitude of oscillation was also a function of mixture ratio. For both
injectors at the highest mixture ratio (nominal $\dot{w}_o/\dot{w}_f = 15$) oscillation

169

TABLE F-1

AMPLITUDE AND FREQUENCY OF COMBUSTION INSTABILITY

IN LOW-L* FIRINGS

(NOMINAL P_c = 100 PSIA)

Run No.	Injector Type	L*, inches	Mixture Ratio	Combustion Oscillations	
				Frequency, cps	Amplitude, Peak-to-Peak, percent of mean value
204	Triplet	3.4	9.3	90	26
202	Triplet	3.4	11.8	90	15
203	Triplet	3.4	15.2	Stable	0
234	Triplet	10	9.6	250	9
233	Tiplet	10	12.7	Stable	0
232	Triplet	10	16.4	Stable	0
211	Doublet/ Showerhead	3.4	8.9	Stable*	0
208	Doublet/ Showerhead	3.4	12.7	250	36
209	Doublet/ Showerhead	3.4	15.5	250	4
207	Doublet/ Showerhead	10	9.2	300	6
205	Doublet/ Showerhead	10	12.3	300	8
206	Doublet/ Showerhead	10	15.3	Stable	0

*Unstable for first 350 milliseconds of run (170 cps, 20 percent of mean), but stable, thereafter.

amplitude was essentially zero in three cases out of four and 4 percent of the mean in the fourth. Maximum amplitudes were observed at the lowest mixture ratio (9 nominal) with the triplet injector, and at the intermediate mixture ratio (12 nominal) with the doublet/showerhead.

Low-frequency (chugging) instability results from interaction of propellant feed system dynamics and chamber combustion processes, including combustion time delay (time between injection and combustion of propellants). Mathematical models of bipropellant feed system-combustion chamber coupling as the controlling factor in low-frequency instability have recently been described (Ref. F-1 and F-2). With the LF_2/GH_2 combination, primary coupling probably involves the liquid fluorine feed system, because the compressible gas in the fuel manifold tends to isolate the GH_2 feed system from the combustion chamber.

Combustion oscillations at 100 to 400 cps were observed in LF_2/GH_2 experimental firings made at NASA Lewis in a thrust chamber fairly similar to the one employed in the present investigation (Ref. F-3). Modification of the liquid fluorine flow system to reduce its volume by about two-thirds alleviated the oscillations.

No detailed analyses were made of the observed instabilities, because (1) significant degrees of combustion instability were observed only in the very shortest L* chamber and only at the lower mixture ratios, (2) chugging oscillation is more a characteristic of the particular hardware system than of the propellant combination per se, and (3) chugging can usually be minimized by proper modification of the propellant supply system.

REFERENCES

F-1.   Fontaine, R.J., R. S. Levine, and L. P. Combs, Secondary, Nondestructive Instability in Medium-Size Liquid Rocket Engines, Presented at the 25th AGARD Colloquium on Advances in Tactical Rocket Propulsion, University of California, San Diego, California, April, 1965.

F-2.   Reardon, F.H. and R. C. Waugh, "Feed System Effects in Combustion Instability," Bulletin of the Fifth Liquid Propulsion Symposium, Vol. II, pp 843-862, Chemical Propulsion Information Agency, Silver Spring, Maryland, 13 November 1963.

F-3.   Price, H.G., Jr., R. J. Lubick, and A. M. Shinn, Jr., Investigation of Injectors for a Low Chamber Pressure Hydrogen-Fluorine Rocket Engine, Technical Memorandum No. X-485, National Aeronautics and Space Administration, July 1962 (CONFIDENTIAL)

APPENDIX G

COLD FLOW STUDIES

INTRODUCTION

This appendix presents experimental details of a short photographic study
carried out to characterize qualitatively the liquid atomization processes
of triplet and doublet/showerhead injection elements typical of those used
in the respective injectors.

The oxidizer simulant was water, fuel simulant was helium, and flow
conditions were such that liquid/gas momentum ratio was the same in the
cold flows as in the hot firings. Both microflash and schlieren motion
pictures were made.

INJECTOR ELEMENTS

The single-element injectors used for the cold flow experiments were
modeled directly from the injectors used for the hot firings and were
fabricated from 4-inch-diameter aluminum blocks. Face patterns and
dimensions are shown in Fig. G-1. Note that four fuel orifices were
used with the single pair of oxidizer orifices in the doublet/showerhead
element, instead of two, as in the large injector. This was done to
simulate the "environment" of the liquid streams, so that atomization
would be uniform.
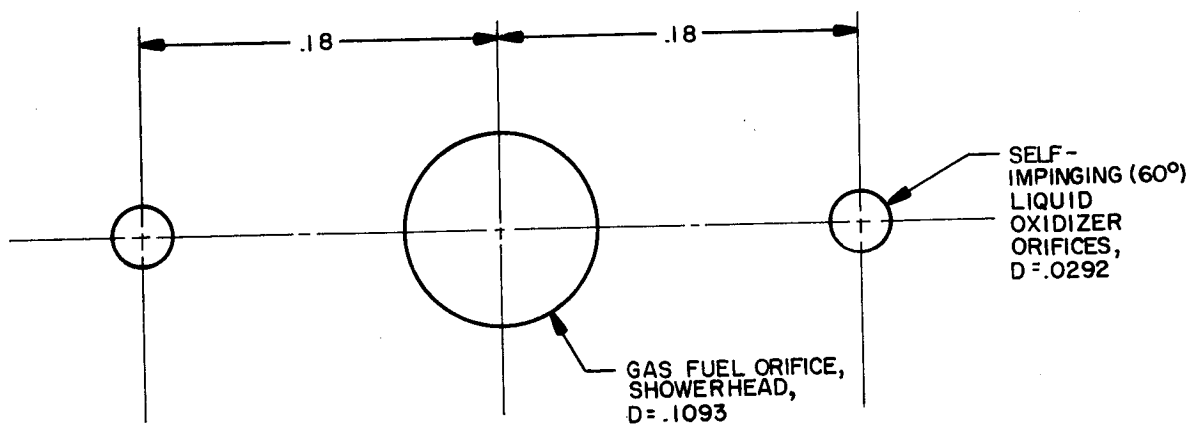
(a) TRIPLET
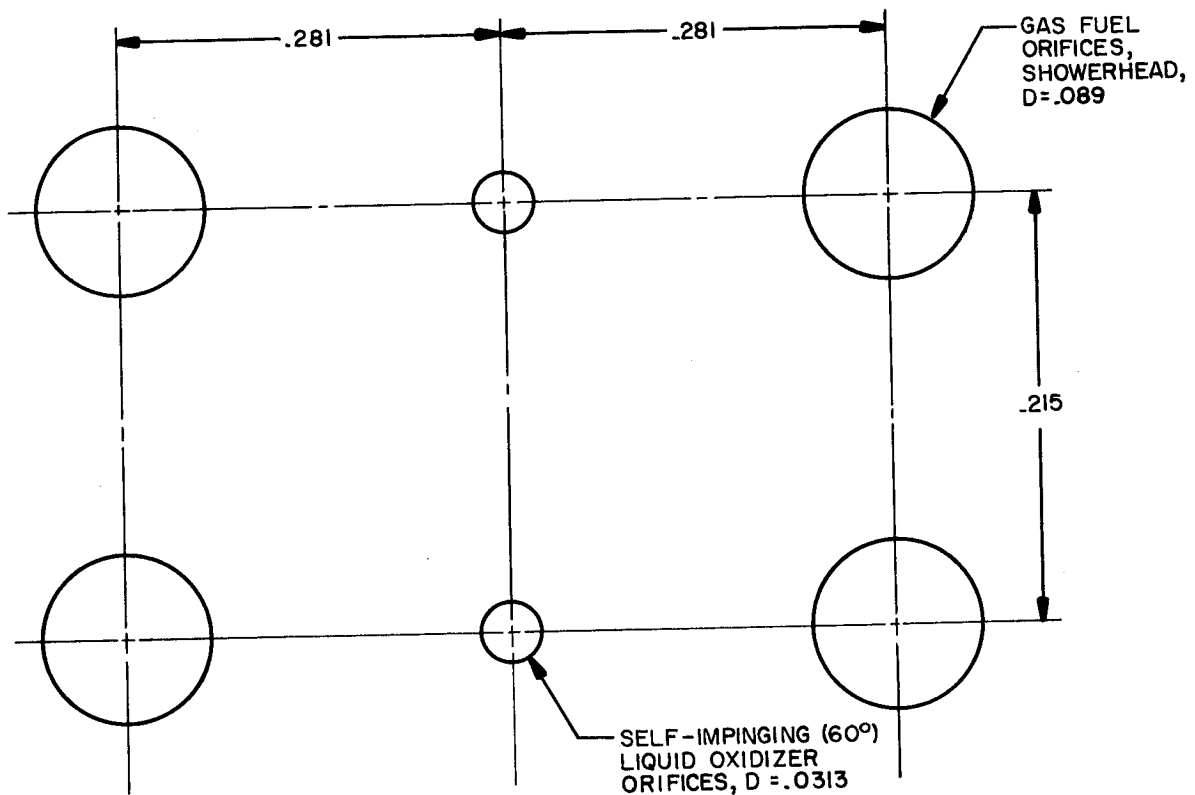
(b) DOUBLET/SHOWERHEAD

Figure G-1. Patterns and Dimensions of Single-Element Units Used for Cold-Flow Simulation of the Triplet and Doublet/Showerhead Injector Configurations.

The criterion used for sizing the single-element cold flow injectors
was maintenance of equality of the following three parameters in the
cold flows and hot firings:

    1.   Fuel orifice sizes

    2.   Gas injection Mach numbers

    3.   Liquid/gas momentum ratio

Design calculations were based on the central point of the hot-firing
parametric matrix (chamber pressure = 100 psia, mixture ratio = 12) and
assumed that pressure at the exit of the gas orifices was atmospheric.
Comparisons of various hot firing and cold flow conditions are given
in Table G-1, with the following nomenclature:

      D   =   orifice diameter

      M   =   Mach number

   MOM =   momentum rate

      V   =   velocity

  M.R. =   mixture ratio

TABLE G-1

COMPARISON OF COLD FLOW SIMULATION CONDITIONS WITH HOT FIRING
AT CHAMBER PRESSURE = 100 PSIA AND MIXTURE RATIO = 12

Parameter	Triplet	Doublet/Showerhead
D_{H_2}/D_{He}	1	1
D_{F_2}/D_{H_2O}	1.3	1.4
M_{H_2}/M_{He}	1	1
$(MOM)_{H_2}/(MOM)_{He}$	5.0	5.3
$(MOM)_{F_2}/(MOM)_{H_2O}$	5.0	5.3
$(MOM\ RATIO)_{F_2/H_2}/(MOM\ RATIO)_{H_2O/He}$	1	1
$(V_{H_2}/M.R.) / (V_{He}/M.R.)$	1.9	1.9
$(V/D)_{F_2} / (V/D)_{H_2O}$	1	1

By maintaining equal liquid/gas momentum ratios as well as gas orifice
sizes and exit Mach numbers in the cold flows and hot firings, the momen-
tum levels could not be held the same, as indicated in Table G-1. The
ratio $V_{gas}/M.R.$ appears in the drop size parameter expression (Eq. 2).
Equality of liquid V/D ratio relates to equal mean drop sizes, according
to the Ingebo criterion.

Procedure

Water and helium flowrates were set by upstream pressure adjustments, with the use of direct-reading pressure gages and the assumption of $C_D = 0.75$.

Motion pictures of the spray patterns were made with a 16-millimeter Fastax camera after the flows were established. The field of view extended to three inches from the injector face. Two types of photography were used:

1. Microflash; light source was an Edgerton, Germeshauser and Grier strobe unit (Model 549) with one mocrosecond flash duration and 4000 frames per second camera speed.

2. Schlieren; a six-inch parabolic mirror was used behind the spray in conjunction with the schlieren unit, and camera speed was 4000 frames per second.

The photographs shown in the body of this report (Fig. 30 and 31) are enlargements of single frames taken from the latter portion of each run.

APPENDIX H

CALCULATION OF HEAT FLUX AND HEAT TRANSFER COEFFICIENTS

INTRODUCTION

Chamber and nozzle transient heat flux and heat transfer coefficients were determined from temperature-time data obtained on the cold side of the isolated measuring segments described in Appendix A. This appendix details the computational procedures employed in determining these parameters.

Two methods are available for calculating the convective heat transfer coefficient from measured cold wall transient temperature: the first assumes infinite thermal conductivity of the segment material and the form of the temperature distribution across it; the second method involves solution of the one-dimensional transient conduction equation, with material properties evaluated at a suitable mean temperature. The first method is simpler from a computational standpoint, but is less exact than the second. However, the former gives values of heat flux and convective heat transfer coefficient which are close to the more exact method if heat flux from gas to wall is not excessive or wall thickness too great. A comparison of heat transfer coefficients obtained by each procedure is given below.

INFINITE CONDUCTIVITY METHOD

The simpler of the two calculation procedures, referred to as the "infinite conductivity" method, is as follows.

179

On the basis of an average temperature of the isolation segment, the following heat balance may be written:

$$\left(\frac{q}{A}\right) d\theta = \left(\frac{c_p W}{A}\right) d\overline{T}$$

or

$$\frac{q}{A} = \left(\frac{c_p W}{A}\right) \frac{d\overline{T}}{d\theta} \tag{H-1}$$

where

q/A = heat flux to element, $Btu/in.^2$-sec

c_p = specific heat of the material in the measuring element $(Btu/lb/F)$, assumed constant

W = total mass of element, pound

A = cross-sectional area of element, sq. in.

$\overline{T}$ = average element temperature (averaged over time, $d\theta$, and length)

θ = time, seconds

If the internal thermal resistance of the segment is negligibly small with respect to the external film resistance, then, after an initial time lag, the temperature-time gradients at the hot and cold element walls are very nearly equal to each other and to the gradient of the average temperature:

$$\frac{d\overline{T}}{d\theta} \sim \frac{dT_c}{d\theta} \sim \frac{dT_h}{d\theta} \tag{H-2}$$

where

T_c = Temperature at the cold wall

T_h = Temperature at the hot wall

Hence Eq. H-1 may be written:

$$\frac{q}{A} = \left(c_p \frac{W}{A}\right) \frac{dT_c}{d\theta} \qquad (H-3)$$

which permits calculation of q/A from the observed cold-side temperature-time gradient and average c_p value of the element.

If the cold wall is assumed to be adiabatic then the following boundary conditions apply:

$$\frac{dT_c}{dx} = 0 \qquad (H-4)$$

$$\frac{dT_h}{dx} = -\frac{q/A}{k} \qquad (H-5)$$

where

   k = thermal conductivity of the segment material, Btu/in./sec/F

A quadratic temperature distribution is assumed in the heat transfer segment, as indicated in Fig. H-1. To satisfy the boundary conditions of Eq. H-4 and H-5, this takes the following form:

$$T_x = T_c + (L-x)^2 \left(\frac{q/A}{2kL}\right) \qquad (H-6)$$
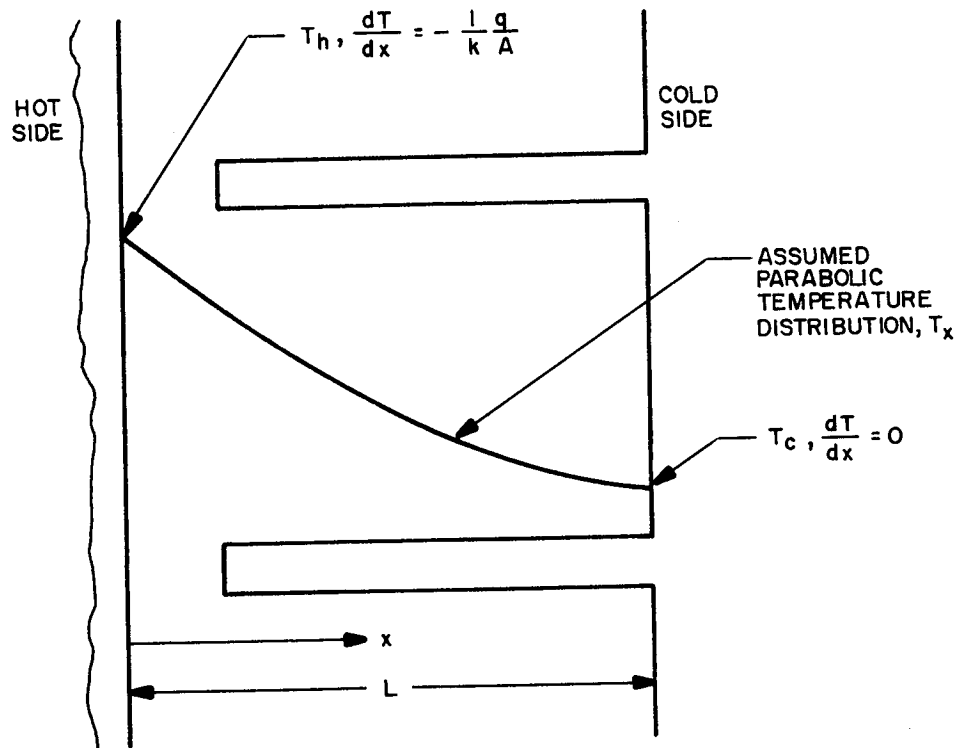
Figure H-1. Cross Section of Typical Heat Transfer Segment, Showing Assumed Parabolic Temperature Distribution along the Length, L.

Hence,

$$\frac{dT_x}{dx} = - (L-x)\left(\frac{q/A}{kL}\right) \tag{H-7}$$

whence Eq. H-5 follows at $x = 0$, $T_x = T_h$.

The hot wall temperature is obtained from Eq. H-6 as:

$$T_h = T_c + \frac{(q/A)\,L}{2k} \tag{H-8}$$

The local heat flux, q/A, is related to the heat transfer coefficient by the expression

$$q/A = h_g \left(T_{aw} - T_h\right) \tag{H-9}$$

where

h_g = heat transfer coefficient, $\text{Btu/in.}^2\text{-sec-F}$

T_{aw} = adiabatic wall temperature, R

T_h = hot wall temperature, R

Substitution of Eq. H-3 and H-8 into Eq. H-9, and writing

$$\frac{W}{A} = \rho\,L \tag{H-10}$$

where

W = total mass of isolation segment, lbm

A = cross-sectional area of segment, sq. in.

ρ = density of segment material, lbm/in^3

L = length of segment, inches

gives:

$$h_g = \left[\frac{T_{aw} - T_c}{c_p \rho L \, (dT_c/d\theta)} - \frac{L}{2k} \right]^{-1} \tag{H-11}$$

Under the conditions of the experimental firings, the adiabatic wall temperature may be taken as the stream stagnation temperature, with insignificant error, as shown by the following considerations.

For turbulent boundary layer flow, the following equation applies:

$$\frac{T_{aw} - T_s}{T_0 - T_s} = (Pr)^{1/3} \tag{H-12}$$

where

T_{aw} = adiabatic wall temperature

T_s = local static temperature

T_0 = gas stream stagnation temperature

Pr = Prandtl number

For laminar boundary layer flow, the Prandtl number exponent in Eq. H-12 is 1/2.

Values of Pr obtained from the theoretical performance calculations for LF_2/GH_2 ranged from 0.757 $(P_c = 50 \text{ psia, M.R.} = 15)$ to 0.770 $(P_c = 200 \text{ pisa,}$ M.R. = 9), with a typical value of 0.762 $(P_c = 100 \text{ psia, M.R.} = 12)$. In the throat region, the static-to-total temperature ratio is 0.92. Substitution into Eq. H-12 gives:

$$T_{aw} = (0.762)^{1/3} \left[T_o - 0.92 \ T_o \right] + 0.92 \ T_o = 0.99 \ T_o \qquad (\text{H-13})$$

In the combustion chamber, the adiabatic recovery temperature is even closer to gas stagnation temperature because gas velocity is lower. Actual stagnation temperature is obtained from theoretical combustion gas stagnation temperature by appropriate reduction for combustion efficiency, η_c*:

$$T_{aw} = (T_o)_{theo} \ (\eta_c*)^2 \qquad (\text{H-14})$$

Thermal properties of copper as a function of temperature are shown in Fig. H-2, and the factors $(\rho \ Lc_p)$ and (L/2k), used in Eq. H-11, are presented in Fig. H-3 and H-4. The average outside wall temperature in the interval taken for the slope $dT_c/d\theta$ was used in Eq. H-11, and thermal properties were evaluated at the corresponding midpoint temperature:

$$\overline{T} = T_c + \left(\rho \ Lc_p \ \frac{dT_c}{d\theta} \right) \left(\frac{L}{6k} \right) \qquad (\text{H-15})$$

A highly accurate value of average segment temperature is not essential, because the heat capacity changes by only one percent per 100 F change in temperature.

Figure H-2. Thermal Properties of Copper.
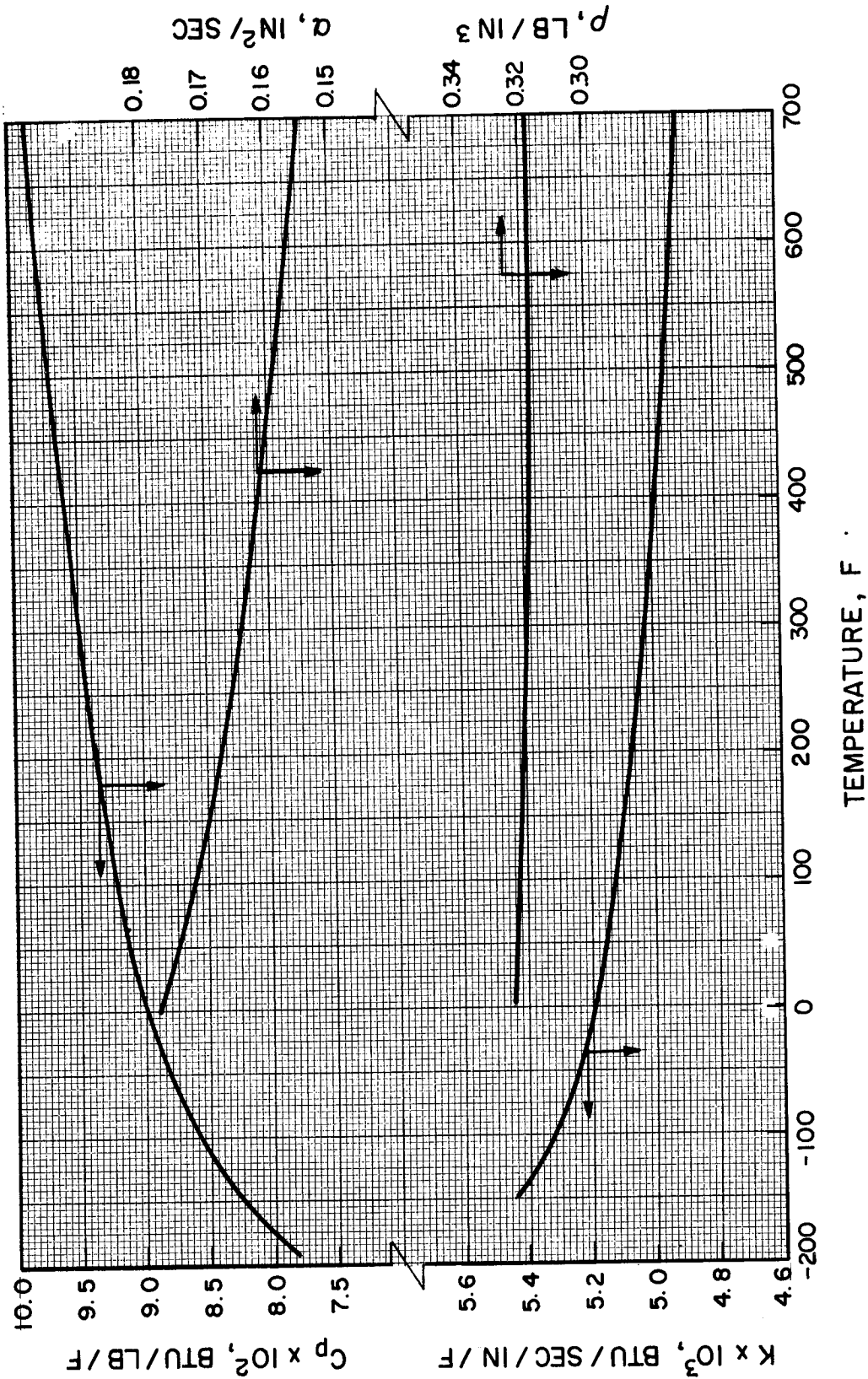
k = Thermal Conductivity
c_p = Heat Capacity
ρ = Density
α = Thermal Diffusivity
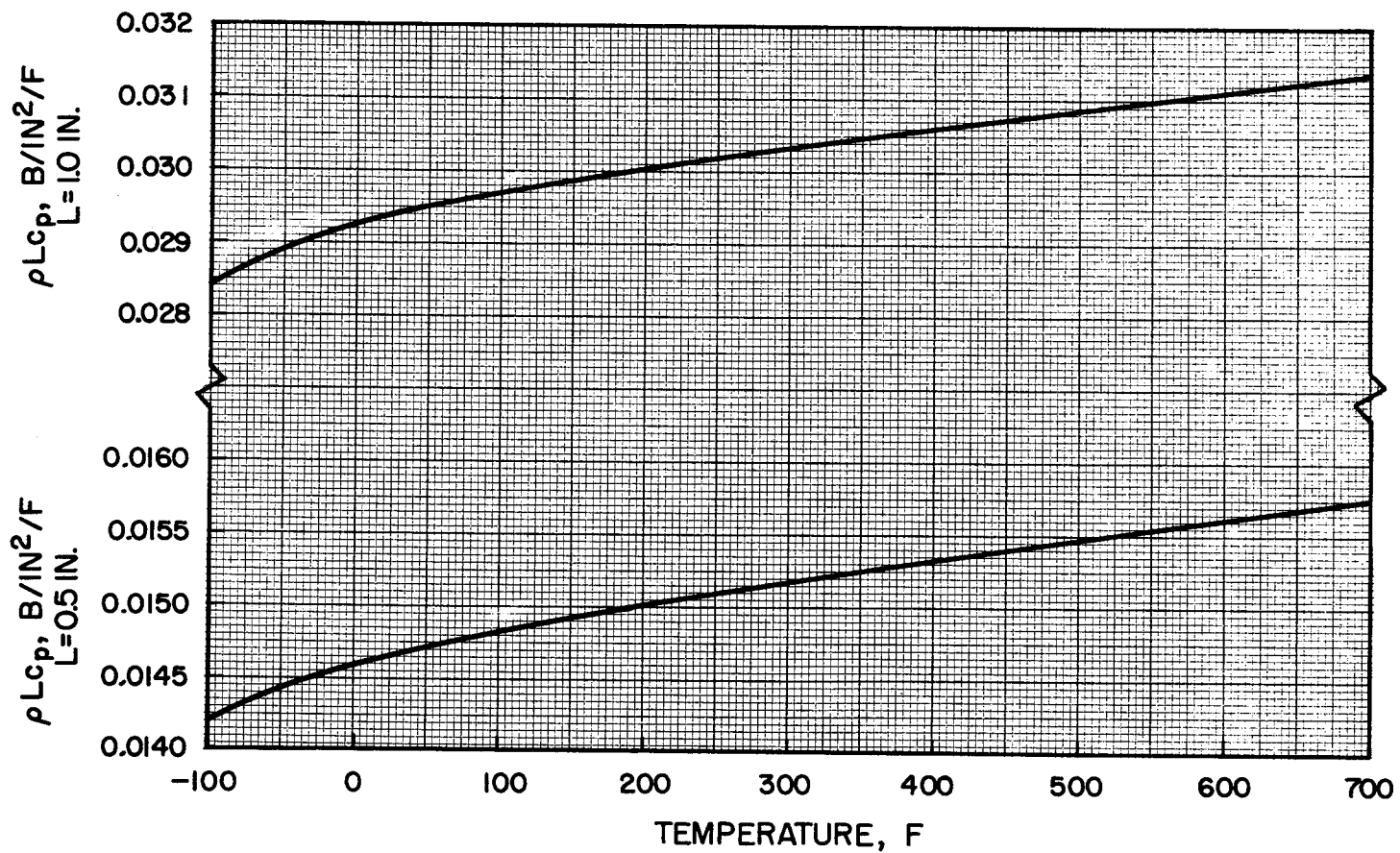
Figure H-3. Specific Heat of Copper Heat Transfer Segments in Chamber (L = 0.5 inches) and in Nozzle (L = 1.0 inches) as Function of Temperature.
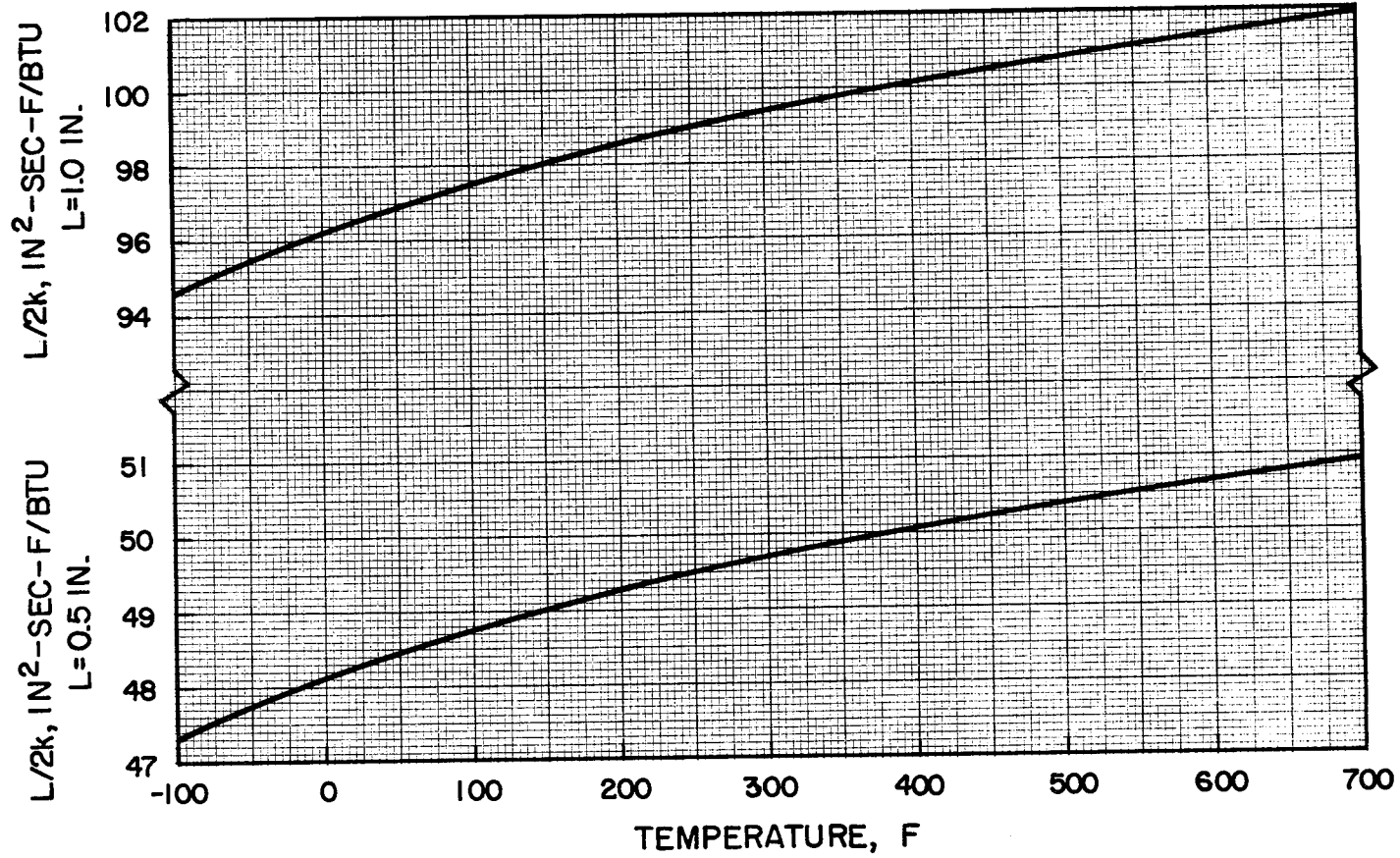
Figure H-4. Thermal Resistive Functions of Copper Heat Transfer Segments in Chamber (L = 0.5 inches) and in Nozzle (L = 1.0 inches).

The above analysis is strictly valid only at the instant in time when the hot wall temperature is T_h, because q/A is dependent upon T_h and h_g itself is not completely independent of T_h.

The essential conditions for application of this method, stated in Eq. H-2, are attained when the internal conductive thermal resistance of the element is negligibly small compared to the external convective film resistance. The ratio of the resistances is conveniently expressed by the dimensionless Biot modulus:

$$\frac{\text{Internal resistance}}{\text{External resistance}} = \frac{L/k}{1/h_g} = \frac{\frac{h_g L}{k}}{} = Bi \qquad (H-16)$$

When the Biot modulus is no greater than 0.1, the temperature-time gradients at the cold and hot walls of an element are equal to within less than 3 percent (Ref. H-1).

ONE-DIMENSIONAL EQUATION METHOD

The second computational procedure involves the use of transient conduction charts obtained from solution of the one-dimensional conduction equation. Such a chart, covering the range of Biot and Fourier numbers of interest, is shown in Fig. H-5 (Ref. H-2).

The heat transfer coefficient is determined by computing the value of

$$\frac{T_{aw} - T_c}{T_{aw} - \left(T_c\right)_{initial}}$$
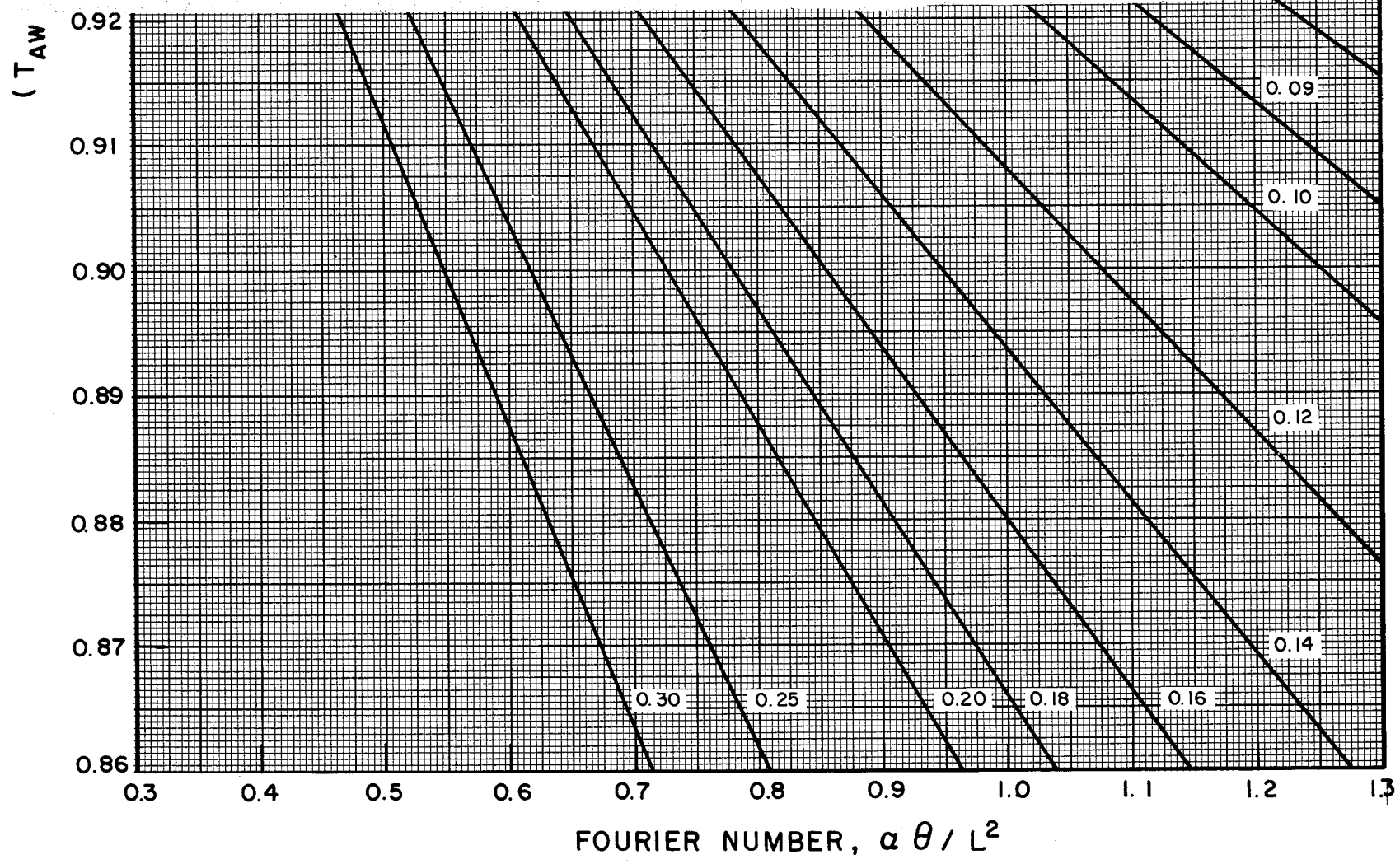
Figure H-5. Transient Conduction Chart for Copper Heat Transfer Segments.
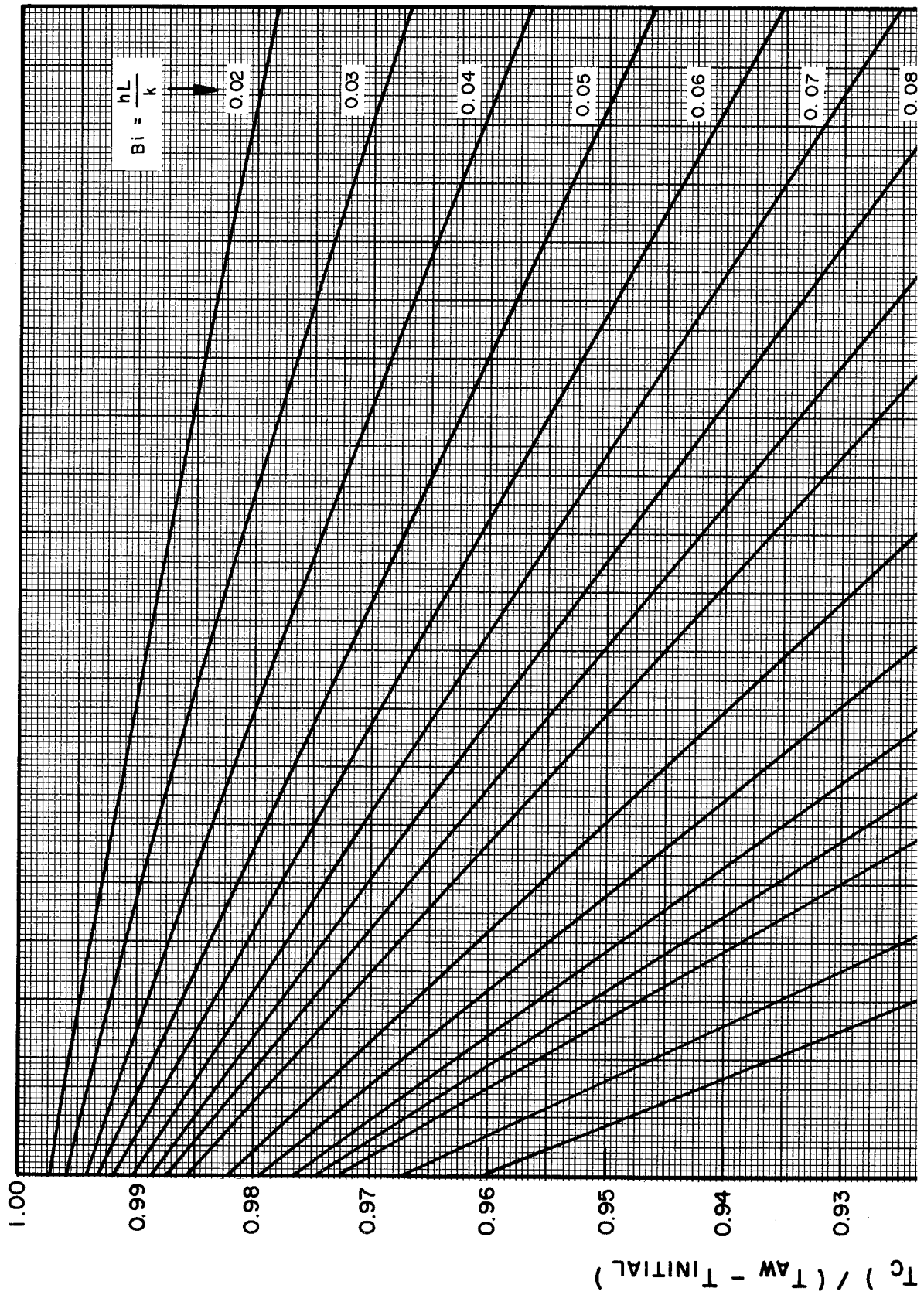
from measured cold wall temperatures at the initial and final points.
The Fourier number

$$\frac{\alpha \, \theta}{L^2}$$

is calculated, based upon the run duration, θ, and thermal diffusivity,
α, evaluated at an estimated midpoint temperature. The Biot number,
from which the heat transfer coefficient is calculated, is then read
from the transient conduction chart.

COMPARISON OF METHODS

Values of heat transfer coefficients for Run No. 237, calculated by
both procedures, are given in Table H-1.

The agreement between the two computational methods is good, with average
variation of three percent and maximum variation of four percent. Examin-
ation of Eq. H-11 indicates that agreement should even be better at 50-
and 100-psia chamber pressures because of the lesser effect of the thermal
resistance term, L/k, at lower heat fluxes. Consequently, the infinite
conductivity method with parabolic temperature gradient was used to
determine convective heat transfer coefficients.

TABLE H-1

COMPARISON OF HEAT TRANSFER COEFFICIENTS DETERMINED BY TWO
METHODS, RUN NO. 237

(Nominal Chamber Pressure = 200 psia)

Location of Isolation Segment	h_g, Btu/in.^{2}/sec/F	
	Infinite Conductivity Method	Transient Conduction Chart Method
Chamber, Injector End	12.6×10^{-4}	13.1×10^{-4}
Chamber, Center	10.3×10^{-4}	10.5×10^{-4}
Nozzle, Convergent Portion	11.3×10^{-4}	11.4×10^{-4}
Nozzle, Throat	11.2×10^{-4}	11.6×10^{-4}

REFERENCES

H-1. Krieth, F.: Principles of Heat Transfer, International Textbook Company, Scranton, Pennsylvania, 1958, pp. 136-137.

H-2. Talmor, E., Toroidal Tube Heat Transfer with and without Film Cooling, Report No. RR 63-28, Rocketdyne, a Division of North American Aviation, Inc., Canoga Park, California, October 1963.

DOCUMENT CONTROL DATA · R&D

(Security classification of title, body of abstract and indexing annotation must be entered when the overall report is classified)

1. ORIGINATING ACTIVITY (Corporate author)	2a. REPORT SECURITY CLASSIFICATION
Rocketdyne, a Division of North American Aviation Inc., 6633 Canoga Avenue, Canoga Park, California	Unclassified
	2b. GROUP

3. REPORT TITLE

Fluorine-Hydrogen Performance Evaluation.   Phase I, Part I: Analysis, Design, and Demonstration of High-Performance Injectors For The Liquid Fluorine-Gaseous Hydrogen Propellant Combination

4. DESCRIPTIVE NOTES *(Type of report and inclusive dates)*

Final Report , August 1966

5. AUTHOR(S) *(Last name, first name, initial)*

Arbit, H. A.

Clapp, S. D.

6. REPORT DATE	7a. TOTAL NO. OF PAGES	7b. NO. OF REFS
August 1966	204	48

8a. CONTRACT OR GRANT NO.	9a. ORIGINATOR'S REPORT NUMBER(S)
NASw-1229	
b. PROJECT NO.	R-6636-1
c.	9b. OTHER REPORT NO(S) (Any other numbers that may be assigned this report)
d.	NASA CR-54978

10. AVAILABILITY/LIMITATION NOTICES

11. SUPPLEMENTARY NOTES	12. SPONSORING MILITARY ACTIVITY
	National Aeronautics and Space Administration Lewis Research Center Cleveland, Ohio

13. ABSTRACT

Results are reported of a program covering the analysis design, and evaluation of two injectors giving high performance with LF_2/GH_2 over a nine-point matrix of chamber pressure (50, 100, 200 psia) ^{2} and ^{2} mixture ratio (9, 12, 15). A segmented, calorimetric thrust chamber was used. ($L^*=30$ in., vacuum thrust=2500 lb at a chamber pressure of 100 psia, and mixture ratio 12). One injector ($LF-GH_2-LF_2$ triplet) produced a corrected c* efficiency of 98 to 100 percent over the parametric matrix; the other (LF_2 doublet/GH_2 showerhead), a corrected c* efficiency of 97 to 100 percent. Reductions in chamber length to $L^*=10$ in. and $L^*=3.4$ in. decreased c* efficiency of the doublet/showerhead injector more than that of the triplet. Heat flux measurements were made and are reported.

DD FORM 1 JAN 64 **1473**

14.	KEY WORDS	LINK A		LINK B		LINK C	
		ROLE	WT	ROLE	WT	ROLE	WT
	Fluorine						
	Hydrogen						
	Injectors						
	Design						
	Performance						
	Heat Flux						

INSTRUCTIONS

1. ORIGINATING ACTIVITY: Enter the name and address of the contractor, subcontractor, grantee, Department of Defense activity or other organization (corporate author) issuing the report.

2a. REPORT SECURITY CLASSIFICATION: Enter the over-all security classification of the report. Indicate whether "Restricted Data" is included. Marking is to be in accordance with appropriate security regulations.

2b. GROUP: Automatic downgrading is specified in DoD Directive 5200.10 and Armed Forces Industrial Manual. Enter the group number. Also, when applicable, show that optional markings have been used for Group 3 and Group 4 as authorized.

3. REPORT TITLE: Enter the complete report title in all capital letters. Titles in all cases should be unclassified. If a meaningful title cannot be selected without classification, show title classification in all capitals in parenthesis immediately following the title.

4. DESCRIPTIVE NOTES: If appropriate, enter the type of report, e.g., interim, progress, summary, annual, or final. Give the inclusive dates when a specific reporting period is covered.

5. AUTHOR(S): Enter the name(s) of author(s) as shown on or in the report. Enter last name, first name, middle initial. If military, show rank and branch of service. The name of the principal author is an absolute minimum requirement.

6. REPORT DATE: Enter the date of the report as day, month, year; or month, year. If more than one date appears on the report, use date of publication.

7a. TOTAL NUMBER OF PAGES: The total page count should follow normal pagination procedures, i.e., enter the number of pages containing information.

7b. NUMBER OF REFERENCES: Enter the total number of references cited in the report.

8a. CONTRACT OR GRANT NUMBER: If appropriate, enter the applicable number of the contract or grant under which the report was written.

8b, 8c, & 8d. PROJECT NUMBER: Enter the appropriate military department identification, such as project number, subproject number, system numbers, task number, etc.

9a. ORIGINATOR'S REPORT NUMBER(S): Enter the official report number by which the document will be identified and controlled by the originating activity. This number must be unique to this report.

9b. OTHER REPORT NUMBER(S): If the report has been assigned any other report numbers (either by the originator or by the sponsor), also enter this number(s).

10. AVAILABILITY/LIMITATION NOTICES: Enter any limitations on further dissemination of the report, other than those imposed by security classification, using standard statements such as:

(1) "Qualified requesters may obtain copies of this report from DDC."

(2) "Foreign announcement and dissemination of this report by DDC is not authorized."

(3) "U. S. Government agencies may obtain copies of this report directly from DDC. Other qualified DDC users shall request through

_____."

(4) "U. S. military agencies may obtain copies of this report directly from DDC. Other qualified users shall request through

_____."

(5) "All distribution of this report is controlled. Qualified DDC users shall request through

_____."

If the report has been furnished to the Office of Technical Services, Department of Commerce, for sale to the public, indicate this fact and enter the price, if known.

11. SUPPLEMENTARY NOTES: Use for additional explanatory notes.

12. SPONSORING MILITARY ACTIVITY: Enter the name of the departmental project office or laboratory sponsoring (paying for) the research and development. Include address.

13. ABSTRACT: Enter an abstract giving a brief and factual summary of the document indicative of the report, even though it may also appear elsewhere in the body of the technical report. If additional space is required, a continuation sheet shall be attached.

It is highly desirable that the abstract of classified reports be unclassified. Each paragraph of the abstract shall end with an indication of the military security classification of the information in the paragraph, represented as (TS), (S), (C), or (U).

There is no limitation on the length of the abstract. However, the suggested length is from 150 to 225 words.

14. KEY WORDS: Key words are technically meaningful terms or short phrases that characterize a report and may be used as index entries for cataloging the report. Key words must be selected so that no security classification is required. Identifiers, such as equipment model designation, trade name, military project code name, geographic location, may be used as key words but will be followed by an indication of technical context. The assignment of links, rules, and weights is optional.

DISTRIBUTION LIST

	No. of Copies
National Aeronautics and Space Administration Washington, D. C. 20546 Attn: Mr. Charles H. King, Code MAT	1
National Aeronautics and Space Administration Washington, D. C. 20546 Attn: Mr. Robert F. Schmidt, Code SV	1
National Aeronautics and Space Administration Marshall Space Flight Center Huntsville, Alabama 35812 Attn: Mr. L. W. Jones, H–P&VE–PAS	1
National Aeronautics and Space Administration Manned Spacecraft Center Houston, Texas 77058 Attn: Mr. H. J. Brasseaux, PESD–Propulsion	1
National Aeronautics and Space Administration Goddard Space Flight Center Greenbelt, Maryland 20771 Attn: Mr. C. R. Gunn Delta Propulsion Office	1
National Aeronautics and Space Administration Kennedy Space Flight Center Cocoa Beach, Florida 32931 Attn: Mr. R. A. Raffaelli	1
Jet Propulsion Laboratory 4800 Oak Grove Drive Pasadena, California 91103 Attn: Mr. W. B. Powell	1
Scientific and Technical Information Facility Attn: NASA Representative, Code CRT P. O. Box 5700 Bethesda, Maryland 20014	1

National Aeroanutics and Space Administration   1
Lewis Research Center
21000 Brookpark Road
Cleveland, Ohio
Attn: Mr. John Gregory
      Mail Stop 500-209

National Aeronautics and Space Administration   1
Lewis Research Center
21000 Brookpark Road
Cleveland, Ohio
Attn: Mr. Carl Aukerman
      Mail Stop 86-1

National Aeronautics and Space Administration   1
Lewis Research Center
21000 Brookpark Road
Cleveland, Ohio
Attn: Mr. Art Curren
      Mail Stop 6-1

National Aeroanutics and Space Administration   1
Lewis Research Center
21000 Brookpark Road
Cleveland, Ohio
Attn: Mr. Howard Douglass
      Mail Stop 500-208

NASA Headquarters,   2
Washington, D.C. 20546
Contracting Officer, BCA
Patent Officer, AGP

NASA Lewis Research Center   3
21000 Brookpark Road
Cleveland, Ohio 44135
Office of Technical Information
Contracting Officer
Patent Office

NASA Headquarters   4
Office of Advanced Research and Technology
Washington, D.C. 20546
Chief, Liquid Experimental Engineering, RPX

Aerospace Corporation   1
2400 East El Segundo Boulevard
P. O. Box 95085
Los Angeles, California 90045
Attn: John G. Wilder
        MS-2293
        Propulsion Dept.

Arthur D. Little, Inc.   1
20 Acorn Park
Cambridge, Massachusetts 02140
Attn: E. Karl Bastress

Douglas Aircraft Company   1
Astropower Laboratory
2121 Paularino
Newport Beach, California 92663
Attn: Dr. George Moc
        Director, Research

Astrosystems International, Inc.   1
1275 Bloomfield Avenue
Fairfield, New Jersey 07007
Attn: A. Mendenhall

Atlantic Research Corporation   1
Edsall Road and Shirley Highway
Alexandria, Virginia 22314
Attn: A. Scurlock

Beech Aircraft Corporation   1
Boulder Division
Box 631
Boulder, Colorado
Attn: J. H. Rodgers

Bell Aerosystems Company   1
P. O. Box 1
Buffalo, New York 14240
Attn: W. M. Smith

Bendix Systems Division
Bendix Corporation
3300 Plymouth Road
Ann Arbor, Michigan
Attn: John M. Brueger

       1

Boeing Company
P. O. Box 3707
Seattle, Washington 98124
Attn: J. D. Alexander

       1

Chrysler Corporation
Missile Division
P. O. Box 2628
Detroit, Michigan 48231
Attn: John Gates

       1

Curtiss-Wright Corporation
Wright Aeronautical Division
Wood-Ridge, New Jersey 07075
Attn: G. Kelley

       1

Douglas Aircraft Company
Missile and Space Systems Division
3000 Ocean Park Boulevard
Santa Monica, California 90406
Attn: R. W. Hallet
       Chief Engineer
       Advanced Space Tech.

       1

Fairchild Hiller Corporation
Aircraft Missiles Division
Hagerstown, Maryland 10
Attn: J. S. Kerr

       1

General Dynamics/Astronautics
Library & Information Services (128-00)
P. O. Box 1128
San Diego, California 92112
Attn: Frank Dore

       1

General Electric Company
Re-Entry Systems Department
3198 Chestnut Street
Philadelphia, Pennsylvania 19101
Attn: F. E. Schultz

       1

General Electric Company   1
Advanced Engine & Technology Dept.
Cincinnati, Ohio 45215
Attn: D. Suichu

Grumman Aircraft Engineering Corp.   1
Bethpage, Long Island
New York
Attn: Joseph Gavin

Ling-Temco-Vought Corporation   1
Astronautics
P.O. Box 5907
Dallas, Texas 75222
Attn: Warren C. Trent

Lockheed California Company   1
2555 North Hollywood Way
Burbank, California 91503
Attn: G. D. Brewer

Lockheed Missiles and Space Co.   1
Technical Information Center
P.O. Box 604
Sunnyvale, California 94088
Attn: Y. C. Lee

Lockheed Propulsion Company   1
P. O. Box 111
Redlands, California 92374
Attn: H. L. Thackwell

The Marquardt Corporation   1
16555 Saticoy Street
Van Nuys, California 91409
Attn: Warren P. Boardman, Jr.

Martin Marietta Corporation   1
Baltimore Division
Baltimore, Maryland 21203
Attn: John Calathes (3214)

Martin Marietta Corporation   1
Denver Division
P. O. Box 179
Denver, Colorado 80201
Attn: J. D. Goodlette (A-241)

McDonnell Aircraft Corporation   1
P. O. Box 516
Municipal Airport
St. Louis, Missouri 63166
Attn: R. A. Herzmark

North American Aviation, Inc.   1
Space & Information Systems Division
12214 Lakewood Boulevard
Downey, California 90241
Attn: H. Storms

North American Aviation, Inc.   1
Rocketdyne (Library 586-306)
6633 Canoga Avenue
Canoga Park, California 91304
Attn: E. B. Monteath

Northrop Space Laboratories   1
3401 West Broadway
Hawthorne, California
Attn: Dr. William Howard

Radio Corporation of America   1
Astro-Electronics Division
Princeton, New Jersey 08540
Attn: S. Fairweather

Thiokol Chemical Corporation   1
Reaction Motors Division
Denville, New Jersey 07832
Attn: Arthur Sherman

Republic Aviation Corporation   1
Farmingdale, Long Island
New York
Attn: Dr. William O'Donnell

Space General Corporation   1
9200 East Flair Avenue
El Monte, California 91734
Attn: C. E. Roth

Stanford Research Institute   1
333 Ravenswood Avenue
Menlo Park, California 94025
Attn: Lionel Dickinson

Langley Research Center 2
Langley Station
Hampton, Virginia 23365
Attn: Dr. Floyd L. Thompson
        Director

Lewis Research Center 2
21000 Brookpark Road
Cleveland, Ohio 44135
Attn: Dr. Abe Silverstein
        Director

Marshall Space Flight Center 2
Huntsville, Alabama 35812
Attn: Hans G. Paul
        Code R-P&VED

Manned Spacecraft Center 2
Houston, Texas 77001
Attn: Dr. Robert R. Gilruth
        Director

Western Operations Office 2
150 Pico Boulevard
Santa Monica, California 90406
Attn: Robert W. Kamm
        Director

John F. Kennedy Space Center, NASA 2
Cocoa Beach, Florida 32931
Attn: Dr. Kurt H. Debus

Wright-Patterson Air Force Base 1
Aeronautical Systems Division
Air Force Systems Command
Dayton, Ohio 45433
Attn: D. L. Schmidt
        Code ASRCNC-2

Holloman Air Force Base 1
Air Force Missile Development Center
New Mexico
Attn: Maj. R. E. Bracken
        Code MDGRT

NASA Scientific and Technical Information   25
Facility
P.O. Box 33
College Park, Maryland 20740

NASA Headquarters   1
Washington, D.C. 20546
Office of Space Science and Applications
Director, Launch Vehicles and Propulsion, SV
Attn: Mr. Vincent L. Johnson

NASA Headquarters   1
Washington, D.C. 20546
Office of Manned Space Flight
Director, Advanced Manned Missions, MT
Attn: Mr. Edward L. Gray

NASA Ames Research Center   1
Mission Analysis Division
Moffett Field, California 24035
Attn: Mr. Clarence A. Syvertson

NASA Lewis Research Center   3
21000 Brookpark Road
Cleveland, Ohio 44135
Attn: Mr. Paul Herr
       Mail Stop 500-209

Ames Research Center   2
Mission Analysis Division
Moffett Field, California 94035
Attn: Mr. Harold Hornby

Goddard Space Flight Center   2
Greenbelt, Maryland 20771
Attn: Mr. Merland L. Moseson
       Code 620

Jet Propulsion Laboratory   2
California Institute of Technology
4800 Oak Grove Drive
Pasadena, California 91103
Attn: Mr. Henry Burlage, Jr.
       Propulsion Division 38

Patrick Air Force Base   1
Air Force Missile Test Center
Florida
Attn: L. J. Ullian

Air Force Systems Division   1
Air Force Unit Post Office
Los Angeles 45, California
Attn: Col. Clark
        Technical Data Center

Arnold Air Force Station   1
Arnold Engineering Development Center
Tullahoma, Tennessee
Attn: Dr. H. K. Doetsch

Department of the Navy   1
Bureau of Naval Weapons
Washington, D. C.
Attn: J. Kay
        RTMS-41

Defense Documentation Center Headquarters   1
Cameron Station, Building 5
5010 Duke Street
Alexandria, Virginia 22314
Attn: TISIA

U. S. Air Force Headquarters
Washington 25, D. C.
Attn: Col. C. K. Stambaugh
        AFRST

Picatinny Arsenal   1
Dover, New Jersey 07801
Attn: I. Forsten, Chief
        Liquid Propulsion
        Laboratory, SMUPA-DL

Air Force Rocket Propulsion Laboratory   1
Research and Technology Division
Air Force Systems Command
Edwards, California 93523
Attn: Mr. H. Main/RPRR

U. S. Atomic Energy Commission   1
Technical Information Services
Box 62
Oak Ridge, Tennessee
Attn: A. P. Huber
        Oak Ridge Gaseous
        Diffusion Plant
        (ORGDP) P.O. Box P

U. S. Army Missile Command   1
Redstone Arsenal
Alabama 35809
Attn: Dr. Walter Wharton

U. S. Naval Ordnance Test Station   1
China Lake
California 93557
Attn: Chief, Missile
        Propulsion Division
        Code 4562

Chemical Propulsion Information Agency   1
Applied Physics Laboratory
8621 Georgia Avenue
Silver Spring, Maryland 20910
Attn: T. L. Reedy

Aerojet-General Corporation   1
P.O. Box 296
Azusa, California 91703
Attn: L. F. Kohrs

Aerojet-General Corporation   1
P. 0. Box 1947
Technical Library, Bldg 2015,
Dept. 2410
Sacramento, California 95809
Attn: R. Stiff

Aeronautronic   1
Philco Corporation
Ford Road
Newport Beach, California 92663
Attn: D. A. Carrison

United Aircraft Corporation   1
Research Laboratories
400 Main Street
East Hartford, Connecticut 06108
Attn: Erle Martin

United Technology Center
587 Methilda Avenue
P.O. Box 358
Sunnyvale, California 94088
Attn: B. Abelman

Walter Kidde and Company, Inc.   1
Aerospace Operations
567 Main Street
Belleville, New Jersey 07109
Attn: R. J. Hanville
        Director of Research
        Engineering

Pratt and Whitney Aircraft   1
United Aircraft Corporation
Florida Research and Development
P.O. Box 2691
West Palm Beach, Florida 33402
Attn: R. J. Coar

Rocket Research Corporation   1
520 South Portland Street
Seattle, Washington 98108
Attn: Foy McCullough, Jr.